Theses and Dissertations   1. Thesis and Dissertation Collection, all items

2019-09

Oceanic Response Observations due to Passing Tropical Cyclones: An Assessment of Drag and Sea Spray Parameterizations

Gallagher, Stephan, D

Monterey, California. Naval Postgraduate School

http://hdl.handle.net/10945/63167

REPORT DOCUMENTATION PAGE

Form Approved
OMB No. 0704-0188

Public reporting burden for this collection of information is estimated to average 1 hour per response, including the time for reviewing instructions, searching data sources, gathering and maintaining the data needed, and completing and reviewing the collection of information. Send comments regarding this burden estimate or any other aspect of this collection of information, including suggestions for reducing this burden to Washington Headquarters Service, Directorate for Information Operations and Reports, 1215 Jefferson Davis Highway, Suite 1204, Arlington, VA 22202-4302, and to the Office of Management and Budget, Paperwork Reduction Project (0704-0188) Washington, DC 20503.
PLEASE DO NOT RETURN YOUR FORM TO THE ABOVE ADDRESS.

1. REPORT DATE *(DD-MM-YYYY)* 24-09-2019	2. REPORT TYPE Master's Thesis	3. DATES COVERED *(From - To)*

4. TITLE AND SUBTITLE

Oceanic Response Observations due to Passing Tropical Cyclones: An Assessment of Drag and Sea Spray Parameterizations

5a. CONTRACT NUMBER

5b. GRANT NUMBER

5c. PROGRAM ELEMENT NUMBER

6. AUTHOR(S)

Gallagher, Stephan, D., LCDR

5d. PROJECT NUMBER

5e. TASK NUMBER

5f. WORK UNIT NUMBER

7. PERFORMING ORGANIZATION NAME(S) AND ADDRESS(ES)

8. PERFORMING ORGANIZATION REPORT NUMBER

9. SPONSORING/MONITORING AGENCY NAME(S) AND ADDRESS(ES)

Civilian Institutions Office (Code 522)
Naval Postgraduate School
1 University Circle, Herrmann Hall Rm HE046
Monterey, CA 93943-5033

10. SPONSOR/MONITOR'S ACRONYM(S)

NPS CIVINS

11. SPONSORING/MONITORING AGENCY REPORT NUMBER

12. DISTRIBUTION AVAILABILITY STATEMENT

Approved for public release; distribution is unlimited

13. SUPPLEMENTARY NOTES

14. ABSTRACT

In 2015, Air-Launched Autonomous Micro Observer float 9077 was intercepted by Hurricane Ignacio and revealed a 40 m isotherm depression preceding the traditional, well-documented upwelling response. To replicate this unique and apparent downwelling ahead of Hurricane Ignacio and three others—Irma, Florence and Michael, the Price-Weller-Pinkel model permitted comparisons of tropical cyclone intensity indices and vertical velocity. When modeling the stress, two other traditional ideas were challenged. First, many legacy drag coefficients linearly increase with wind speed, while the modern variety maximize near tropical cyclone strength. Second it is believed sea spray droplets are sheared off large wave crests, quickly accelerate, but upon reentry, dampen smaller waves while fluxing considerable momentum to the ocean. However, many models bulk parameterize air-sea interaction processes with a legacy drag coefficient and omit spray. Therefore, this study aimed to simulate the aforementioned downwelling using seven legacy/modern drag coefficients, with and without spray stress. These analyses illustrated downwelling ahead of every storm, legacy drag coefficients as statistical outliers, invalid for TC modeling, and although its addition reduced model accuracy, sea spray remains paramount through modern drag coefficient selection. The confirmation of downwelling is supported by Ekman dynamics and may be significant in storm surge enhancement.

15. SUBJECT TERMS

upper oceanic response, tropical cyclone, hurricane, downwelling, drag coefficient, sea spray, storm surge

16. SECURITY CLASSIFICATION OF:			17. LIMITATION OF ABSTRACT	18. NUMBER OF PAGES	19a. NAME OF RESPONSIBLE PERSON
a. REPORT U	**b. ABSTRACT** U	**c. THIS PAGE** U	UU	123	**19b. TELEPONE NUMBER** *(Include area code)*

Standard Form 298 (Rev. 8-98)
Prescribed by ANSI-Std Z39-18

THIS PAGE INTENTIONALLY LEFT BLANK

Oceanic Response Observations due to Passing Tropical Cyclones: An Assessment of Drag and Sea Spray Parameterizations

By

Lieutenant Commander Stephan D. Gallagher, United States Navy

B.S., The Pennsylvania State University, 2009

Submitted in partial fulfillment of the requirements for the degree of

Master of Science in Physical Oceanography

at the

MASSACHUSETTS INSTITUTE OF TECHNOLOGY
and the
WOODS HOLE OCEANOGRAPHIC INSTITUTION

September 2019

Signature of Author

_____
Joint Program in Physical Oceanography
Massachusetts Institute of Technology
and Woods Hole Oceanographic Institution
August 9, 2019

Certified by

_____
Steven R. Jayne
Thesis Supervisor
Woods Hole Oceanographic Institution

Accepted by

_____
Glenn R. Flierl
Chair, Joint Committee for Physical Oceanography
Massachusetts Institute of Technology

Oceanic Response Observations due to Passing Tropical Cyclones: An Assessment of Drag and Sea Spray Parameterizations

by

Lieutenant Commander Stephan D. Gallagher, United States Navy

Submitted to the Joint Program in Physical Oceanography
Massachusetts Institute of Technology
& Woods Hole Oceanographic Institution
on August 9, 2019, in partial fulfillment of the
requirements for the degree of
Master of Science in Physical Oceanography

Abstract

Most traditional theories regarding upper oceanic response due to passing tropical cyclones involve an initial and predominant upwelling based on storms' strong cyclonic flow and resulting positive wind stress curl imparted on the sea surface. In August 2015, Air-Launched Autonomous Micro Observer float 9077 was intercepted by Hurricane Ignacio and its temperature measurements revealed a 40 m depression of the 26°C isotherm ahead of the device's closest point of approach with the storm and usual upwelling response. This unique finding motivated attempting to replicate the apparent downwelling ahead of Hurricane Ignacio and three others—Irma, Florence and Michael, using the Price-Weller-Pinkel ½ order closure model, via comparisons of the depth of the 26°C isotherm, tropical cyclone heat potential and vertical velocity. When modeling the total stress, two other traditional ideas were challenged. First, many legacy drag coefficients linearly increase with wind speed, while the modern variety maximize near tropical cyclone strength, with varying asymptotic and/or decreasing end behavior. Second, it is believed that sea spray droplets are sheared off the largest wave crests, quickly accelerate in the high winds, but upon reentry, dampen the smaller waves and flux substantial amounts of momentum to the sea. Taken together, many traditional atmosphere-ocean models bulk parameterize air-sea interaction processes and employ a legacy drag coefficient and omit or crudely formulate sea spray. Therefore, this study aimed to simulate the aforementioned downwelling using 14 total forcing parameterizations, including seven different legacy or modern drag coefficients, with and without spray stress. A combination of qualitative and statistical analyses illustrated downwelling was present in Hurricane Ignacio and every other storm by a large majority of variable indices, legacy drag coefficients were statistically significantly over-estimating outliers and should not be employed in tropical cyclone models, and while the explicit addition of sea spray to interfacial stress reduced model accuracy, this phenomenon remains paramount through modern drag coefficient selection. The confirmation of downwelling is physically founded in Ekman dynamics and may be significant in storm surge enhancement due to the accompanying surface height anomaly and near-shore depth limitations forcing water, with a negative vertical velocity, ashore.

Thesis Supervisor: Steven R. Jayne
Title: Senior Scientist, Woods Hole Oceanographic Institution

3

THIS PAGE INTENTIONALLY LEFT BLANK

Acknowledgements

With so many wonderful and influential people to thank, maybe approaching this chronologically, with only first names to maintain anonymity, would be best. Well, without my Mom and Dad, not only would I not be here, but I wouldn't be the hardworking, dedicated student and Naval officer I am today. This ride, both through the Navy and here at MIT/WHOI hasn't always been easy, but the reward and positive influence on my life is unmatched and I would absolutely do it again. Thank you for all of the support, guidance, love, and phone calls—those 75 minute drives back from WHOI needed audible entertainment.

My passion for weather has been innate as long as I can remember, but not necessarily for research, which was bolstered at an undergraduate at Penn State. I would to thank Anne for the opportunity to join the GATOR Team and experience a taste of the scientific community, data processing, and conferences. Without that research experience, I may not be here and I wouldn't have met life-long friend Alaina, who despite being a Steelers fan, provided me the basic guidance and underlying motivation to earn a Master of Science, something I did not foresee 11 years ago.

While I was certainly interested in applying to the MIT/WHOI JP, it was my wife Dominique that really pushed me to actually go for it. Despite her hate of cold weather, she signed up for two years of it for the betterment of my career. Rest assured, without her, I again wouldn't be here. Additionally, she volunteered to sacrifice 11 months away in the east Pacific just to allow me to focus on writing this thesis—unmatched dedication.

Upon arriving at WHOI, my research advisor Steve recruited me to join his team and fly with the Hurricane Hunters. I cannot thank him enough for this once in a lifetime experience and research opportunity. In addition, he was a great advisor during my time here in the JP. I never felt pressured with due dates, deadlines, deliverables, etc.; he was always there for me when I had questions, required guidance, or needed help with computer programing—my Achilles heel as a graduate student. Even while deployed with the United States Coast Guard, he routinely provided me feedback on this thesis and took time out of his demanding schedule to get me to the finish line. Thanks again for everything Steve!

Through working with Steve, I was privileged enough to fly with the United States Air Force 53rd Weather Reserve Squadron—the aforementioned Hurricane Hunters, traveling to St. Croix, Hawaii and Savannah and flying missions in Hurricanes Hector and Florence. That group of reserve officers and airmen were always jovial, easy-going and accommodating to my Navy and Coast Guard brethren, but simultaneously, consummate professionals and experts willing to be away from their families for weeks on end to improve forecasting efforts and ultimately ensure the safety of other American citizens and allies. Without their willingness to conduct joint operations with us oceanographers, this study would have had never happened.

While the Hurricane Hunters were instrumental, the connection to their team would absolutely not exist without the unwavering efforts of both Steve and Beth. In addition to the professional development and guidance as a fellow METOC officer, she was absolutely essential to allowing us to seamlessly jump on weather reconnaissance flights to obtain our ocean data. In addition, her dedication to incorporating ocean measurements to coupled atmosphere-ocean models is illustrated through her work with the TROPIC program, allowing midshipmen to get the same Hurricane Hunter experience and garner a taste of operational ocean science. Needless to say, without Beth's selfless efforts and immense leadership, I would have never had the opportunity to fly through hurricanes and the devices measuring the data used in this study may have never been deployed.

Through my work with Steve, Beth, and the TROPIC team, I met a several fantastic prospective Naval officers and really enjoyed the volleyball, beach time, and just hanging out with Rachel, Kelli, Grace, Shannon and Jordan! With that said, I also had a chance to become friends with, learn from, and even mentor one of the smartest people I have ever met—Casey, and I don't know where I would be without his unswerving support! I cannot thank him enough for his work on the Price-Weller-Pinkel model modernization and conversion to MATLAB, not to mention all of the specific assistance he provided me along the way. If it weren't for Casey, I don't think my study would have been nearly as model-centric, thus much less robust. I can't thank him enough!

While at MIT taking classes, I met Jing and Astrid, who are now colleagues and friends for life. The problem sets in MIT classes are challenging to say the least and they demand teamwork; for someone who hadn't attended a college course in over eight years, I needed an understanding, sharp teammate willing to help and Jing was it. In addition to support with classes, she was a great office mate willing to listen to me try to translate Navy-speak and my stories. Astrid was also an amazing office mate, one of the nicest people I have ever met, and always there to provide guidance as a senior student. I absolutely loved the time I had in the Green Building with Jing and Astrid, where we also shared another passion—chocolate!

With my wife deployed, there were two beings here in Boston that buoyed my emotions and helped me get through this initially daunting task. My brother Drew moved here and we have shared many fun experiences including Red Sox games, golfing, concerts, volleyball, basketball, watching sports and even some coding help. Without any great nearby friends, Drew was that for me and I can't thank him enough for deciding to start his professional career here with me, in a new city. Despite all of the aforementioned people I have graciously thanked, there was another being there for me day in and day out, listened to me yelling at MATLAB and Word, dealt with the extreme cold and heat in our wonderful abode, and shared meals throughout the last year. Izzy, our dog, was always there for an emotional lift and I will give her a bone after this paragraph.

Lastly, I would like to thank the MIT/WHOI JP professors and administrators for their unswerving devotion to the students. For me, without Kris, Lea, Kathy, Julia, and Claudia, I would have been at a loss.

Contents

THIS PAGE INTENTIONALLY LEFT BLANK

List of Figures

THIS PAGE INTENTIONALLY LEFT BLANK

List of Tables

THIS PAGE INTENTIONALLY LEFT BLANK

Chapter 1

Introduction

1.1   Motivation

Tropical cyclones (TCs) have affected people all over the globe for centuries, and within the last 14 years, there has been a series of particularly memorable storms (e.g. Hurricanes (HU) Katrina, Sandy, Harvey, and Irma and Typhoon Haiyan) due to the vast devastation they caused. While every storm's impacts are different, based on both the system itself and characteristics of its landfall, historically damage to life and civilization has been proportional to intensity [1]. Unfortunately, significant improvements in intensity forecasts have been slow with respect to track predictions in the 21st Century [2]. One of the most memorable examples of a poor intensity forecast involved HU Katrina in 2005. After briefly making landfall over southern Florida, the modest category one storm was forecast to intensify to no greater than category two, over the ensuing five days, according to 76% of models [3]. However, now infamously, HU Katrina was fixed as a category five storm within 54 hours, where just one model had predicted such an intensification over the Gulf of Mexico. While much of the devastation this storm would go on to cause in Alabama, Mississippi and Louisiana was inevitable, earlier, more accurate intensity forecasts could have assisted government and emergency management decision makers as well as citizens alike in evacuation procedures, ultimately saving more lives. To improve these modelling efforts, it is paramount to properly characterize the relationship between the ocean and the atmosphere with respect to TCs. The ocean is the primary energy source for their sustainment and strengthening, with warmer upper ocean temperatures correlating to intensification [4]. Historically, this effect was parameterized by wide-spread measurements of sea surface temperature (SST) (via satellites) with 26°C acting as the benchmark for development, but more recent studies have suggested the volume of this warm water provides a stronger representation of the ocean's available energy (in the form of latent and sensible heat).

17

To that end, other heat-bearing metrics, such as integrals down to the 26°C isotherm, may be critical to better characterizing intensity [5], [6], [7]. Using these variables, coupled atmosphere-ocean models have outperformed the uncoupled variety [8] and have been extremely valuable in areas where only marginal TC potential exists, based on all such data [9].

While there are many viable and accurate ways to measure the upper layers of the ocean, the two methods used herein have a distinct advantage over most—they can be strategically positioned in a storm's track with little safety risk and impact to normal operations. First, Air-Launched Autonomous Micro Observer (ALAMO) floats are deployed during TC reconnaissance flights by United States Air Force (USAF) 53rd Weather Reconnaissance Squadron (WRS) WC-130J aircraft [4], strategically placed to optimize the measurement of storm dynamics. Second, the United States' Navy Littoral Battlespace Sensing unmanned underwater vehicles, more commonly referred to as gliders, are pre-deployed vessels, piloted by the Naval Oceanographic Office (NAVO), to measure ocean variables all throughout the world [10]. Despite their distinct deployment methods and levels of autonomy, each device is able to relay real-time profiles of oceanic variables beneath TCs, directly supporting coupled atmosphere-ocean model initialization and post-storm analysis[1].

The very specific nature of this project was motivated by an observation from ALAMO 9077 during its interaction with HU Ignacio, an eastern Pacific storm from late August 2015. Originally deployed on August 3 [11], this float was strategically positioned in the forecast path of HU Guillermo, but due to an unfortunate shift in track to the northwest, its interaction with the storm was muted with an estimated 140 km closest point of approach (CPA) [12]. Despite this lost opportunity and the near-miss of another major hurricane to the south just a week later, the return on investment for ALAMO 9077 was advantageously founded 27 days after its initial deployment. Due to the ALAMO's sample duration (on the order of months) [13], this float drifted north and successfully captured a valuable set of data during the passage of HU Ignacio, where its CPA with the storm was less than 5 km, as depicted in Figure 1-1. In particular, an initial analysis of the time series of measured temperature (vs. depth) profiles indicated a sharp isotherm deepening throughout the water column, nearly aligning with the storm's CPA. To best illustrate this observation, the perturbation of the depth of the 26°C isotherm was plotted in

---

[1] ALAMO floats and the Navy glider used in this analysis will be presented in detail in Section 4.1.1 below.

Figure 1-2, initialized using measures 12 hours prior to the storm's CPA with ALAMO 9077. The steep decline in the depth of the 26°C isotherm maximizes just after the storm's CPA with the float, followed by a symmetrical recovery, and then a nearly sinusoidal pattern for the remaining hours with all values indicating a shallowing depth. While the latter follows the
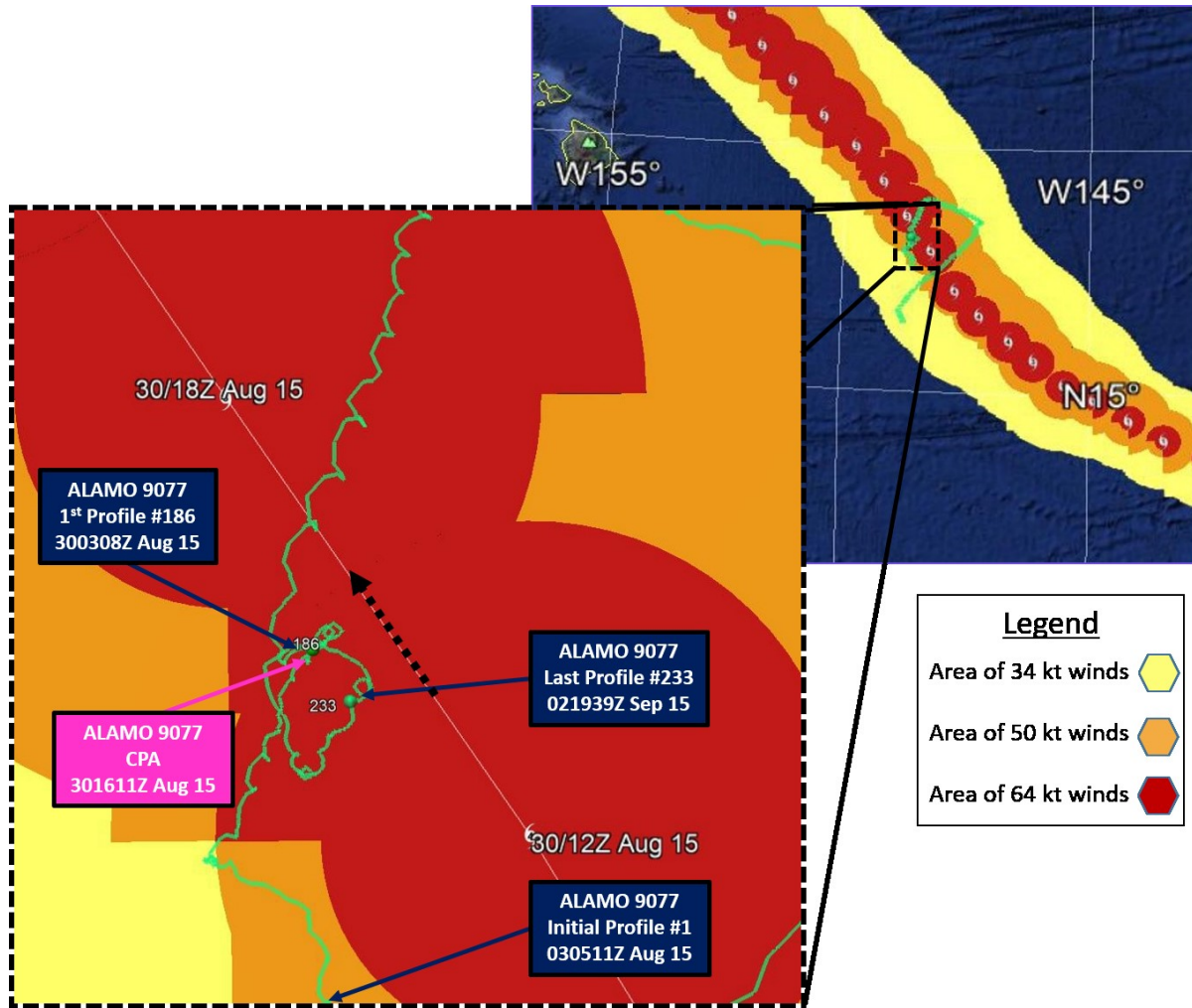
Figure 1-1: Interaction between HU Ignacio and ALAMO 9077 [12], [11]. The left image displays the majority of the storm's track with the modeled area of over water wind speeds in 34, 50 and 64+ knot thresholds as well as the entire path of ALAMO 9077, from its initial deployment to final profile. The right image zooms in on this interaction and labels the time and position of the initial deployment, first and last profiles used in this analysis, and the CPA between the storm and float.

traditional theories on the upper oceanic response to TC passage (to be discussed in 1.2 below), the former does not, motivating the remainder of this study to attempt to replicate, model, parameterize and assess implications of this event in other storms.

1.2   Traditional Ideas

The following traditional ideas or theories will be investigated and/or challenged, based on observed measurements and/or model output, within this study: upper oceanic response to the passage of a TC, relative importance of sea spray in models and other investigations and drag coefficients at high wind speeds.

1.2.1   Upwelling During Tropical Cyclone Passage

Up until the 1970s, only a few studies had been conducted involving the oceanic response to a TC. In particular, these investigations had identified upwelling and entrainment of cool, sub-

HU Ignacio
Depth of 26°C Isotherm Perturbation Under Varying Stress
Grid Position (x,y) [km]
0
-5
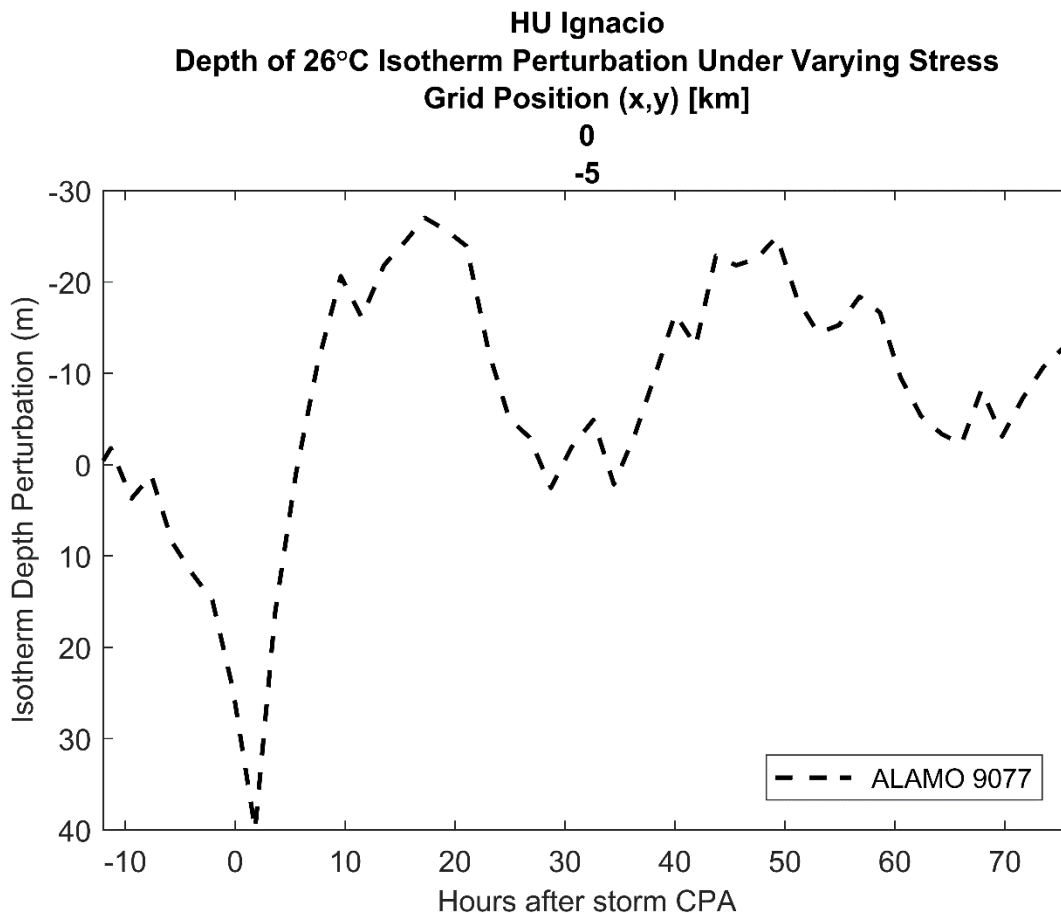
Figure 1-2: Depth of 26°C isotherm perturbation, during the passage of HU Ignacio, as measured by ALAMO 9077 and initialized 12 hours prior to its CPA with the storm. Positive perturbation values reflect a depression in the original measured depth of the 26°C isotherm.

thermocline waters in response to surface hurricane forcing, but only accounting for the barotropic response of stationary storms [14]. Based on these findings and the great implications

20

of a cooling mixed layer on the intensity of the forcing TC and any subsequent storms, Geisler [14] aimed to advance these findings, but by considering the much more realistic baroclinic response of a translating storm. Using an inviscid two-layer deep ocean model on a plane of constant Coriolis (e.g. f-plane), Geisler forced the storm with a radially-symmetric, negative atmospheric pressure anomaly, with cyclonic wind stress curl, and translated it at a constant rate along the negative x-axis [14]. While there were several landmark findings in this investigation related to the cold wake and its amplitude as a function of the translation speed and storm strength, the most relevant result to this study was the sign of the induced vertical velocity nearest to the position of the storm. For a translation speed of 7 m/s, the resulting upper oceanic response was a maximum of positive vertical velocity in the immediate wake of the storm, followed by inertial oscillations with alternating minima (negative) and maxima (positive) of vertical velocity, dissipating with increasing along-track distance [14]. For a translation speed of only 3.5 m/s, the result was much different, but maintained a maximum of vertical velocity centered at the storm's position, with positive values both ahead and in its wake [14]. In each result, the maximum in vertical velocity nearest the storm indicated upwelling as the initial, prevailing upper oceanic response to a translating TC, without mention or modeling of preceding downwelling. These findings have set the precedent for the theory on the upper oceanic response to a translating TC for the past half-century, but are in direct contrast to the aforementioned observations by ALAMO 9077 of HU Ignacio. Attempting to resolve this discrepancy will be a chief component of this study.

1.2.2 Relative Importance of Sea Spray

As identified by Andreas [15], most synoptic and mesoscale models utilize a bulk surface flux parameterization of turbulent exchanges across the air-sea interface. In doing so, these only use bulk meteorological quantities (e.g. wind speed, temperature, humidity) and fail to consider the implications of smaller scale, surface-based processes such as sea spray [15]. This phenomenon has the potential to have a significant effect on momentum, sensible and latent heat fluxes between the ocean and atmosphere, especially in a TC, where wind stress is extreme and the temperature gradient across the boundary has great implications for storm intensity[2]. To that

---

[2] Sea spray theory will be presented in detail in Chapter 3 below.

end, the aforementioned challenges with TC intensity forecasts may be attributed to such inadequacies in the modeling of air-sea interaction, including processes such as sea spray [16], [17]. In addition to atmospheric models, many ocean models, including the Price-Weller-Pinkel (PWP) model[3] used herein, also omit smaller scale phenomena, including sea spray, from its surface forcing. In a TC, this added forcing and potentially substantial source of surface momentum might have the ability to drive the observed downwelling ahead of upwelling and inertial oscillations. To that end, this study will incorporate sea spray into the PWP model by adjusting the wind stress forcing of a translating TC and analyze the upper oceanic response.

1.2.3 Drag Coefficients at High Wind Speeds

Based on the aforementioned methodology of incorporating sea spray through wind stress forcing, its parameterization is fundamental to this study. As such, a brief review of this parameter is appropriate. Wind stress, τ, upon the sea surface, is defined by equation (1),

$$\tau = \rho C_D U_{10}^2, \tag{1}$$

where ρ is the density of air, C_D is the drag coefficient, and U_{10} is the mean wind speed 10 m above the ocean surface [18], [19]. While the first and last parameters are easily computed and standard measured values respectively, the drag coefficient is anything but and has evolved through its history over the last half century. Based on theories, lab experiments, and/or observations, these values have taken on various forms to include constant, constant piecewise values as a function of U_{10}, piecewise functions of U_{10} to a limiting value and becoming constant, linear functions of U_{10}, and several others with a multitude of variable inputs. Inevitably, however, under TC force winds, the greatest challenge in each of these parameterizations is the inherent difficulty in accurately obtaining surface flux measurements, thus many of these findings remain estimates or are simply unreliable above a relatively low wind speed threshold. Further complicating the matter, there are many theories on what the sea surface resembles under such great forcing, from a monotonically increasing wave field to an emulsion layer of suspended water droplets and entrained air, and everything in between. With that being said, one of the first declarations of the appropriate characterization of C_D for TC wind

---

[3] The PWP model and details of the surface forcing will be presented in Chapter 4 below.

forcing was made by Wu [20], which was a linearly increasing function of U_{10} [20], [18]. This parameterization also closely resembled that of Garratt[4] [21], which was used in the original version of the PWP model [22], while Wu's was also featured in prominent ocean models (e.g. Simulating Waves Nearshore (SWAN)) [18]. While unknowns remain with regards to the drag coefficient under TC force winds, there is a resounding belief that the C_D does not monotonically increase with U_{10} for a variety of theoretical explanations. As such, this study will apply a series of C_D parameterizations to the wind stress component of the PWP model, to demonstrate their distinction and test their validity under TC forcing, as compared to the measured response of the upper oceanic layer.

1.3   Contribution

This thesis builds upon the illuminating and valuable results that can be obtained by measuring oceanic variables, from beneath a passing TC, using air-deployed and autonomous devices [4], [5]. In particular, it contributes to the following:

(1) Resolving, modeling and explaining the downwelling observed by ALAMO 9077, during the passage of HU Ignacio, using the PWP model with varying wind stress forcing and measurements from sensors at distinct CPAs to four passing storms. By replicating the presence of downwelling as a consistent response from all storms, this study will also provide intuition on another physical mechanism driving storm surges.

(2) Enhancing insight on the drag coefficient at TC force winds by comparing the modeled output of various parameterizations against measured data through their effects on the upper oceanic layer.

(3) Determining the relative magnitude of the effect of sea spray on the upper ocean layer, in terms of momentum transfer, for potential incorporation in future TC models.

   The remainder of this thesis is organized as follows: Chapter 2 discusses the drag coefficient and each of the specific parameterizations used herein; Chapter 3 describes sea spray theory in terms of momentum transfer and parameterization; Chapter 4 provides details on measurement platforms, PWP model, and measured versus modeled results; Chapter 5 considers the oceanic vertical velocity response results to passing storms and associated their implications as well as

---

[4] The drag coefficient parameterizations of Garratt, Wu and five others will be detailed in Chapter 2 below.

compares findings herein to similar publications; and Chapter 6 is a summary of the findings and lists future directions and applications for this research.

Chapter 2

Drag Coefficients

2.1 Evolution of Drag Coefficients

The parameterization of the drag coefficient dates back to the late 1950s when a series of winter storms in the north Atlantic Ocean generated threatening significant wave heights to underway vessels and fears of enhanced near-shore tidal forcing, during a hurricane, sparked the need for a reliable measure of C_D [18]. Since then and as mentioned in the introduction, C_D has taken on many forms and when considering TC force winds, the majority of parameterizations simply do not apply. Most of these formulations incorporated a linear function of U_{10}, where C_D increased up until a wind speed threshold between 21 - 26 m/s. While there was some variability for smaller values of U_{10}, the only one of the group to make a claim in parameterizing higher wind speed measures was Wu [18]. This relationship was generally accepted until a series of studies in the early 2000s first illuminated the possibility of a saturated drag coefficient, one that would slow its rate of increase, maximize, and/or asymptote at higher wind speeds [18]. This idea sparked a second series of investigations and experiments in search of a more complete C_D, which have varied greatly in both methodology and result. These studies used laboratory experiments, measured values at towers and in storms, remote sensing as well as reanalysis data to parameterize C_D. In this study, five of the modern C_D parameterizations involving varying approaches and/or results were selected, along with the legacy formulation of Wu and Garratt and a constant value of C_D, to force the PWP model and compare the upper oceanic response with measured data.

2.2 Drag Coefficient Selection and Description

The following subsections will chronologically detail the methodology, theory and specific parameterization of each drag coefficient as well as the motivation for its inclusion in this study.

2.2.1 Constant

Serving as a baseline, a constant C_D was selected in order to illustrate the upper oceanic response to TC forcing without allowing it to vary with wind speed, falling in the middle of many of the theories describing the sea surface under such conditions. In addition, this parameterization represents a historical view of the drag coefficient, as many of which were constant. As such, the constant drag coefficient is given by

$$C_{D\_Const\ C_D} = 1.3\ x\ 10^{-3}. \tag{2.1}$$

2.2.2 Garratt (1977) and Wu (1982)

The drag coefficient parameterizations by Garratt and Wu serve as the legacy characterizations in this study as each results in a linear increase of $C_D(U_{10})$. Beginning with the former, Garratt aimed to derive a drag coefficient through three primary relationships including wind stress (equation (1)), the neutral drag coefficient (C_{DN})[5] and Charnock's relation [21]. Beginning with C_{DN}, which is derived from Monin-Obukhov similarity theory and accounts for the drag coefficient in neutrally stable conditions, is given by

$$C_{DN} = \frac{k^2}{\left(ln\left(\frac{z}{z_0}\right)\right)^2}, \tag{2.2a}$$

where k is von Kármán's constant and z_0 is the aerodynamic roughness length. Next, Charnock's relation implies, for an aerodynamically rough flow, over the ocean, z_0 is only a function of the surface friction velocity (u_*) and gravity (g) [23], as given by

$$\frac{z_0 g}{u_*^2} = \alpha = constant, \tag{2.2b}$$

---

[5] C_{DN} and C_D will be presented herein as they were established in their respective publications. While C_{DN} assumes a neutral atmosphere and C_D does not imply such a condition, they will be used and applied interchangeably within this study as the PWP model does not contain a vertical atmosphere, as will be discussed in Section 4.1.2. As a result, while there remains a physical difference between the parameters, it will not be paramount herein.

where

$$u_* = U_{10}\sqrt{C_D} \text{ and } u_* \approx U_{10N}\sqrt{C_{DN}}. \qquad (2.2c, 2.2d)$$

In addition to these relationships, Garratt incorporated more than 20 recent drag coefficient parameterizations utilizing either large or local scale stress calculations. The former set of results used measurements of surface water tilt under wind forcing or geostrophic departure to empirically derive the wind stress [21], thus C_{DN} via equation (1). Meanwhile, the latter involved two distinct processes to determine C_{DN} with the local measurements. First, some studies assimilated wind profiles [21] and used the wind flux profile method to determine z_0 in the boundary layer, then used formulations similar to equation (2.2a) to find C_{DN}. Second, the remaining publications measured eddy covariance $(\overline{u'w'})$ from a rigid platform [21] and were able to find C_{DN} using equation (1) along with a second parameterization of wind stress, as given by

$$\vec{\tau} = \overline{u'w'}. \qquad (2.2e)$$

Using all of the aforementioned studies, Garratt plotted each characterization of C_{DN} vs. U_{10} and conducted a fit to derive u_* and a representative neutral drag coefficient for all of these data from equation (2.2a). As such, Garratt found the following parameterization:

$$C_{DN\_Gar} = (0.75 + 0.067U_{10}) \; x \; 10^{-3}, \qquad (2.2f)$$

valid for $4 < U_{10} < 21$ m/s [21]. As alluded to in Chapter 1, this parameterization was selected for this study because it was incorporated in the initial version of the PWP model. While that reason alone would make its inclusion worthwhile, the following is even more substantial—its validity under TC wind forcing is questionable as such stress is well outside of the domain of Garratt's function. With that being said, this perception takes on a different meaning based on the findings of Wu [20].

Wu utilized a nearly identical method as Garratt in terms of equations and including parameterizations over many studies, specifically those using the wind profile and eddy covariance methods, the two most accurate of those included in Garratt's study, in order to limit error [18]. After averaging the accumulated data set and performing the associated regressions

and calculations as Garratt above, Wu found the following representation of for the drag coefficient:

$$C_{D\_Wu} = (0.8 + 0.065U_{10}) \; x \; 10^{-3}, \tag{2.2g}$$

but valid for $U_{10} > 1$ m/s [20]. Contrary to Garratt, while each used largely the same data, Wu claimed his parameterization could be applied through TC force winds despite very few data points at such speeds [20]. This proclamation is significant to this study as it may help explain why C_{DN_Gar} was used in the original PWP model in hurricane simulations. First, as might be expected, C_{DN_Gar} and C_{D_Wu} are nearly identical and second, with Wu's claim, using either drag coefficient in the model would be reasonable in the early 1980s. To that end, this study will also use C_{DN_Gar} as the legacy parameterization of the drag coefficient under TC forcing.

2.2.3 Powell et al. (2003)

Beginning with Powell, the following series of drag coefficient formulations will represent modern characterizations where C_D saturates under TC forcing. Unlike the other four modern drag coefficient parameterizations used herein, Powell was the only one to use direct measurements of TC force winds. He and his team utilized over 300 global positioning system (GPS) dropsondes, deployed by USAF reconnaissance or National Oceanic and Atmospheric Administration (NOAA) weather research aircraft, within 15 category 1-4 hurricanes during the late 1990s [24]. The dropsondes, which were deployed from flight altitudes of at least 1.5 km, measured wind speed (along with several other meteorological variables) every 0.5 s, calibrated to an accuracy of 0.5-2.0 m/s. After binning the measures into 5 categories (30-39, 40-49, 50-59, 60-69 and 70-85 m/s) as determined by the profile's mean boundary layer (MBL) wind speed (below 500 m), they were then filtered, normalized by the respective MBL speed, and then plotted on a logarithmic scale [24]. This technique, known as the wind flux profile method, aims to extrapolate z_0 by combining equations (2.2a, 2.2d), rearranging them into the following form,

$$\ln(z) = \frac{k}{u_*}U + \ln(z_0), \tag{2.2h}$$

and conducting a least squares fit (from $z = 100\text{-}150$ m) to each bin of data providing the slope $\left(\frac{k}{u_*}\right)$ and y-intercept $(\ln(z_0))$ [18]. Subsequently, z_0 can be reapplied to equation (2.2.a) to find

the neutral drag coefficient, which output four important values of C_{DN} as function of wind speed (with the 70-85 m/s bin lacking requisite sampling for a statistically significant result). While no explicit form for C_{DN} was published, the following significant findings were displayed and expounded upon. While the magnitude of C_{DN} for $U_{10} < 40$ m/s was similar to that of the legacy drag coefficient parameterizations, for values $U_{10} > 33$ m/s and most drastically between 40-51 m/s, C_{DN} decreased [24]. With this breakthrough finding, Powell postulated the development of sea foam and spray covering the surface might significantly alter air-sea momentum exchange at wind speeds greater than 40 m/s[6] [24], thus saturating or even lessening C_{DN}. As a result, this parameterization was selected for use in this study due this substantial finding and its clear relation to sea spray stress as well as its incorporation of direct measures of wind speed at TC force.

2.2.4   Donelan et al. (2004)

One year later, Donelan and his team aimed to investigate the drag coefficient at high winds in order to confirm the following theories. First, in open ocean, wind stress under moderate forcing is maintained by form drag of the roughness elements—waves, which have a slower phase speed than the wind. As such, as wind speed increases, the band of distinct, yet slower wave phase speeds grows, thus resulting in an increase in C_{DN} [25]. While this had been validated by many of his predecessors, most of the data utilized only encompassed wind speeds up to 25 m/s, thus raising questions on extrapolation to gale and storm force winds. Second, Emanuel argued that if C_{DN} was to monotonically increase with wind speed, TC's with strength greater than 50 m/s would not be sustainable as surface friction would reduce storms' kinetic energy faster than it could be garnered from oceanic heat fluxes (i.e. enthalpy fluxes and transfer coefficient (C_K) cannot be less than momentum fluxes and the drag coefficient) [17]. With data and studies supporting each idea, Donelan developed a study to investigate the delta by utilizing momentum budgets within an air-sea interaction tank. In doing so, he measured the surface stress under variable wind forcing with specialized and precise devices (e.g. laser/line scan cameras), calculated the horizontal pressure gradient by via the surface slope and applied momentum budgets to finally determine the drag coefficient using equation (1) [18]. After extrapolating the

---

[6] Sea spray theory will be presented in detail in Chapter 3 below.

data logarithmically from the tank height of 30 cm to the usual 10 m, despite no explicit publication, the resulting drag coefficients indicated the expected increase between wind speeds of 3-33 m/s, but then reached saturation under greater forcing, asymptoting to 2.5 x 10^{-3} [25]. Physically, Donelan attributed this limit to a change in the flow characteristics as under such wind forcing, waves break incessantly, preventing the flow of air from following, and efficiently exchanging momentum with, the crests and troughs [25], [16]. While this result largely matched the legacy parameterizations and findings of Powell for less than TC force winds, the saturation of C_{DN} was unique and provided a new theory for surface roughness when sea spray and foam become significant, which is why it was selected for this study.

2.2.5 Zijlema et al. (2012)

Unlike the previous studies explicitly aimed at addressing the drag coefficient, Zijlema and his team were initially investigating bottom friction within wave models, specifically looking to resolve a potential discrepancy in bottom friction coefficients between local wind waves and swells in shallow water. Motivated by hindcasts from the SWAN and other models over-estimating the dissipation of waves, in their initial analysis, they discovered the greater of the two bottom friction coefficients might be at fault and that it was derived in storm conditions [26]. As a result, they hypothesized the drag coefficient under the strong forcing may have been too high, pointing them to a possible source of the issue—the SWAN model's drag coefficient was that of Wu, as given by equation (2.2g), for wind speeds of 7.5 m/s or greater [26]. As detailed in Section 2.2.2, this parameterization increases linearly with wind speed and since it was deemed valid for TC force winds 30 years earlier, it takes on a large C_D in any storm. In order to accurately parameterize the bottom friction coefficient, Zijlema first had to resolve the possible drag coefficient over-estimation, especially given more recent studies claiming saturation. Ironically, he and his team used a similar method as Wu by incorporating data from other drag coefficients and then bin averaging and fitting C_D as a function of wind speed. There were a total of nine published studies assimilated, four of which dated back to the 1970s-1980s to include Garratt and Wu, with the remaining five including and following the work of Powell in 2003. Using a second order fit, Zijlema established the following parameterization where

$$C_{D\_Zij} = (0.55 + 0.0943U_{10} - 0.0015U_{10}^2) \; x \; 10^{-3}, \tag{2.2i}$$

which aligns with the findings of other studies for wind speeds to about 30 m/s, where it takes its distinct shape by sharply decreasing [26]. This parabolic form of C_D takes on extremely low values at very high wind speeds, and if left unbounded, its upper limit would result in a zero or even negative parameterization. In order to avoid to this seemingly physical impossibility where extreme winds would result in the ocean surface applying stress to the atmosphere, an upper bound has been applied as follows

$$C_{D\_Zij\_bounded} = \begin{cases} (0.55 + 0.0943U_{10} - 0.0015U_{10}^2)x\ 10^{-3}, 0 \leq U_{10} < 64.4\frac{m}{s} \\ 0.4x10^{-3}, \qquad\qquad\qquad\qquad U_{10} > 64.4\frac{m}{s} \end{cases}, \quad (2.2j)$$

matching the same technique as Hwang [27].

This parameterization was initially chosen based on its distinct saturation and sharp decrease of C_D under TC force winds as well as its simplicity as a modern form. Upon further research of other publications, it became clear that Zijlema's findings were at the extreme end of the modern, saturated C_D results and in direct contrast to Wu, thus Garratt, making its inclusion valuable for comparison under TC forcing.

2.2.6 Edson et al. (2013)

While this investigation incorporated some of the foundations and relations used in legacy studies such as Garratt, Edson and his team conducted far and away the most in-depth, all-encompassing and observationally driven study of those used herein. In doing so, Edson based his approach on parameterizing the drag coefficient by dividing the boundary layer into two distinct regions—the Monin-Obukhov (MO) and wave boundary layers (WBL). As the title suggests, the MO layer is governed by MO similarity theory, which states the generation of turbulence is a function of the height above the surface (z) and MO length (L) [28]. These two metrics together parameterize the shear and buoyancy driven generation of turbulence, where negative values of $\frac{z}{L}$ indicate unstable flow and enhanced mixing, positive values of $\frac{z}{L}$ indicate stable flow and suppressed mixing and a zero value of $\frac{z}{L}$ accounts for neutral conditions. This theory has been used and validated effectively many times, both on land down to the surface and over water, but only above the WBL. While Edson's overall aim was to improve the parameterization for the surface roughness and drag coefficient in general, he and his team also

31

had a specific focus on the WBL, hoping to advance the function of C_{DN} beyond just that of wind speed, potentially to include wave parameters such as wave age and/or sea state [28].

Three Eulerian data sets were used in their study, two of which were effectively towers in the ocean and the other a set of moored buoys, which included precise measures of wind, temperature and humidity, allowing for momentum and buoyancy fluxes to be found via direct eddy covariance [28]. Using these data, under neutral conditions, their baseline formulation for the drag coefficient is an extension of equation (2.2a) as used by Garratt, as given by

$$C_{DN} = \frac{k^2}{\left(ln\left(\frac{z}{z_0}\right)\right)^2} = -\frac{\overline{u'w'}}{U_N^2 G}, \tag{2.2k}$$

where U_N is the vector-averaged wind velocity (relative to water) under neutral stratification and G is the gustiness parameter, which is the ratio of the wind speed to the vector-averaged wind. All of the variables in equation (2.2k) can be directly measured except for the aerodynamic roughness length, z_0, which can be further parameterized as a function of wind speed (friction velocity), wave age (inverse wave phase speed) and significant wave height. Edson tested each of these measures and associated parameterizations by varying the Charnock "constant," as given in equation (2.2b), but allowing α to vary; rather than expressing each relationship here, he would go on to find that his wind speed dependent formulation of z_0,

$$z_0 = \frac{\gamma v}{u_*} + \alpha \frac{u_*^2}{g}, \alpha = mU_{10N} + b, \tag{2.2l}$$

where γ is the roughness Reynolds number for smooth flow and v is the kinematic viscosity while $m = 0.017$ m/s and $b = -0.005$ as determined through a fit of the bin averaged wind data from 7-18 m/s, outperformed the inclusion of wave information. This was determined through comparisons with the direct eddy covariance measurements and a global wind-derived C_{DN} given wave age-dependent surface roughness via European Centre for Medium-Range Weather Forecasts (ECMWF) models [28].

This study, despite its encompassing and detailed measurements and findings matching that of previous investigations and models, only included a handful of data points in which winds were above 20 m/s. Recognizing this "limitation," Edson conducted a fit of the friction velocity using his data for wind speeds greater than 8.5 m/s, where he determined for

$$u_* = C_m U_{10N} + u_{*0}, \qquad\qquad (2.2\text{m})$$

C_m = 0.062 and u_{*0} = -0.28 were in great agreement with recent studies [28]. Based on this result and rearranging with equation (2.2d),

$$C_{D10N} = \left(C_m + \frac{u_{*0}}{U_{10N}} \right)^2, \qquad\qquad (2.2\text{n})$$

the neutral drag coefficient would asymptote to 3.8 x 10^{-3}. While he acknowledges that this number is larger than the results of other recent studies involving TC force winds [28], including each of the modern parameterizations used herein, the fact that it does show an asymptotic behavior based on limited wind measurements above gale force promotes further confidence in its use for lower values and helps to confirm the theory of a saturating drag coefficient. Furthermore, Edson also explicitly states the use of his parameterization is unlikely to hold under TC forcing, but has clarified that it can be utilized in studies such as this by asymptoting to that found by Donelan (J. Edson, personal communication, July 15, 2018). This formulation of C_{DN}, which is titled Coupled Ocean–Atmosphere Response Experiment (COARE) 3.5 (referred to as C3.5 in subsequent chapters) [28], was selected for this study for being the most comprehensive parameterization, at least up to wind speeds of storm force.

2.2.7 Hwang (2018)

In the final and most recent investigation of the drag coefficient used in this study, Hwang acknowledged the challenges and limitations of making near surface measurements in TC force winds. As a result, his approach relied on microwave remote sensing to measure surface roughness and whitecaps to ultimately parameterize the drag coefficient as a function of wind speed. In general, regardless of the transport mechanism (e.g. satellite or airplane), microwave radiometers accurately measure the brightness of the sea surface (T_B), which is affected by roughness and whitecaps at high winds. The specific formulation of T_B is beyond the scope of this study, but physically is a function of the SST and emissivity of polarization, the latter of which itself is a function of the water-side relative permittivity (i.e. how well and much the water stores entrained air following wave breaking) as well as wind speed [27]. In order to parameterize these processes, previous studies related the whitecap coverage (W_c) on the sea surface to wind stress via the friction velocity [29], as given by

$$W_c = \begin{cases} 0, & u_* \leq 0.11 \frac{m}{s} \\ 0.3(u_* - 0.11)^3, & 0.11 < u_* \leq 0.4 \frac{m}{s} \\ 0.07 u_*^{2.5}, & u_* > 0.4 \frac{m}{s} \end{cases} \qquad (2.2\text{o})$$

While this relation of W_c to C_D via equation (2.2d) had been completed by Hwang before, in this study, he aimed to use field measurements from within hurricanes in order to improve or validate prior formulations. To do so, Stepped Frequency Microwave Radiometer (SFMR) data taken from a total of 370 USAF and NOAA hurricane reconnaissance flights were incorporated to specifically fit measured T_B and the corresponding W_c with the wind-derived W_c, which is a function of C_D via equation (2.2d) [27]. Based on the data analysis, Hwang determined that his previous parameterization was inaccurate for wind speeds of about 51 m/s and refined such using a least squares fitting of the aforementioned data [27], as given by

$$C_{D\_Hwg} = \left(8.5 + 9.48(U_{10}/11.411)e^{-U_{10}^2/1483.49}\right)x10^{-4}. \qquad (2.2\text{p})$$

These results, which were predicated on the use of SFMR data—the only measurements above 45 m/s in this study, also indicate the intuitive relationship between whitecap coverage and wind speed in which W_c increases with U_{10} [27]. This parameterization, which falls between the magnitudes of such by Powell and Zijlema, was chosen due to its critical use of USAF SFMR data as well as its distinct method of measuring wind speeds at TC force and inherent relation to sea surface effects under this forcing.

2.3 Comparisons of Drag Coefficients

Each of the eight drag coefficients are distinct and take-on noteworthy shapes as a function of wind speed. As such, it is prudent to display and describe their features on a single chart, Figure 2-1, and any nuances used for application herein. Initially, each of the parameterizations take on a similar value prior to forming their distinct shapes, which will be described in the order they were initially presented below, with the exception of the intuitive constant C_D. First and second, Garratt's and Wu's formulations of the drag coefficient, taken together, have a very distinct shape by linearly increasing with U_{10} and while they take on similar values as the others for wind speeds less than 20 m/s, they then quickly grow to 100-200% of the others, by 60 m/s. Due to
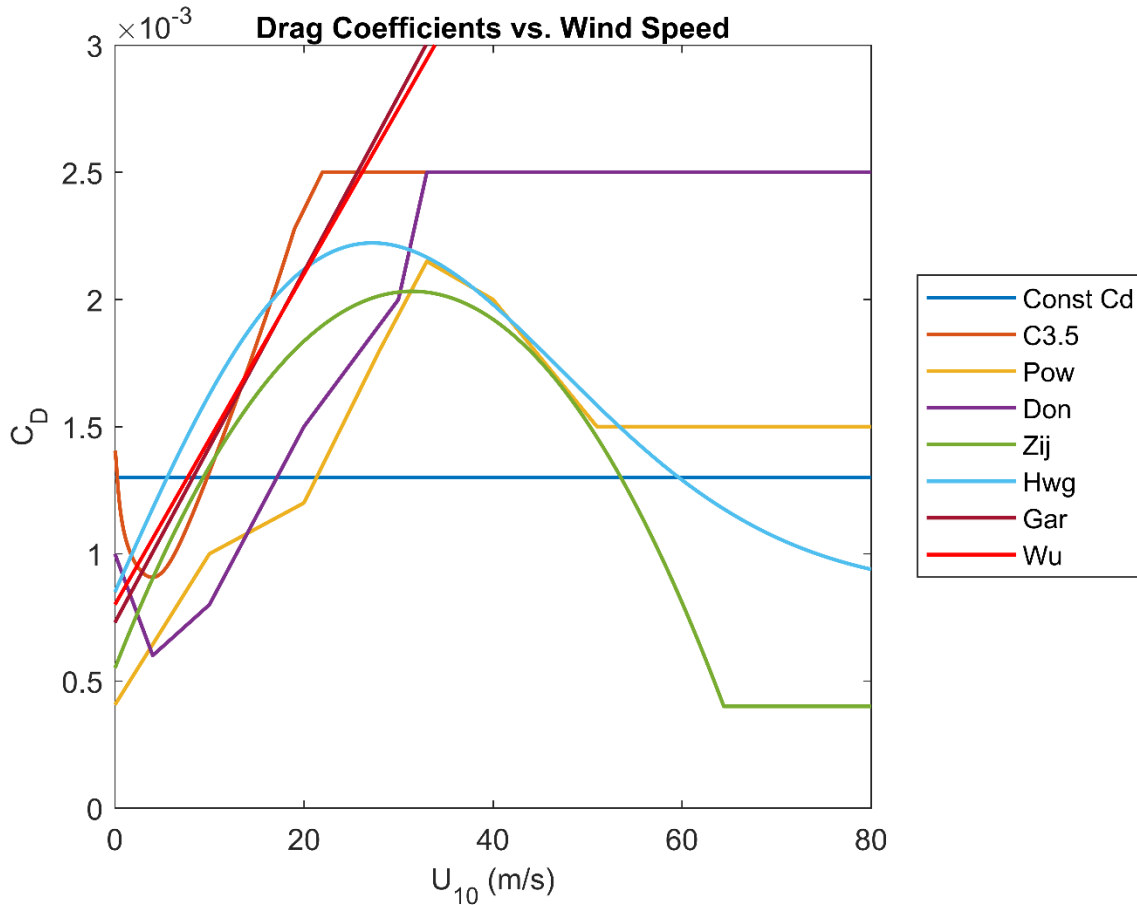
Figure 2-1: Drag coefficient vs. wind speed [m/s] for all parameterizations discussed in Section 2.2 and used in this study, which are abbreviated as the following: Constant C_D – "Const Cd," Edson – "C3.5," Powell – "Pow," Donelan – "Don," Zijlema – "Zij," Hwang – "Hwg," Garratt – "Gar" and Wu.

their similarity, as mentioned in Section 2.2.2, Garratt's version of C_{DN} was selected to represent each, as well as many other legacy publications, in this study. Third, Powell's finding for C_{DN} increases with wind speed up until 33 m/s, where it maximizes, and then begins to decrease, most drastically between 40-51 m/s. After this point, Powell's data is limited and while he did not specifically publish a form for C_{DN}, he indicated a saturation of, rather than rapid decent, of the drag coefficient. As such, the parameterization used herein includes a horizontal asymptote at 1.5 x 10^{-3}, which is the minimum of his plotted measures of C_{DN} under TC force. Fourth and fifth, Donelan's and Edson's (taken out of order due to similarity) formulations for C_{DN} have very similar shapes, with an initial decrease and minimum at approximately 3-4 m/s, then increase to a drag coefficient of 2.5 x 10^{-3}, where each asymptotes. The preliminary decrease in

the drag coefficient can physically be attributed to viscous stress dominating under light wind and swell conditions, but as the winds increase and the seas become fully rough by 7.5 m/s, wind waves dominate the surface roughness, causing the drag coefficient to continually increase [28]. While Donelan's C_D increases from 3-33 m/s, Edson's C_D increases from ~3-22 m/s, upon which each asymptotes; Donelan's arrival at this limit was based on his data analysis, but Edson's was attributed to his formulation not being explicitly valid under TC force winds, as described in Section 2.2.6. Sixth, Zijlema's parameterization of C_D parallels some of the other modern approaches up to approximately 50 m/s, upon which it continues to decrease until bounded at 0.4 x 10^{-3} for wind speeds greater than 64.4 m/s. Lastly, the seventh parameterization for C_D is that of Hwang, which increases up to 25 m/s, maximizes, and then decreases to an asymptote of just under 1 x 10^{-3}. In total, by applying equation (1), the strongest wind stress under TC forcing is represented by Garratt, then Donelan and Edson, with the order of the remaining four varying as function of a storm's specific strength.

Chapter 3

Sea Spray

3.1 Generation and Types of Sea Spray

There are three different types of sea spray that are characterized by the process by which they are generated. The first two categories are formed from a three step sequence where air is entrained into the water by some process (e.g. wave breaking), then the submerged air bubbles rise to and through the sea surface, where they break. When these air bubbles reach the surface, water on the skin of the sea is displaced and *film* droplets are forced into the atmosphere. Subsequently, upon the breaking of the bubbles, their cavities are immediately filled by water, which forces *jet* drops from the sea to the atmosphere [30]. Film and jet drops range in initial radius from 0.1-5 μm and 3-100 μm respectively [31]. The remaining two types of sea spray, communally known as *spume* drops, are formed directly as a result of waves and are not dependent on entrained air bubbles. This type of sea spray either forms when winds (of approximately 7 m/s or greater) shear off a portion of wave crests or when waves curl over and break, both ejecting airborne spray [30]. Spume droplets, whose population density and volume dominate at high wind speeds, have a minimum initial radius of 20 μm and can be much larger [31], [32].

Although these spray drops are often tiny, even in light winds there are numerous and under TC forcing, they can play a pivot role in controlling the storm's maintenance and development. While it is not the focus of this study, many investigations involving sea spray and TCs have aimed to characterize the enthalpy flux, thus lending insight to, or deriving a relationship with, storm intensity [17]. In fact, Andreas, whose work will be the chief contribution to sea spray theory used herein, conducted such a study with Emanuel [33] and made a key finding with respect to re-entrant sea spray and TC intensity. Physically, they determined that sea spray almost immediately transfers sensible heat from the warmer ocean to the cooler air, but falls back

into the water in a matter of seconds before it can completely evaporate and exchange latent heat, thus representing a tangible change in the net enthalpy flux across the boundary [33]. (In many prior studies, the effect of sea spray had been deemed negligible as the change in the *net* enthalpy flux across the air-sea interface would be zero if all of the drops were to evaporate, which is not the case following their re-entry to the water [33].) Using this new application, Andreas and Emanuel determined that the inclusion of sea spray in the enthalpy, as well as momentum fluxes, lead to the most intense storms [33], indicating the criticality of its parameterization in TC modeling. As above, the role of sea spray in enthalpy transfer is not central to this study, but is included to provide context to its overall importance and original research motivation with respect to TCs. With that being said, Andreas and Emanuel did include its effect on momentum flux in their model, which will be detailed below and is a principal component of this study.

3.2   Momentum Transfer

When sea spray (of any form) enters the atmosphere due to the forcing of a TC, it quickly accelerates and approaches the speed of the extreme horizontal wind, before most of it subsequently plunges back into the ocean in a matter of seconds. For the atmosphere, the spray acts as a drag as there is a transfer of momentum from the fast flowing air to the initially much slower moving water particles. For the ocean, upon reentry into the water, the spray transfers this gained momentum from the air to the sea [33]. This fairly intuitive process, which is often unaccounted for, may be significant in characterizing the total stress imposed by TCs on the upper ocean. Introducing the effect of sea spray within the wind stress, which traditionally is a function of ρ, U_{10} and C_D (as defined by equation (1)), would only slightly affect the magnitude of the latter two parameters, but the density of the droplets would be up to three orders of magnitude larger than that of air. As a result, a parameterization of sea spray and total stress accounting for this discrepancy is paramount to this study and will be discussed in the following section.

3.3   Parameterization of Sea Spray

3.3.1 Spray Generation Functions

While there are many approaches to parameterizing the stress caused by sea spray through momentum transfer from the atmosphere to the ocean, utilizing familiar terms is key as it helps to provide a foundation of physical intuition into the process as well as allow for seamless application in current and future models. Andreas and Emanuel took such an approach by defining the spray stress as a mass flux (per unit volume) [33], as given by

$$\tau_{sp} = \frac{4\pi}{3}\rho_w u \int_{r_{lo}}^{r_{hi}} r_0^3 \frac{dF}{dr_0} dr_0, \tag{3.3a}$$

where $\frac{4\pi}{3}r_0^3$ is the volume of spherical spray drops, u is the wind speed one significant wave height above the mean sea level, and $\frac{dF}{dr_0}$ is a spray generation function, integrated from film and jet droplets (r_{lo} = 1 µm) to large spume drops (r_{hi} = 500 µm) [33]. This formulation contains several embedded assumptions including that all spray drops are spherical, those within this dimensional interval accelerate to within e^{-1} of the horizontal wind speed before re-entering the ocean and droplets outside the interval are either small enough to remain suspended in the atmosphere or larger enough to return to the ocean before substantially accelerating [33]. In addition, the spray generation function, which is the only portion of equation (3.3a) lacking an intuitive physical base, must be addressed. Andreas, amongst a series of other scientists in separate studies, aimed to develop a reliable spray generation function in the late 1980s and throughout the 1990s. In particular, he formulated two separate functions that would go on to be used to further parameterize spray stress. While the specific details regarding the exact nature of these formulations go beyond the scope of this study, they will be briefly considered below. First in 1992, Andreas aimed to go beyond the other spray generation functions to date by extending their applicability to well within the spume drop radii due to their importance in TCs [31]. In addition, many of the previous investigations were founded based upon tank simulations, but he aimed to improve their findings using Wu et al.'s [34] spray measurements from optical sensors on an ocean-deployed raft [31]. Using near-surface droplet concentration spectra, Andreas fit the data in a piecewise form by drop radius, which now ranged from 15-250 µm, and as a function of $5 \leq U_{10} \leq 20$ m/s [31]. While this parameterization was a great

improvement in terms of its accounting for spume drops, Wu et al.'s data was limited by the measured wind speeds, which maximized at 8 m/s, not strong enough to produce high concentrations of spume [33]. In order to address this, Andreas conducted a second investigation in 1998 where he merged and fit the spray generation functions of Monahan et al. (1986) and Smith et al. (1993). The former, which was based upon tank simulations, was regarded as the most accurate for film and jet spray drops [35], while the latter was formulated using Eulerian, 10 m oceanic tower data, which contained maximum wind speed measurements of approximately 30 m/s and consequently accounted for spume drops up to 50 µm [36]. Andreas aimed to marry these together using a least squares fit in their interval of overlapping wind speed (5-20 m/s), but also believed the larger spume drops would be too massive to reach the elevation of the 10 m tower sensors. As a result, his final parameterization was continuous, but again split piecewise by drop radius and a function of $0 \leq U_{10} \leq 32.5$ m/s, which generally accounted for the film and jet drop radii, spume drop radii up to 20 µm, and spume drop radii from 20-500 µm by applying the following respective formulations: Monahan et al. [35], Smith et al. [36] and Andreas (1992) [32]. Using his 1992 and 1998 parameterizations, he formulated an equation for spray stress as a function of a familiar term—u_*.

3.3.2 Wind and Spray Stresses

Using equation (3.3a) and the two aforementioned spray generation functions, Andreas and Emanuel plotted those as a function of u_* [33], while also comparing their shapes to that of the wind stress alone, which is given by

$$\tau_w = \rho u_*^2 \tag{3.3b}$$

after combining equations (1) and (2.2c). In order to arrive at equation (3.3b), as well as evaluate τ_{sp} from equation (3.3a), a drag coefficient must be assumed, which in this case, they applied Large and Pond's formulation [33], [37], as given by

$$C_{DN\_LP} = \begin{cases} 1.2, & 4 \leq U_{10} \leq 11\frac{m}{s} \\ 0.49 + 0.065U_{10}, & 11 < U_{10} \leq 25\frac{m}{s} \end{cases} \tag{3.3c}$$

This parameterization of C_{DN} represents another legacy variety that after 11 m/s, is parallel to Wu's (equation (2.2g)) and nearly identical to Garrett's (equation (2.2f)) and like that of the

latter, contains an upper boundary in winds of approximately gale force. However, like Wu, Andreas and Emanuel have applied this to an unbounded series of friction velocities, to include those of TC force. When comparing the shapes of the two spray and wind stress functions against u_*, they made several observations including that τ_w and τ_{sp} had quadratic and fourth power relationships respectively with u_*. In addition, under low wind forcing, τ_w was much greater than τ_{sp}, but these values took on similar orders of magnitude under TC forcing, with τ_{sp} surpassing τ_w at approximately 60 m/s—a category four TC [33]. Using these three functions, Andreas and Emanuel estimated a parameterization for spray stress as a function of u_*, as given by

$$\tau_{sp} = 6.2x10^{-2}u_*^4, \tag{3.3d}$$

where the leading coefficient is dimensional $\left[\frac{kg\,s^2}{m^5}\right]$ [33]. To provide stronger physical intuition and align equation (3.3d) with (3.3b), adjusting the leading coefficient to include the density of water (ρ_w) approximately yields

$$\tau_{sp} = 6.2x10^{-5}\rho_w u_*^4, \tag{3.3e}$$

where the leading coefficient is altered dimensionally $\left[\frac{s^2}{m^2}\right]$.

In this study, separating and combining the wind and spray stresses as well as forming them as a function of the drag coefficient (as above in equation (3.3b)) is paramount. In doing so, a comparison between the upper oceanic response with and without the inclusion of sea spray can be made easily via application within model simulations. To illustrate this as well as attempt to validate the above conclusions made by Andreas and Emanuel, Figure 3-1 depicts τ_w and τ_{sp} vs. U_{10} using the seven drag coefficients presented in Section 2.2. Using Garratt's drag coefficient as a case study, all of Andreas and Emanuel's observations are evident as τ_w is much larger than τ_{sp} under low wind forcing, but since the latter does increase more rapidly (i.e. is proportional to $u_*^4 \propto U_{10}^4$ via equation (2.2c)), τ_{sp} approximately reaches the same order of magnitude as τ_w under TC wind forcing, eventually surpassing it at 70 m/s—also a category four TC. This legacy drag coefficient was selected as a case study because it is the only one in which all of the aforementioned observations are matched. In fact, through the domain of Figure 3-1, which approaches the wind speed of some of the strongest observed TCs on record, none of the modern
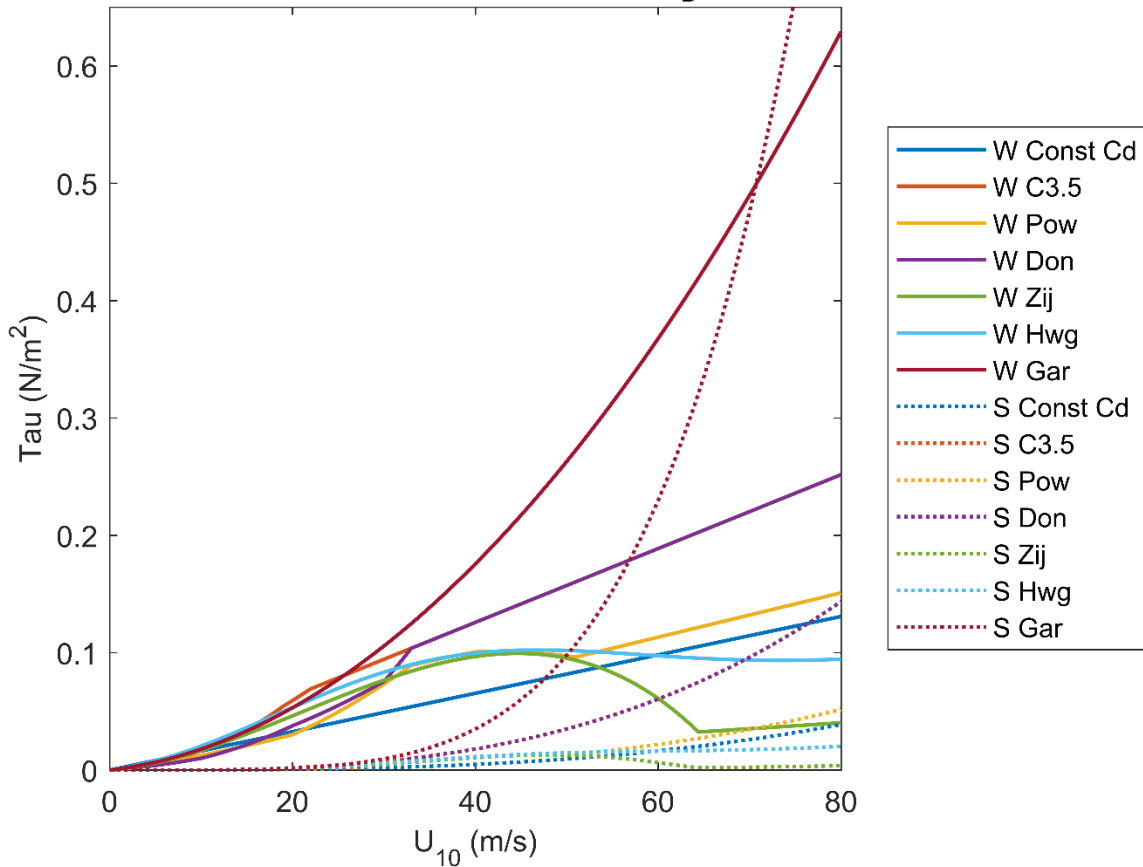
Figure 3-1: Separated wind (τ_w) and spray stresses (τ_{sp}) [N/m^2] vs. wind speed (U_{10}) [m/s] for all C_D parameterizations discussed in Section 2.2 and used in this study. Solid and dotted lines represent modeled output with wind-only ("W") (τ_w) and spray-only ("S") τ_{sp} forcing respectively.

parameterizations show a quadratic or higher order relationship with respect to U_{10} or u_* and only the two strongest formulations, those by Donelan and Edson (C3.5), eventually indicate similar orders of magnitude between the wind and spray stresses. The implications of this discrepancy between the legacy and modern drag coefficient parameterizations, with respect to τ_w and τ_{sp}, will be addressed below.

3.3.3   Over or Underestimation of Wind with Spray Stress?

Based on these findings in which only the legacy parameterizations of the drag coefficient match the related formulations of sea spray stress as well as the manner in which these will be applied to model formulation (to be discussed below), preemptively considering the relative outcome of

this study's results is warranted. Beginning with the spray stress parameterization as given by equation (3.3e), Andreas and Emanuel argue this may provide a lower bound on τ_{sp} as its formulation only considered spume drops up to a radius of 500 μm [33]. While larger drops would not stay in the air as long due to their size, spume drops can be much greater than 500 μm and those would still play a role in further enhancing momentum transfer from atmosphere to the ocean. With that said, however, their parameterization was developed from a legacy drag coefficient formulation. As such, since the friction velocity can be expressed as a function of C_D (equation (2.2c)), the resulting spray stress with a legacy drag coefficient yields a large value, acting more as an upper boundary. Next, the implementation of τ_w and τ_{sp} in model simulations also warrants a boundary discussion with respect to assessing wind *and* spray vs. wind *only* stresses. With individual parameterizations for both wind and spray stresses, in 2001, Andreas and Emanuel added these together to form a total stress [33], which was used in the aforementioned TC intensity model results (Section 3.1). Three years later, however, arguing that such a technique violated the conservation of momentum, Andreas revised this initial approach by defining the total stress as the previous τ_w and rather than adding an additional spray stress term, partitioned the total stress as that caused by air and spray, but not to increase beyond τ_w [19]. In order to do this, rather than using a bulk formula for each stress parameter, he allowed each to have a vertical dependence, naturally letting the effect spray be largest near the surface [19]. While this approach is certainly credible, there are a few reasons why it was not incorporated in this study. First, as will be expounded upon in Chapter 4 below, PWP is an ocean model lacking a vertically dimensional atmosphere in which such stress parameterizations could be effectively implemented. Second, as mentioned in Section 3.2 above, stress as a result of spray cannot be accurately parameterized using the density of air, as would be the case if only equation (3.3b) was used as the total stress parameter. While the author is in agreement with Andreas' argument that momentum conservation is likely violated when purely adding τ_w and τ_{sp}, the 2-3 order of magnitude density difference between air and spray droplets must also be considered. Furthermore, it is believed that when spray is introduced, while the magnitude of the wind stress likely decreases, obviously the magnitude of spray stress goes from zero to some appreciable value, but the total stress would be larger with spray, which is contrary to Andreas' revision. Based on the above, Andreas and Emanuel's first approach will be applied herein in which the total stress including spray will be expressed by

$$\tau_{w\&s} = \tau_w + \tau_{sp} \qquad\qquad (3.3f)$$

and that without spray will be expressed as τ_w, as previously defined.

Based on these factors related to a lower or upper boundary of total stress when including sea spray, the results of this study will serve as an upper boundary or possible over-estimation. If it is assumed that the effects of the absence of large spume droplets is generally balanced by the use of strong, legacy drag coefficient parameterizations in the formulation of τ_{sp}, the potential "addition" of momentum via equation (3.3f) points to an upper boundary of the total stress. As such, this expectation must be considered during data analysis and if it is determined that the inclusion of sea spray either consistently overestimates or improves the model accuracy of oceanic variables as compared to measurements during TC passage, to a statistical significance, additional studies would be needed to more precisely derive the total stress. However, if the addition of spray stress over *and* underestimates and does not improve model accuracy of oceanic variables as compared to measurements, then this study's parameterization of the total stress will sufficiently point to sea spray being negligible in terms of TC modeling of its momentum flux into the ocean.

Chapter 4

Oceanic Response to Tropical Cyclone Passage

4.1   Experimental Design

The primary methodology applied in this study involved comparing measured upper oceanic variables, to models of those same variables, under varying stress forcing (e.g. several drag coefficients and with and without sea spray), following the passage of real and parameterized TCs as summarized below in Table 4.1. The following section will discuss both measurement platforms used herein—ALAMO floats and a Navy Littoral Battlespace Sensing glider, followed by a detailed description of the PWP model and its specific uses in this study.

Summary of TC Characteristics								
Storm	Year	Basin	Vmax [m/s]	Rmax [km]	Translation Speed [m/s]	Translation Bearing [°]	Latitude [°N]	Inertial Period [hrs]
Ignacio	2015	Central Pacific	56.5	28	4.3	326	18.2	38.3
Irma	2017	Western Atlantic	81	28	6.8	270	16.9	41.2
Florence	2018	Western Atlantic	54	28	5.5	294	22.4	31.4
Michael	2018	Gulf of Mexico	59	28	6.2	356	27.6	25.8

Table 4.1: Summary of the TC Characteristics of the four HUs, at the time of CPA, used in this study. *Vmax* and *Rmax* respectively refer to the magnitude and radius of the maximum wind velocity.

4.1.1   Submersible, Upper Oceanic Measurement Devices

In situ surface and oceanic measurements under TC forcing are few and far between due to general safety and sensor limitations. Ordinarily, many surface and upper oceanic measurements

are made by ships, but in the face of an approaching TC, many of the strongest hulled research and United States Navy (USN) and Coast Guard (USCG) vessels are not equipped to withstand sustained winds and significant wave heights over 50 miles per hour and 20 feet respectively— and neither of which would even qualify as TC force. In addition, the majority of these data are captured by "ships of opportunity" and not those specifically outfit to potentially endure such an event, and as a result, weather-risk avoidance ship routers and captains alike would steer well clear of such rough, possibly damaging and deadly systems to seek fair winds and following seas. Floating and moored buoys are another of the major players in such measurements, but as with the ships, they struggle to withstand the extreme winds and high seas without sensor or communication malfunction. With surface-based platforms largely unreliable, airborne and subsurface devices must be considered. From the air, satellites and radiometers can reliably measure and/or parameterize surface features such as wind speed, significant wave height and SST to name a few, but nothing below the first few meters of the mixed layer. Finally, when pondering subsurface platforms, there are several viable options for measuring the upper ocean, but it is important to consider the very specific nature of TCs; the desired platform must be able to measure directly beneath a passing storm, as often as possible, without requiring ship deployment due to the aforementioned challenges. Argo floats, which are autonomous, Lagrangian devices that profile the ocean worldwide, have been the standard in such a measurement method for the last 20 years. These floats are primarily designed to measure temperature and salinity, but to a depth well-beyond that of the mixed layer, and at a low frequency (ten days per profile), allowing for an extended life (four to five years) [38]. In addition, Argo floats are relatively large and heavy devices, designed for sustainment, making their deployment platform primarily shipborne. As a result, for pronounced utility in TC measurements, scientists would have to be extremely fortunate to gain great insight from an Argo float as it would have to had meandered into the track of a TC and be in the mixed layer near the time of its passage. Even so, the Argo array, at one float per 3x3 degree box every ten days, is too sparse in space and time to observe the ocean response to TCs. Thus, the need for a submersible device designed to measure the mixed layer, in a rapid fashion, at a specific, on-demand location, was present—enter the ALAMO float and Navy Littoral Battlespace Sensing glider.

4.1.1.1 ALAMO Floats

The vehicle for the majority of the directly measured data in this study (from HUs Ignacio, Irma and Florence) can be attributed to the ALAMO float, which sports several technological advancements from legacy systems of its kind. Two of those developments, including an electronic communication system with internal time and specific size design, were paramount to the success of this analysis. First, the ALAMO's electronic communication system and internal time (i.e. clock) allow for remote programming of float profiling speed as a function of time [5]. This feature optimizes the floats utility by allowing for a series of "rapid" profiles to be executed before, during and after the CPA between the float and a passing TC. In addition, ALAMOs can also be remotely programmed to limit their maximum profiling depth of 1000 m [13] to approximately 200 m, allowing for exclusive measurement of the mixed layer during TC passage. In tandem, the float can relay its measured data in real-time via the Global Telecommunications System (GTS), traditionally used by forecast centers, for immediate assimilation to ocean models. Second, the dimensions of the ALAMO match those of an "A-size" sonobuoy and along with associated air-deployment rigging and a parachute [5], allow for dispersal from USAF WC-130J Hurricane Hunter aircraft. Accordingly, this characteristic permits the deployment of floats from a relatively safe platform (e.g. aircraft designed and rated to withstand TC force winds and associated turbulence as opposed to exposed, unrated ships) directly to the location of the storms, which is not attainable using traditional Lagrangian floats such as Argo. The specific tactics employed by these aircraft during missions are robust and not necessarily pertinent to this discussion; however, in general, floats are deployed from the stern buoy chute during radial routes towards a storm's eye, from an altitude between 500 and 10,000 feet. After exiting the aircraft, the aforementioned profiling settings can be adjusted, but otherwise the float is autonomous and relays measures of temperature (and salinity, but not applicable to this study) as a function of pressure via the GTS for model ingestion and/or subsequent case study analysis.

While there is no preset number of ALAMOs deployed during each storm, they are generally allocated based on two factors—data potential and USAF operational availability. First, data potential is often maximized when storms are strong, located over deep water and away from land, and forecasters have a high confidence in their track and ability to sustain intensity. Simply

put, there can be greater return on investment when the storm is not going to fall apart or immediately shift away from the deployed float. Second, these and other ocean-measurement devices are deployed during USAF tasked reconnaissance missions, which do not have defined orders to measure the ocean, rather the storm's atmospheric characteristics (e.g. pressure, maximum wind speed and radius, movement, etc.) above the water. As such, not every mission is going to allow for the optimal placement of an ALAMO float. Since the initial ALAMO deployment during a USAF storm flight in 2014, the average number of floats released per storm has continued to increase [13]. While this is partially a result of the data potential, an ever larger consideration must be ascribed to ever-increasingly strong relationship being forged between the USAF Hurricane Hunters and USN and USCG oceanographic researchers. Based on this, the initially nominal 1-2 floats per storm increased to four in HU Guillermo (one of which interacted with HU Ignacio, as stated in Section 1.1), eight in HU Irma and ten in HU Florence. In the latter two storms, as part of the return route, the USAF crews agreed to fly special tracks designed to deploy those 18 floats, approximately 25 km apart, in a line perpendicular to the forecast storm track.

Summary of Float and Glider Measured Data					
Storm	Floats/Gliders Deployed	Profiling Depth [m]	Hours of Data (Relative to CPA)	Float/Glider PWP Grid Positions	CPA to Storm [km]
Ignacio	1	200	-12-76	9077 / (0,-1)	-5.0
Irma	8	200	-9-70	9129 / (0,-5)	-26.9
				9134 / (1,6)	30.4
Florence	10	200	-12-60	9136 / (-2,10)	51.0
				9141 / (-1,15)	75.2
Michael	1	~100-210*	-10-70	NG 288 / (0,10)	50.0

Table 4.2: Summary of ALAMO float and Navy glider measured data incorporated into this study. *While the profiling depths were fixed for the ALAMO floats during storm passage, the Navy glider's was not and the maximum depth of each profile varied throughout. For the PWP grid positions, which are partitioned into 5 x 5 km^2 boxes, the storms' tracks were rotated to align with the x-axis, with the origin representing the storms' positions at CPA. As such, positive and negative x grid points represent the horizontal distance behind and ahead and positive and negative y grid points represent the distance right and left, respectively, of the storms' CPA positions. For the CPA to the storms, the magnitude of the grid positions was computed, with positive and negative values indicating left and right of track respectively.

With such a dataset, the ability to compare the oceanic response from the left, center and right side of the storm is possible. This seemingly simple set-up is extremely valuable in such

measurements due to the asymmetry associated TCs based on the hemisphere and their track bearing. For example, a Northern Hemisphere (NH) storm, translating from south to north, would impart more stress on the ocean on its right side as the cyclonic wind motion would add to northerly translation speed, but subtract on the left. In addition, from a Eulerian perspective, a surface object (e.g. free floating buoy) positioned to the northeast of the storm would generally experience the following sequence of directional wind stress forcing through TC passage: southeast, south, southwest and west. As a result, the object would be forced northwest, north, northeast and east, ultimately following a clockwise pattern. Separately, also in the NH, the Coriolis effect directs movement to the right and as such, inertial currents form as a result of wind stress and have a clockwise rotation. During the passage of a TC, these two effects resonate, scaling along the storm track as the approximate product of the translation speed and inertial period [39]. Since the wind stress acts in the opposite direction on the left side of a storm's track, these aforementioned effects only resonate on its right side. Overall, with stronger wind stress forcing and inertial current resonation only on the right side of the storm, it is of course worthwhile to measure on that side where the mixed layer is expected to deepen the most, especially near the radius of maximum winds, but also paramount to compare data from left and center in order to discover trends, relative responses, CPA dependency, etc. Furthermore, placing several floats ahead of multiple storms allows for cross-comparison as a function of storm strength, latitude and translation speed. In the end, a great deal of gratitude is owed to the USAF Hurricane Hunters, as without their flexibility and dedication to improving TC forecasts through oceanographic measurement, the 19 float complete dataset used herein would not have been possible.

After considering the entire data set, five ALAMO floats were chosen for this study, as listed above in Table 4.2. When pairing those down, the following considerations were made. First, any floats that either failed to report measurements over at least three full days or were deployed at a significantly different time than the other floats in a given storm were neglected. To determine the latter, a CPA time was established for each TC that was defined as the time when the storm reached its minimum distance to the device, based on a dead-reckoned average

Figures 4-1a, 4[...]
Interaction between a)[...]
Irma and ALAMOs 9[...]
9134 and b) HU Floren[...]
ALAMOs 9136, 9141[...]
The left image displays t[...]
of the storm's track [...]
modeled area of over [...]
speeds in 34, 50 and [...]
thresholds as well as the [...]
of each ALAMO, from [...]
deployments to final pr[...]
right image zooms i[...]
interaction and labels th[...]
position of the first and [...]
used in this analysis an[...]
between the storms and floats.
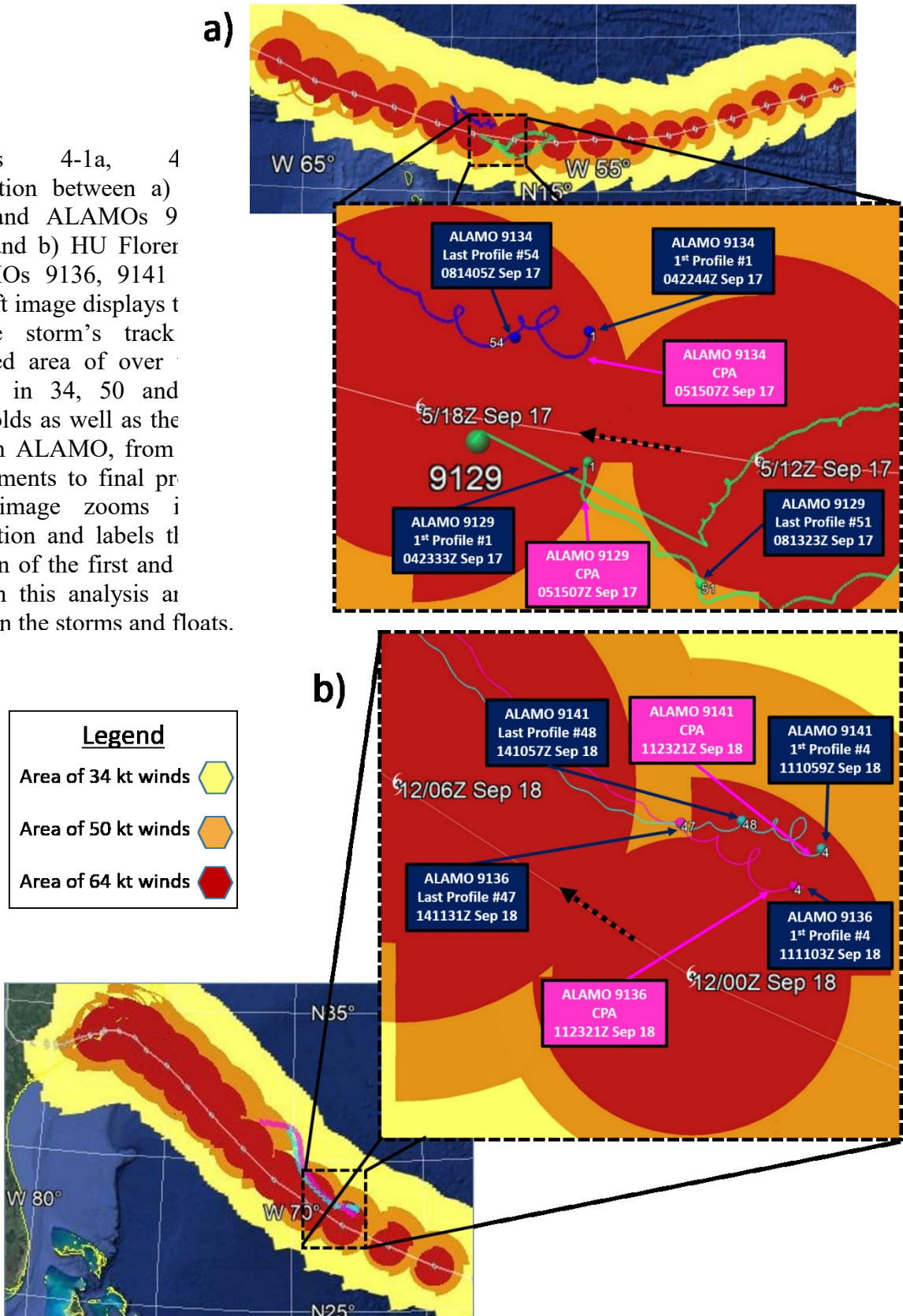
translation speed between the appropriate, adjacent six hour fixes. This process was held exactly for the single device storms (e.g. HUs Ignacio, Michael), but was slightly altered when several floats were deployed (e.g. HUs Irma, Florence); in this case, since the floats were dropped in an approximately perpendicular line to the storms' tracks, the CPA times were determined by their intersections. In the case where a single float was deployed after the established CPA time for a given storm, it was ignored. Second, including data from as many different storms as possible was desired, which would have elicited the use of ALAMO 9077 from HU Ignacio alone, but its incorporation can more aptly be attributed to the overall motivation of this study, as described in Section 1.1. Third, coupling the measured oceanic response with the modeled output in terms of the time (with respect to the CPA) and shape was considered. While almost all of the floats' data was viable based on this criterion, those that were significantly, visibly different from both the model and other results for a given storm were omitted. Finally, as alluded to above, floats with varying CPAs left, right and nearest a storm's track were desired. Based on these four main criteria, five floats were selected, two in HUs Irma and Florence as illustrated in Figures 4-1a and 4-1b, which overall included CPAs from approximately 27 km left to 75 km right of the storms' tracks, with a near direct hit by HU Ignacio.

4.1.1.2 Navy Littoral Battlespace Sensing Glider

ALAMO floats do an exceptional job of measuring the oceanic response beneath TCs, but are somewhat limited in three ways. First, presently, they are deployed by USN or USCG personnel onboard the USAF storm reconnaissance flights and currently, an oceanographer is not billeted or required on these missions. Furthermore, the oceanographic team only accompanies the USAF on 2-3 storm flights per year, depending on the data potential and logistical factors. Second, while the floats are not single-use profilers (e.g. airborne expendable bathythermograph tracers (AXBTs)), they are generally "one and done" in that they are used for just one storm, then meander on their own accord until battery depletion. Third, they are relatively expensive and when combining the last two factors, their inventory is inherently limited. Overall, based on these factors, another submersible platform is paramount to supplement with a similar dataset, which can sometimes be provided by USN gliders.

Navy Littoral Battlespace Sensing unmanned underwater vehicles, also known as gliders (and will be referred to as such onwards), are submersible devices capable of measuring temperature,

salinity, velocity and more oceanic variables through the mixed layer and beyond. Unlike the floats and buoys, these are propelled vessels capable of travelling hundreds of miles within their long-duration, 4-6 month deployments, before requiring a battery recharge [40], [10]. Navy gliders are both deployed and recovered by one of the seven NAVO Tactical Auxiliary General Surveillance ships, which are forward deployed environmental measurement platforms whose data is used to update navigational charts, map the bottom of the ocean and feed atmospheric and oceanographic models, amongst many other applications. In addition to deployment and retrieval, NAVO also pilots these vessels within its Glider Operations Center, which is manned 24 hours a day. As such, Navy gliders are able to profile as prescribed and/or commanded, to include rapidly within the mixed layer, in many ocean basins across the world; the ability to
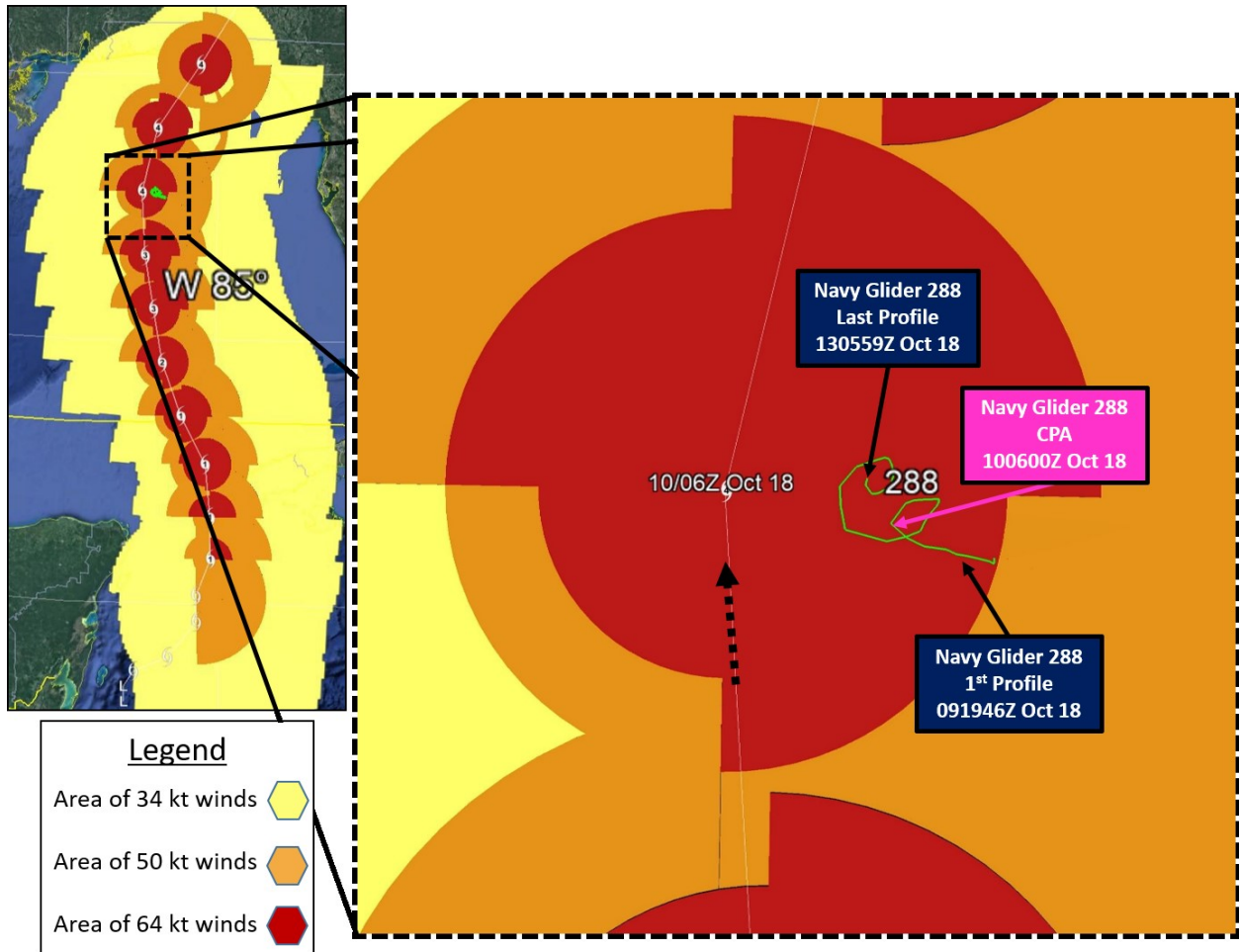
Figure 4-2: Interaction between HU Michael and Navy glider 288 [12]. The left image displays the majority of the storm's track with the modeled area of over water wind speeds in 34, 50 and 64+ knot thresholds. The right image zooms in on this interaction and labels the time and position of the first and last profiles used in this analysis and the CPA between the storm and glider.

already be underway and navigate directly to the storm allows these vessels to safely measure the upper ocean during TC passage.

These vessels' utility was on display during the passage of HU Michael through the Gulf of Mexico in 2018. This storm was a weak category one TC on 8 Oct at 12Z, located just east of Yucatan, translating north, northeast at 7.6 knots [12]. Based on the intensity forecast in which 89% of models predicted the storm to only intensify by one category [41], in addition to the relatively rapid translation speed and time of year, the data potential and logistical challenges were limited and difficult respectively, ultimately influencing the oceanographers' decision to pass on dropping ALAMOs and AXBTs in HU Michael. 42 hours later, however, the storm had intensified to a category four TC, now translating at north at 12.1 knots, and was primed to make landfall as a category five storm in western Florida [12]. In retrospect, there was great data potential in this storm, but without the use ALAMO floats, Navy glider 288 was able to supplement. Having been deployed well before the advent of HU Michael, the glider was used as a "device of opportunity" as NAVO piloted as close as possible to the storm, given its previously deployed position in the northeastern Gulf of Mexico. Navy glider 288 conducted a series of profiles, ranging in maximum depth between approximately 100-210 m, recording temperature data (amongst other parameters) roughly 50 km to the right of the storm's CPA position, as illustrated by Figure 4-2.

4.1.2   Price-Weller-Pinkel Model

The Price-Weller-Pinkel (PWP) model, originally developed in 1986 [42], parameterizes the three-dimensional oceanic response to a variety of surface forcing. Initially, PWP was developed to model upper oceanic diurnal processes, with a specific focus comparing buoyant and mechanically-driven turbulent kinetic energy [42]. Given the latter and similar time scales, this framework had already prioritized wind stress forcing, which made its application conducive to TC investigations. Specifically, PWP utilizes ½-order closure to model the response of the oceanic mixed layer to radiative, wind stress and other surface forcing. The applicability and relative simplicity of the model has propelled its use in many studies over the past thirty years, including exclusively herein, with some modifications from the original version. The ensuing paragraphs will review the main components of PWP while detailing the most relevant elements

and/or adjustments made with respect to this study[7], included in the following order: assumptions, prognostic equations, storm development and grid design and forward integration.

4.1.2.1 Assumptions

In any model, there are a series of assumptions and natural limitations that must exist in order for it to resolve the unknowns in the end. The PWP model is no exception and its primary assumptions and associated implications are listed below. First, as with many ocean models, the hydrostatic and Boussinesq approximations are made and the surface is set as a rigid lid. While the first two do not have a major effect on the oceanic response to a passing TC, applying a rigid lid inherently excludes the barotropic response, which is relatively weak in deep water and does not result in vertical disturbances [22], [14]. Second, the initial ocean is assumed to be horizontally homogeneous, thus absent of currents and eddies [22], contains a general oceanic salinity profile regardless of location, and is initialized using a pre-TC passage ALAMO or nearby Argo temperature profile. Depending on the real ocean dynamics in the vicinity of each of the four storms used in this study, a homogeneous ocean could lead to some differences between the measured data and model output. With that said, however, based on the individual storms' intensities and an analysis of global Hybrid Coordinate Ocean Model (HYCOM) data, there were no currents or eddies that had an palpable effect on these four TCs[8], near the established CPA times [12], [43]. Third, the surface atmosphere is assumed to have a respective temperature and dew point of 26°C and 25°C. As a result, the air is nearly saturated, which is certainly indicative of a maritime tropical air mass and that of passing TC, and permits the ocean to act as a heat source as the storms' measured SSTs ranged from 27.7-29.0°C.

Two other key assumptions made in the original PWP model have been adjusted in this study in order to improve the model's accuracy with respect to measured upper ocean data. First, the Coriolis effect is parameterized as a function of latitude rather than assuming an f-plane. While the change in the storms' latitudes during the application of stress on each measurement location is small, systems like HU Michael and Ignacio, with more northerly tracks, were precisely modeled with a varying Coriolis parameter. Second, a frictional term has been applied to diffuse

---

[7] Rather than attempt to reproduce the rigorous, complete, published work of James Price, Robert Weller and Robert Pinkel, only the overall outline, relevant details, and areas of edition will be included herein [22], [42].
[8] Of the four storms studied, HU Michael was the only to interact with a moderate current/eddy near CPA, which was a relatively small warm core eddy and will be discussed in Section 5.2.1.

the inertial response to a period of only five days. Without such an application, the initial stress applied by passing storms would lead to an indefinite inertial response, which is not physically sustainable due to friction and enhances the delta between measured data and model outputs after the preliminary upwelling period. While these additions have been made to ultimately mute these differences, neither change is alluding to errors in the original PWP model, rather are simply specific to the goals of this study.

4.1.2.2 Prognostic Equations

In a ½-order closure model, only the mean prognostic equations are retained and turbulent mixing, in the vertical, is parameterized using the bulk method. In doing so, surface stress is applied and if critical values of the Richardson number are met, based on inputs from those mean equations, the respective layer of water is mixed and the process continues in time and space. Considering only the mixed layer (of the three), the following are the prognostic equations for layer thickness (h_1), temperature (T_1) and velocity (V_1):

$$\frac{\partial h_1}{\partial t} = -\nabla \cdot (\boldsymbol{v}_1 h_1) + W_e, \tag{4.1a}$$

$$\frac{\partial T_1}{\partial t} = \frac{Q}{h_1} - \boldsymbol{v}_1 \cdot \nabla T_1 + \frac{(T_2 - T_1)W_e}{h_1}, \tag{4.1b}$$

$$\frac{\partial \boldsymbol{v}_1}{\partial t} = -f \times \boldsymbol{v}_1 + \frac{\tau}{h_1} - \boldsymbol{v}_1 \cdot \nabla \boldsymbol{v}_1 - \nabla p_1 + \frac{(\boldsymbol{v}_2 - \boldsymbol{v}_1)W_e}{h_1}, \tag{4.1c}$$

where W_e is the entrainment velocity, Q is the heat flux (sensible, latent and radiative) across the air-sea boundary and f is the Coriolis parameter [22]. As illustrated in many of the aforementioned C_D as well as the τ_w and τ_{sp} parameterizations in Chapters 2-3, the PWP model also, yet necessarily computes τ using the bulk method (equation (1)) due to exchanges of momentum happening on much shorter than resolvable space and time scales (to be discussed in Section 4.1.2.4) [22]. As such, the application of varying parameterizations of the drag coefficient coupled with wind stress, with and without spray, was fairly seamless. To do so, beginning with the drag coefficients, each of the seven formulations for C_D was inserted in the following stress computations. For wind stress without spray, τ_w, equation (1) was used. For wind and spray stress, $\tau_{w\&s}$, equations (1), (2.2c) and (3.3e) were combined in the following form, as given by

$$\tau_{w\&s} = \rho C_D U_{10}^2 + 6.2x10^{-5}\rho_w C_D^2 U_{10}^4. \qquad (4.1d)$$

In total, there were 14 different stress forcing combinations run through each of the four storms within this study, resulting in 56 PWP model outputs, from which several upper oceanic response variables will be compared (in Sections 4.2 and 4.3).

As a brief aside, when considering a TC in the deep ocean, it is useful to scale the terms in the momentum equation (4.1c) to discern the main players affecting oceanic motion during storm passage. Upon assuming characteristic horizontal and vertical velocities, length, depths and wind stress [19], when all terms not at the leading order of magnitude are dropped, the only remaining terms are the Coriolis acceleration and wind stress. This exercise, while not applicable to the PWP model, further enforces the importance of wind stress and accurately parameterizing this term, which is one of the primary aims of this study.

4.1.2.3 Storm Development

Within the model, each storm is treated as an anomaly of cyclonic wind stress applied to the ocean below. In order to replicate the four HUs applied in this study or any other storm, the following procedure, which is largely understood, yet undocumented in the TC and ocean modeling communities, can be applied. To begin, there are six primary variables required to develop a storm, all of which are measured by USAF and NOAA storm reconnaissance aircraft as well as estimated via satellite, including the radius and magnitude of maximum wind velocity, profile of wind speed vs. distance from radius of maximum winds, translation speed and bearing and its central latitude. First and second, the radius (R_{max}) and magnitude of maximum wind velocity (V_{max}) establish the storm's basic structure through an approximate Rankine vortex. A Rankine vortex describes a velocity field with solid body rotation up to a specified radius, upon which the flow becomes irrotational [44]. In addition, the velocity increases linearly up to the indicated radius, then decays proportionally to d^{-1}, where d is the distance from the center, eventually approaching zero. This piecewise form effectively models the wind speed in a TC, where winds fall off much faster from R_{max} to the storm's center as compared to R_{max} to a large value of d [45]. The process used herein is only an approximate Rankine vortex, however, where it is assumed the wind speed does increase from the storm's center to V_{max}, located at $R_{max} = d$, linearly; rather than letting the wind speed decay at d^{-1}, however, a measured profile

of wind speed vs. distance from R_{max}, the third variable in this process, is linearly interpolated to more precisely capture the velocity signature of each storm. Fourth and fifth, the storm's translation speed and bearing are used to propagate the TC across the model grid. Sixth, in order to accurately account for the Coriolis parameter, the storm's central latitude is included. For all of the storms used herein, the required data was measured by USAF reconnaissance missions and accessed and/or downloaded via Tropical Atlantic [12].

4.1.2.4 Grid Design and Forward Integration

Dimensionally, the model's horizontal grid is 500 x 500 km^2, with each box measuring 5 x 5 km^2, in order to both sufficiently resolve the oceanic response as well as encompass the TC's wind field [22]. To put those dimensions in perspective, the strongest storm incorporated in this study, HU Irma, boasted a diameter of storm force winds extending 470+ km, during its CPA time [12]. When a storm is translated across the grid, it is done along the x-axis, at a constant speed equal to that at its CPA, regardless of translation bearing, right to left, from a starting grid position centered at (50,0)—250 km right of the origin. The position of the storm's center at the time of CPA is at the grid's origin (0,0), which in the case of HU Irma, took approximately 10 hours to reach. Vertically, which begins at the rigid lid of the ocean surface and works down, the model is divided into layers by 5 m up to 100 m, 10 m up to 200 m, and then by 50 m to 950 m. This vertical grid distribution adequately resolves both the mixed layer and the measured depths of the ALAMO floats and Navy glider as well as considers well into the thermocline.

Naturally, after establishing the spatial dimensions of the model, time should be considered next. Unlike the former, however, the time dimensions were not consistent throughout, rather were adjusted as a function of the strength of both individual storm and the applied wind stress forcing. Notionally, as established in the original version of the PWP, the time step was set at 15 minutes, which would effectively capture the ocean's predominantly inertial response to a passing TC [22]. With the time and space dimensions in place, the model is integrated forward over 87.5 hours (350 time steps), which included at least two inertial periods from model initialization for each TC, by translating the storm by one row of grid points and allowing the ocean to respond to the stress accordingly, followed by adding a new first row with the ocean's initial conditions. Through this process, once a parcel, which began in that first row, is advected out of the grid, a steady-state solution can be achieved [22]. As alluded to above however, this

Summary of PWP Model Runs					
Storm	Drag Coefficient	Wind Only	Wind & Spray	Time Step [mins]	Number of Time Steps
Ignacio	Constant	X		15	350
	Constant		X	15	350
	C3.5	X		15	350
	C3.5		X	15	350
	Powell	X		15	350
	Powell		X	15	350
	Donelan	X		15	350
	Donelan		X	15	350
	Zijlema	X		15	350
	Zijlema		X	15	350
	Hwang	X		15	350
	Hwang		X	15	350
	Garratt	X		15	350
	Garratt		X	7.5	700
Irma	Constant	X		15	350
	Constant		X	15	350
	C3.5	X		15	350
	C3.5		X	7.5	700
	Powell	X		15	350
	Powell		X	15	350
	Donelan	X		15	350
	Donelan		X	7.5	700
	Zijlema	X		15	350
	Zijlema		X	15	350
	Hwang	X		15	350
	Hwang		X	15	350
	Garratt	X		7.5	700
	Garratt		X	5	1050
Florence	Constant	X		15	350
	Constant		X	15	350
	C3.5	X		15	350
	C3.5		X	15	350
	Powell	X		15	350
	Powell		X	15	350
	Donelan	X		15	350
	Donelan		X	15	350
	Zijlema	X		15	350
	Zijlema		X	15	350
	Hwang	X		15	350
	Hwang		X	15	350
	Garratt	X		5	1050
	Garratt		X	5	1050

Storm	Drag Coefficient	Wind Only	Wind & Spray	Time Step	Number of Time Steps
Michael	Constant	X		15	350
	Constant		X	15	350
	C3.5	X		15	350
	C3.5		X	15	350
	Powell	X		15	350
	Powell		X	15	350
	Donelan	X		15	350
	Donelan		X	15	350
	Zijlema	X		15	350
	Zijlema		X	15	350
	Hwang	X		15	350
	Hwang		X	15	350
	Garratt	X		7.5	700
	Garratt		X	7.5	700

Table 4.3: Summary of PWP model runs, partitioned by storm, drag coefficient and stress forcing. A time step of 7.5 and 5 minutes, with a corresponding number of time steps of 700 and 1050, are respectively highlighted in yellow and red.

time step had to be altered in order to allow the model to remain stable due to the Courant-Friedrichs-Lewy (CFL) condition, which mathematically is given by

$$C = \frac{u\Delta t}{\Delta x} \leq C_{max}, \qquad (4.1e)$$

where C is the Courant number, u is the magnitude of the velocity, Δt is the time step and Δx is the grid size [46]. This non-dimensional number compares the speed (u) with which information can be passed to the length (Δx) with which it is to be delivered, in each time step (Δt) [46]. As a general rule, it is ideal to try to keep the CFL parameter small (less than one), but not so small that it becomes computationally expensive or contains poor resolution, as would respectively be the case if Δt was reduced or Δx was increased. While C_{max} was never explicitly computed in this study, the violation of the CFL condition was discovered through trial and error, and the resulting model destabilization generally occurred under the strongest forcing. In such cases, to mitigate this issue by lowering the CFL parameter without sacrificing resolution, Δt was reduced by half ($\Delta t = 7.5$ mins) or two-thirds ($\Delta t = 5$ mins), as needed, under extreme forcing. Table 4.3 provides a summary of the model runs including the specific time step required based on the CFL condition, where it was clear the strongest forcing combinations (e.g. Garratt with wind and spray in HU Irma) required the most modification due to the CFL condition. With that said,

while HU Florence was much weaker than HU Irma (at CPA), Garratt's wind only stress parameterization, for example, demanded a shorter time step in the former, less intense storm. This simple example indicates meeting the CFL condition was not an exact science herein and likely is a function of far more variables than simply the strength of the TC and stress forcing (e.g. translation speed, latitude, initial oceanic profiles, etc.) In the end, as alluded to above, these required modifications were computationally expensive as model completion was 2-3 times longer, but in the end result permitted an "apples-to-apples" comparison of equal resolution output.

With all of the model runs complete, the ensuing step involved aligning the positions of the floats/glider with the correct grid points as well as the measured vs. modeled times, to allow for data analysis. Beginning with the grid points, given the model design with a right to left tracking storm and CPA position of (0,0), many of the grid points for the measurement devices were found along or near the y-axis, with positive and negative values indicating right and left of track respectively. As described in Section 4.1.1.1, the CPA distance for the single-sensor storms was simply the range between the float/glider and the storm's track at the time of CPA. As a result, since the shortest distance between these locations is a line, perpendicular to the storm's track, the grid points for these two devices were simply the lengths left or right of track, divided by 5 km, with each falling on the x-axis. For example, Navy glider 288's CPA to HU Michael was 50 km to the right of its track, therefore the grid point was (0,10). In the two storms where an array of floats was deployed, the grid point of each float was determined with respect to the CPA position in the following way. First, two lines were plotted from the float position, one directly to the CPA position and another perpendicular to the storm's track, forming a right triangle. The hypotenuse of this triangle is the distance from the float to the CPA position, but in order to fix the grid points to account for the rotation of the storm's translation bearing to that along the x-axis (270°), the perpendicular leg is the distance left or right of track and the along-track leg is the horizontal distance ahead or behind the CPA position. As listed in Table 4.2, due to the relatively short duration between float deployment and storm CPA in HUs Irma and Florence, the floats were not appreciably advected horizontally with respect to their deployment position, minimizing the x-component of their grid points.

With the model grid positions of the measurement devices in place, the final phase to be completed before conducting data analysis was aligning model and CPA times. This was

accomplished using the translation speed of each storm, taken to be constant and that of the storm at CPA, by determining how long it would take to travel from its starting position to the origin of the model grid. For example, HU Florence moved west, northwest at 5.5 knots at CPA, so in the model, it took approximately 12.5 hours to travel 250 km to reach the origin. Using these transit times, the measured data interval was selected to include at least such a duration before CPA, extending approximately another 3 days, as summarized in Table 4.2. Overall, this process proved effective, but as a pitfall of the assumption of a constant translation speed, there was some manual adjustment required through data analysis to ensure better alignment. While these editions were fairly small, on the order of a couple hours in extreme cases, error was certainly induced through this simplification.

4.2   Variables for Comparison

Upon the completion of all model runs, data analysis ensued by comparing the PWP outputs with float/glider measurements, for all four storms and six included grid points. As mentioned in Section 1.1, success in accurately modelling TC intensity has been slow relative to that of storm tracks, but recent improvements have been founded using new heat bearing variables. In particular, rather than using the legacy index, a SST of at least 26°C, to indicate oceanic conditions suitable for TC formation and/or maintenance, considering the vertical ocean has proven more successful [5]. Both the depth of the 26°C isotherm as well as the tropical cyclone heat potential, which will be described below, each provide a multi-dimensional characterization of the sufficiently warm ocean water for TC sustenance. Modeling and replicating the measurement of these variables is not only paramount to improving TC intensity forecasts, but can also help to explain the downwelling response of ALAMO 9077 in HU Ignacio. In addition, the relative ocean heat content as well as vertical velocity are two parameters that do not have a direct connection to intensity forecasting, but will more directly characterize the downwelling event. The following sections will discuss these four variables in detail in terms of their computation, derivation and/or relevance to this study with respect to illustrating the downwelling as well as accuracy and trends formed via variable stress forcing (e.g. C_D, $\tau_{w\&s}$, τ_w).

4.2.1 Depth of the 26°C Isotherm

The depth of the 26°C isotherm is a very straightforward variable that was not arbitrarily selected as a relatively warm ocean benchmark, rather directly correlated to TC formation and air-sea heat exchange. Through various studies, it has been illustrated that ocean temperatures below 26°C are not conducive to TC formation, meanwhile, this value is also representative of the average surface temperature of the tropical atmosphere (during each hemisphere's respective storm season), indicating that if the ocean temperature was any cooler, the atmosphere would be unable to garner the necessary energy from the sea for storm development [6]. This depth is simply determined by the vertical distance from the sea surface to the level where the ocean temperature is 26°C. When using float/glider data, while the temperature is measured directly, the oceanic profiles are recorded as function of pressure, which must be converted to depth. To do so, an integration of the hydrostatic equation was conducted, approximated slightly via the use of a fourth order least squares polynomial fitting for pressure, yielding the following

$$z = \frac{c_1 p + c_2 p^2 + c_3 p^3 + c_4 p^4}{g(\phi) + \frac{1}{2}\gamma' p}, \qquad\qquad (4.2a)$$

where z is depth, $g(\phi)$ is gravity as a function of latitude and c_1, c_2, c_3, c_4 and γ' are constants per [47]. The PWP model naturally embeds the hydrostatic approximation and computes the temperature and depth at each vertical (and horizontal) grid point. With each of these depths in place, in order to primarily deduce trends and compare variable forcing and storms under a single model, conducting all analyses using perturbations from the initial measurement/time step was prudent (and was done with most variables and statistical comparisons herein). As such, the depth of the 26°C isotherm perturbation under varying stress was plotted for each float/glider, with Figure 4-3 as an example for HU Irma. As introduced as motivation for this study in Section 1.2.1, a depression in the depth of the 26°C isotherm is a potential indicator of negative vertical motion or downwelling in at least the upper portion of the water column. Since this was first observed in ALAMO 9077's measurement of HU Ignacio and directly contradicts classical theories of the mixed layer response to a passing TC, a two-step analysis using these data was sensible. First, attempt to replicate ALAMO 9077's measurement of a depression of the 26°C isotherm using the modeled output for HU Ignacio and second, compare the other five

measurements and model outputs to determine possible trends. If the model does indicate a similar response, likely varying in magnitude, it would reasonable to conclude downwelling was present, but with further replication to come with the remaining three variables.
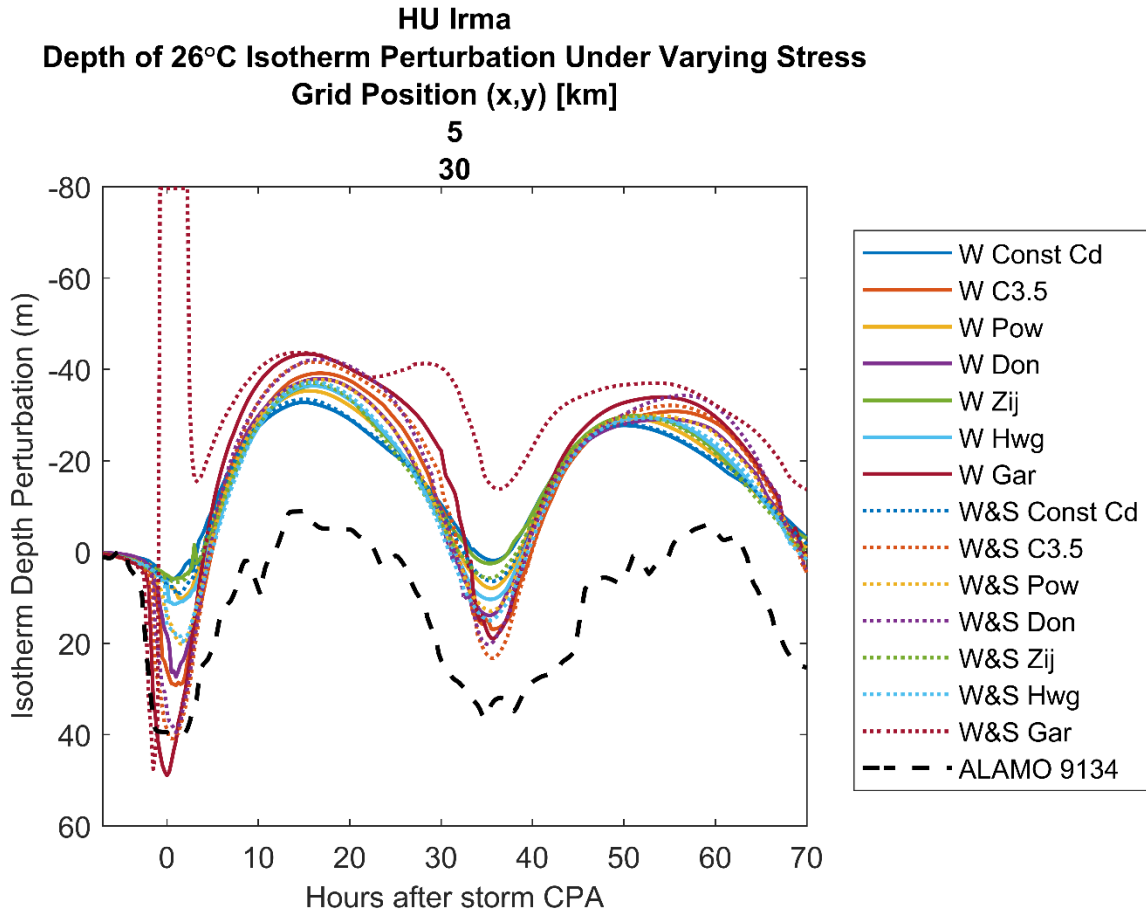
Figure 4-3: Depth of 26°C isotherm perturbation under varying stress, during the passage of HU Irma, as measured by ALAMO 9134 and initialized nine hours prior to its CPA with the storm. Positive perturbation values reflect a depression in the original measured/modeled depth of the 26°C isotherm. Solid and dotted lines represent modeled output with τ_w and $\tau_{w\&s}$ forcing respectively, under a variable C_D. The black dashed line represents measured data.

4.2.2 Tropical Cyclone Heat Potential

Tropical cyclone heat potential (TCHP) dates back to the early 1970s when it was first reasoned that TCs develop and strengthen in part due to a heat flux from the ocean to the atmosphere. As such, it was investigated and confirmed that the larger the heat content or TCHP, the more favorable the conditions for TC formation and sustainment [7], [6]. TCHP characterizes the amount of energy per unit area available to support TC formation, which mathematically, is

defined as the integrated vertical temperature from the depth of the 26°C isotherm to the sea surface [48], as given by

$$TCHP(x,y) = \rho_w c_p \int_{z_{26}}^{0} (T(x,y,z) - 26)dz, \qquad (4.2b)$$

where c_p is the heat capacity of water $\left(c_p = 4186\frac{J}{kgK}\right)$ and z_{26} is the depth of the 26°C isotherm [4], [6], [7]. Inherently, TCHP and the depth of the 26°C isotherm are related and proportional, but the former provides greater insight to the characteristics of the water column, as illustrated in the following example with HU Ignacio. As is the case with all passing TCs, the combination of significant vertical mixing and the entrainment (upwelling) of much cooler waters into the mixed layer, precipitation and entrainment of cool rain and air respectively, to the warmer surface, and cloud cover all play a role in reducing the mixed layer's average temperature and greatly altering its profile. As a short case study, two measured profiles were taken before and after the CPA of HU Ignacio with ALAMO 9077 (16Z 30 Aug 15). The first profile, measured approximately 15 hours before CPA, exhibited a shallow, but uniform mixed layer roughly 55 m deep, with a SST of 27.65°C and depth of the 26°C isotherm of 60.4 m. Just over two days later, well beyond the passage of the storm, the second profile displayed a constantly decreasing temperature, with a SST of 27.57°C and depth of the 26°C isotherm of 60.7 m. These two profiles, which are displayed in Figure 4-4a, not only have nearly identical SSTs, but also depths of the 26°C isotherm, before and after storm passage. By only using those two metrics to assess the favorability for TC formation or sustainment, the result would be the same; however, their TCHPs are much different. Figures 4-4b and 4-4c illustrate the TCHP values by shading in the area of water in which the profile has a temperature greater than 26°C, from the depth of the 26°C isotherm to the surface. In this case, it is clear that there is an increased chance of TC formation or sustainment in the red profile, before storm passage, as would be expected. In this case, however, even the pre-CPA profile was only marginally conducive to TC strengthening, as TCHP values of at least $60\frac{kJ}{cm^2}$ have historically proven to have a significant effect on storm formation and intensification [7]. Nonetheless, the utility of TCHP is illustrated in this example.

   TCHP values in this study were computed using equation (4.2b) for both measured data and

HU Ignacio Temperature Profile Comparison

a)
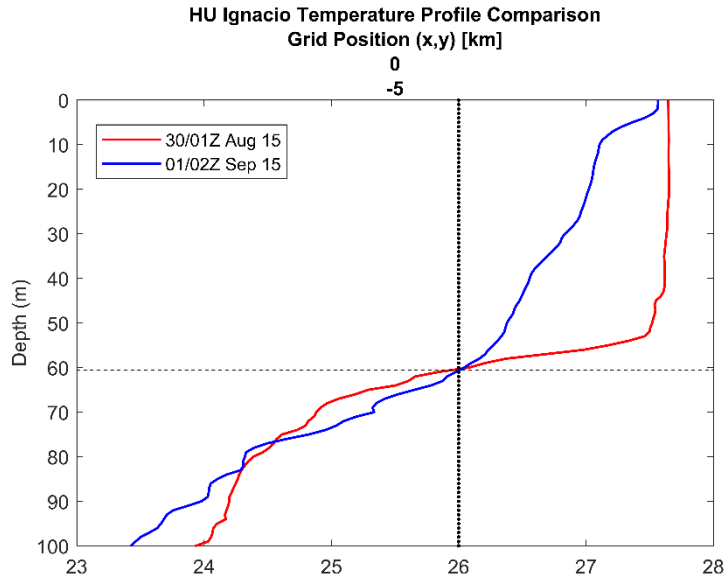
b)
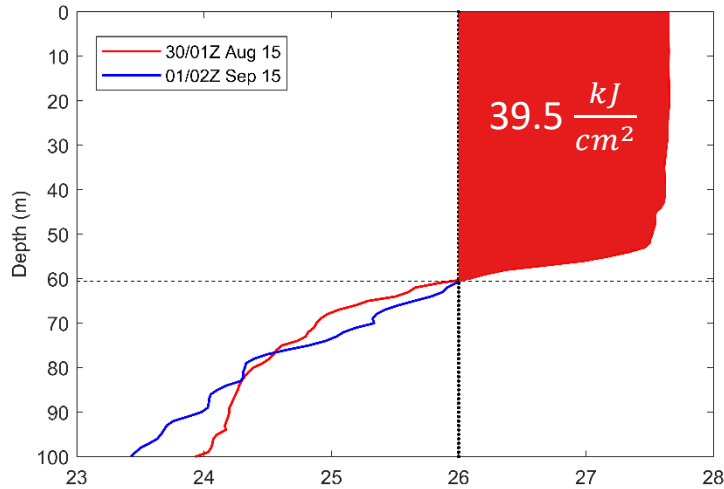
c)
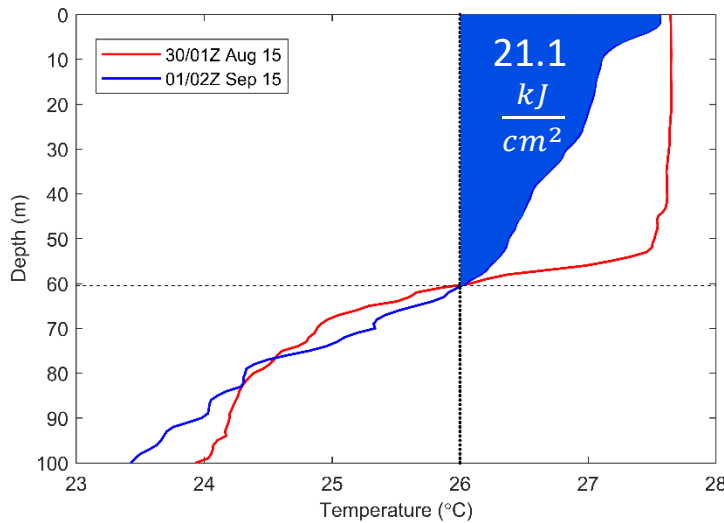
Figures 4-4a, 4-4b, 4-4c: a) HU Ignacio temperature profile comparison of two measures, one before (30/01Z Aug 15 (red)) and after (01/02Z Sep 15 (blue)) CPA with ALAMO 9077. The dashed line identifies the approximate depth of the 26°C isotherm, nearly identical for each profile, while the solid vertical line simply marks 26°C for TCHP visual analysis; b) Shaded in value of TCHP for the pre-CPA profile; and c) Shaded in value of TCHP for the post-CPA profile.

modeled output and as described above with the depth of the 26°C isotherm, these were compared for each of the storms and measurement locations, including that of HU Irma and ALAMO 9129, as displayed in Figure 4-5. In order to discern if downwelling was present ahead of storm passage, there would likely be an increase in the TCHP perturbation, proportional to a deepening in the depth of the 26°C isotherm. With that being said, it can be easily shown visually and proven mathematically that if the average temperature of this layer decreases despite a deepening depth of the 26°C isotherm, the TCHP could remain constant or even decrease. While the meteorological and oceanographic processes required to force such a situation are unlikely to be present in the tropics ahead of a passing TC, it further exemplifies the need to characterize the vertical velocity directly to replicate downwelling, which will be introduced below using the next two variables.

4.2.3 Relative Ocean Heat Content

While the PWP model is able to compute the vertical velocity, as will be discussed in Section 4.2.4 below, the current versions of ALAMO and Navy glider are unable to directly measure this quantity. As a result, there existed no obvious way to compare measured data with modeled output akin to the remainder of the study, in arguably the most important variable in terms of the replication of downwelling. With that being said, a physical argument can be made that changes to the temperature profile of the water column, over relatively short time scales (shorter than diurnal), must be, at least in large part, a function of warmer or cooler water being advected in horizontally, above some reference depth (C. Densmore, personal communication, January 17, 2019). Such a measure of this quantity would be very similar to TCHP, but with one major exception, that reference depth would ideally be much deeper than that of the 26°C isotherm, in order to capture profile changes further down the column. As such, using equation (4.2b) as a basis, the following equation represents the relative ocean heat content (ROHC), as given by

$$ROHC(x,y) = \rho_w c_p \int_{z_{ref}}^{0} \left(T(x,y,z) - T_{ref}\right) dz, \qquad (4.2c)$$

where z_{ref} is the depth of the reference temperature, T_{ref}. To encapsulate as much of the column as possible while ensuring values remained within the measured and modeled domains, a reference temperature of 21.5°C was selected, which amounted to approximately 145 m in the
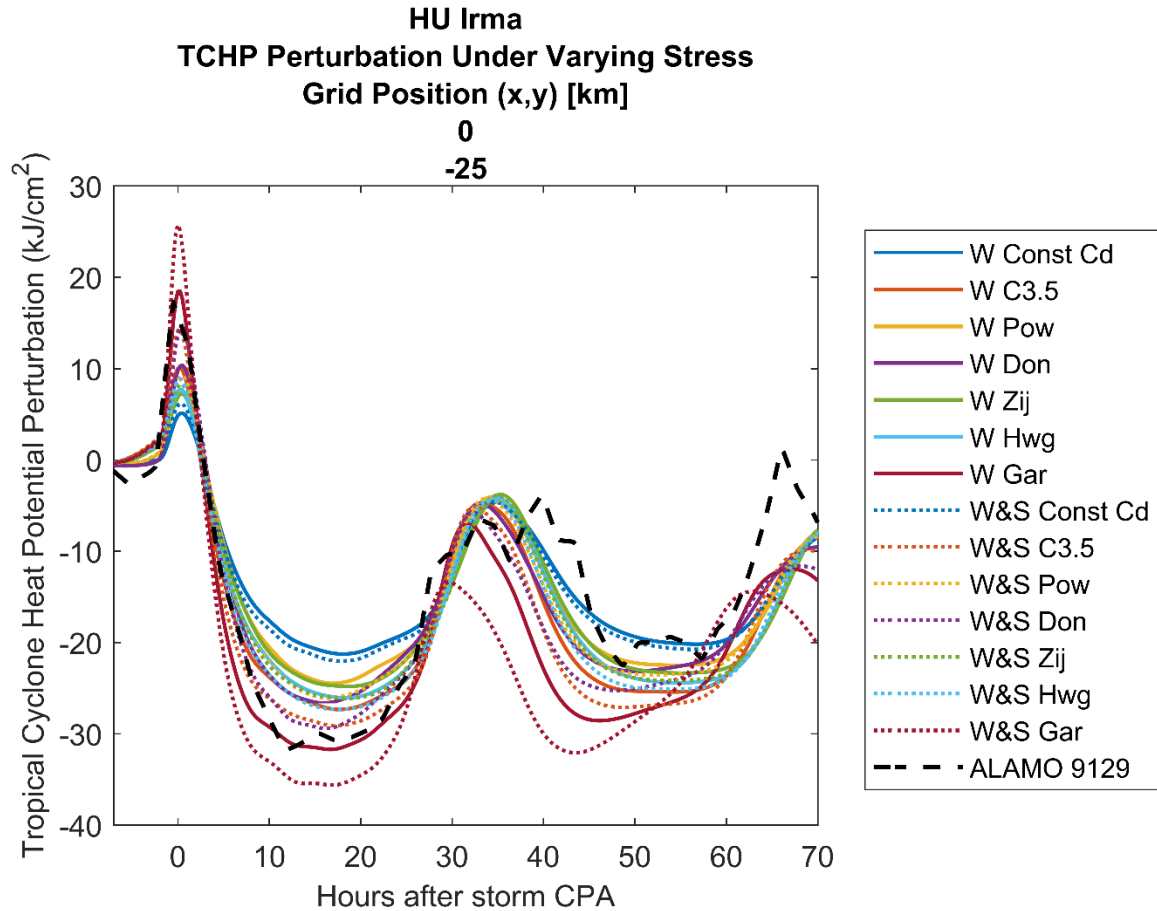
Figure 4-5: TCHP perturbation under varying stress, during the passage of HU Irma, as measured by ALAMO 9129 and initialized nine hours prior to its CPA with the storm. Solid and dotted lines represent modeled output with τ_w and $\tau_{w\&s}$ forcing respectively, under a variable C_D. The black dashed line represents measured data.

case of HU Ignacio for example. A sample of a ROHC perturbation is illustrated in Figure 4-6 below, during the interaction of HU Irma and ALAMO 9134, but this singular quantity, which is expected to take on a very similar shape (yet different magnitude) to that of the TCHP perturbation, will not be analyzed extensively in this study. Overall, ROHC can help illustrate the upper oceanic temperature response beyond that of only the tropical mixed layer via TCHP, acting as a better indicator for a vertical response, but at the same time, having no implications for TC formation and intensification.
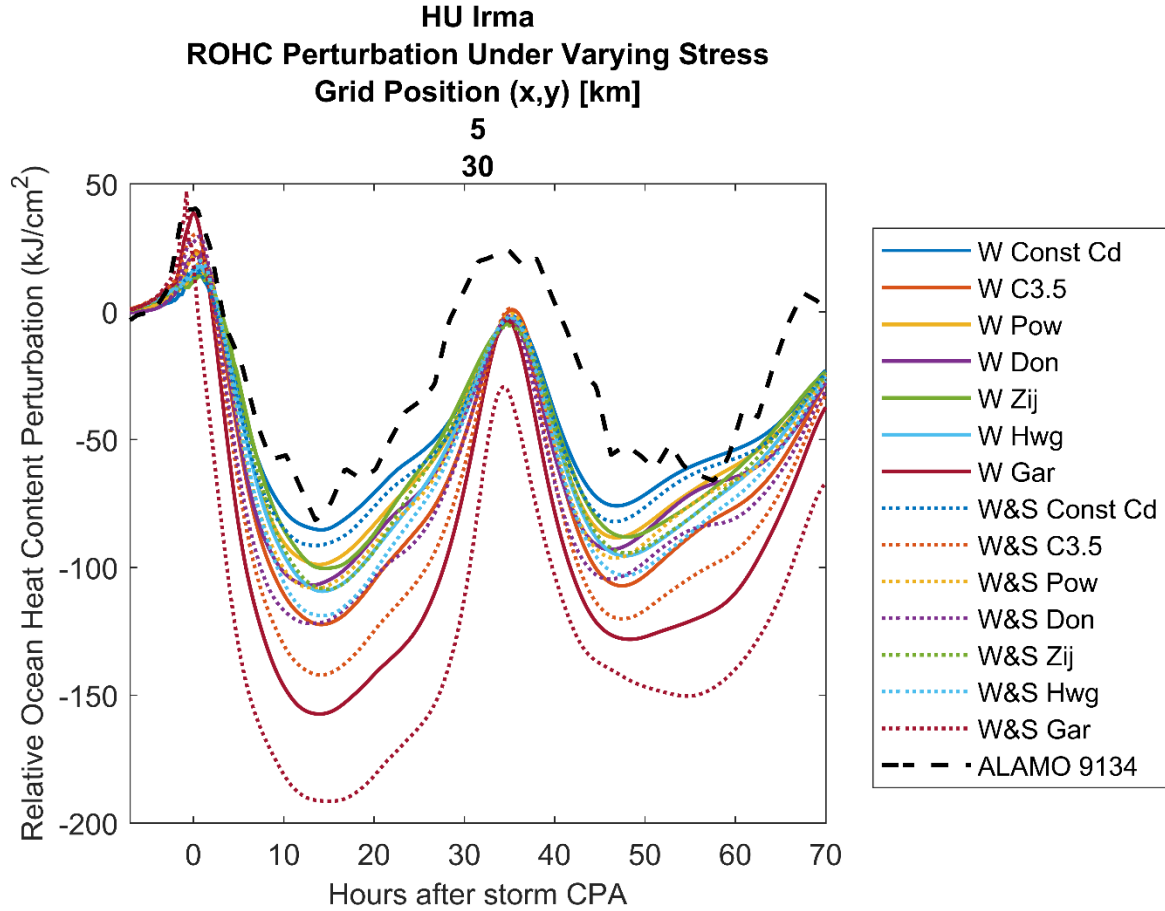
Figure 4-6: ROHC perturbation under varying stress, during the passage of HU Irma, as measured by ALAMO 9134 and initialized nine hours prior to its CPA with the storm. Solid and dotted lines represent modeled output with τ_w and $\tau_{w\&s}$ forcing respectively, under a variable C_D. The black dashed line represents measured data.

4.2.4 Vertical Velocities

While the PWP model, via equation (4.1c) and continuity, computes and carries the vertical velocity, w_{PWP}, ROHC will be used to derive the measured and parameterized vertical velocity, w_{ROHC}. To that end, although computing ROHC is very straightforward following the establishment of a reference temperature, relating this to a vertical velocity is not as trivial. Such a parameterization can be achieved, however, by using the aforementioned argument relating the horizontal advection into the water column over time. First, assume any change in ROHC over time is equal to the difference between the final and initial values, as given by

$$\Delta ROHC = ROHC_f - ROHC_0. \tag{4.2d}$$

68
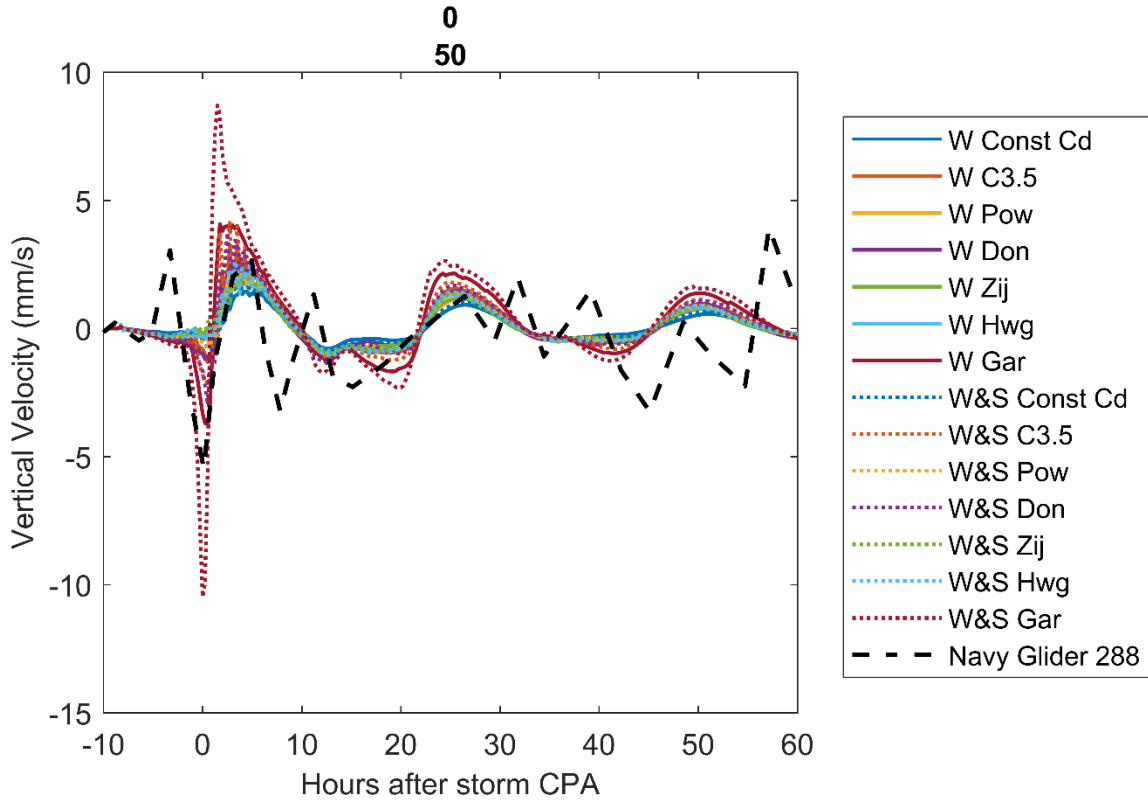
Figure 4-7: Modeled and ROHC-derived vertical velocity under varying stress, during the passage of HU Michael, as measured by Navy glider 288 and initialized ten hours prior to its CPA with the storm. Solid and dotted lines represent model output, w_{PWP}, with τ_w and $\tau_{w\&s}$ forcing respectively, under a variable C_D. The black dashed line represents w_{ROHC}, derived from measured data.

Next, attempt to parameterize the effect of horizontal advection over time on ROHC through the following relationship, as given by

$$\Delta ROHC = (\nabla_H \cdot \boldsymbol{u})(ROHC_0)\Delta t, \qquad (4.2e)$$

where $\nabla_H \cdot \boldsymbol{u}$ is the horizontal divergence of velocity. Assuming continuity and a rigid lid, equation (4.2e) can be discretized into the following form

$$\Delta ROHC = \left(\frac{w_{ref}}{z_{ref}}\right)(ROHC_0)\Delta t. \qquad (4.2f)$$

Finally, by combining equations (4.2d) and (4.2f), the following critical relationship is achieved, as given by

$$w_{ref} = w_{ROHC} = \frac{z_{ref}}{\Delta t}\left(\frac{ROHC_0 - ROHC_f}{ROHC_0}\right) \qquad (4.2g)$$

where z_{ref} is defined as a negative value. Using both w_{PWP} and w_{ROHC}, a plot of modeled output and measured data respectively, can be used to discern the presence and sequence of downwelling and upwelling, as evidenced in Figure 4-7—the interaction of HU Michael and Navy glider 288. In particular, the replication of downwelling must begin with an initial oceanic response containing a negative vertical velocity, likely to be the minimum (or most negative) value over the time domain. While the depth of the 26°C isotherm, TCHP and ROHC can lead one to an affirmative or negative conclusion with respect to downwelling, the vertical velocities will help to most clearly point to a definitive conclusion.

4.3   Comparison of Measured and Modeled Results

With the all four variables established, three themes can be addressed by comparing the measured data and modeled output, including downwelling, drag coefficients, and overall forcing. In doing so, there will be a mix of qualitative observations and statistical analyses presented over the following three sections.

4.3.1   Downwelling Trends - Four Variable Comparison

The presence of downwelling as the initial upper oceanic response to TC passage was assessed qualitatively through the examination of each of the four variables, at all included storm and position combinations, for both measured data and modeled output. First, as mentioned in Section 4.2.1, a two-level analysis is prudent, first beginning with the modeled output at the position of this study's motivation—HU Ignacio's interaction with ALAMO 9077, as displayed in Figure 4-8. As described earlier via Figure 1-2, the measured perturbation of the 26°C isotherm indicated a depression of 40.0 m, clearly beginning ahead of and minimizing

immediately after storm CPA. Shifting to the modeled output, in each of the 14 forcing types, the first response was also clear depression of this variable, beginning and ending slightly closer to the time of CPA[9]. To help quantify presence of downwelling, a comparison between the pre-CPA minimum and post-CPA maximum was conducted, where the downwelling index (DWI) was met (or "positive") when the former had a magnitude of at least 25% of the latter, for all four variables. While this value was selected arbitrarily, as this pre-CPA response challenges traditional oceanic theories in regards to TC passage, it is believed that a quantified response of a fourth or more of the expected post-CPA measure is significant. Using the measured metrics as
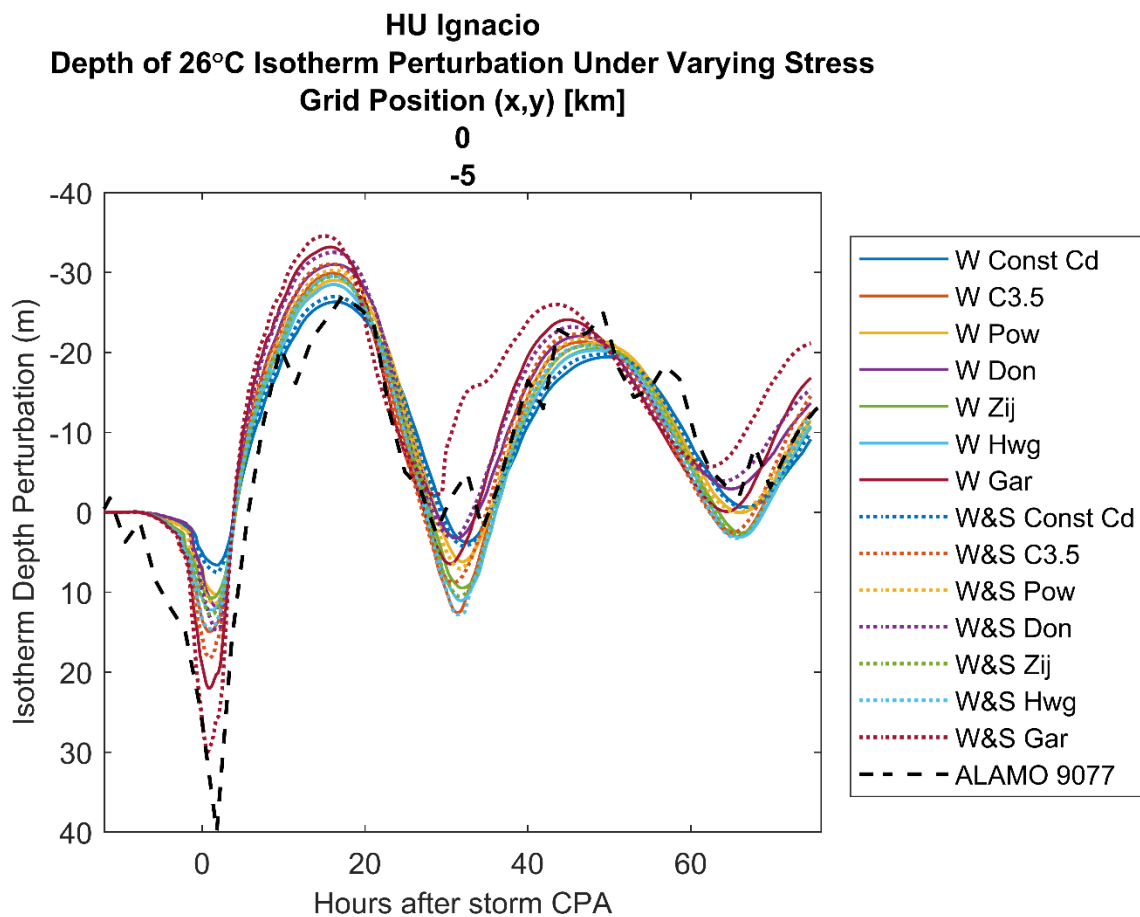
Figure 4-8: Depth of 26°C isotherm perturbation under varying stress, during the passage of HU Ignacio, as measured by ALAMO 9077 and initialized 12 hours prior to its CPA with the storm. Positive perturbation values reflect a depression in the original measured/modeled depth of the 26°C isotherm. Solid and dotted lines represent modeled output with τ_w and $\tau_{w\&s}$ forcing respectively, under a variable C_D. The black dashed line represents measured data.

---

[9] The variability and magnitude of the modeled output vs. measured data as well as a post-CPA upper oceanic response will be discussed in detail in Section 4.3.2.

an example, with a post-CPA maximum perturbation of -27 m, the resulting DWI was 148.1%, well over the established 25% to be considered as downwelling. This same process was then applied to the modeled output where 13 of the 14 different forcing types also indicated a positive DWI. As a result, with 93.3% positive DWI test, the measured depression in the depth of the 26°C isotherm was replicated for HU Ignacio.
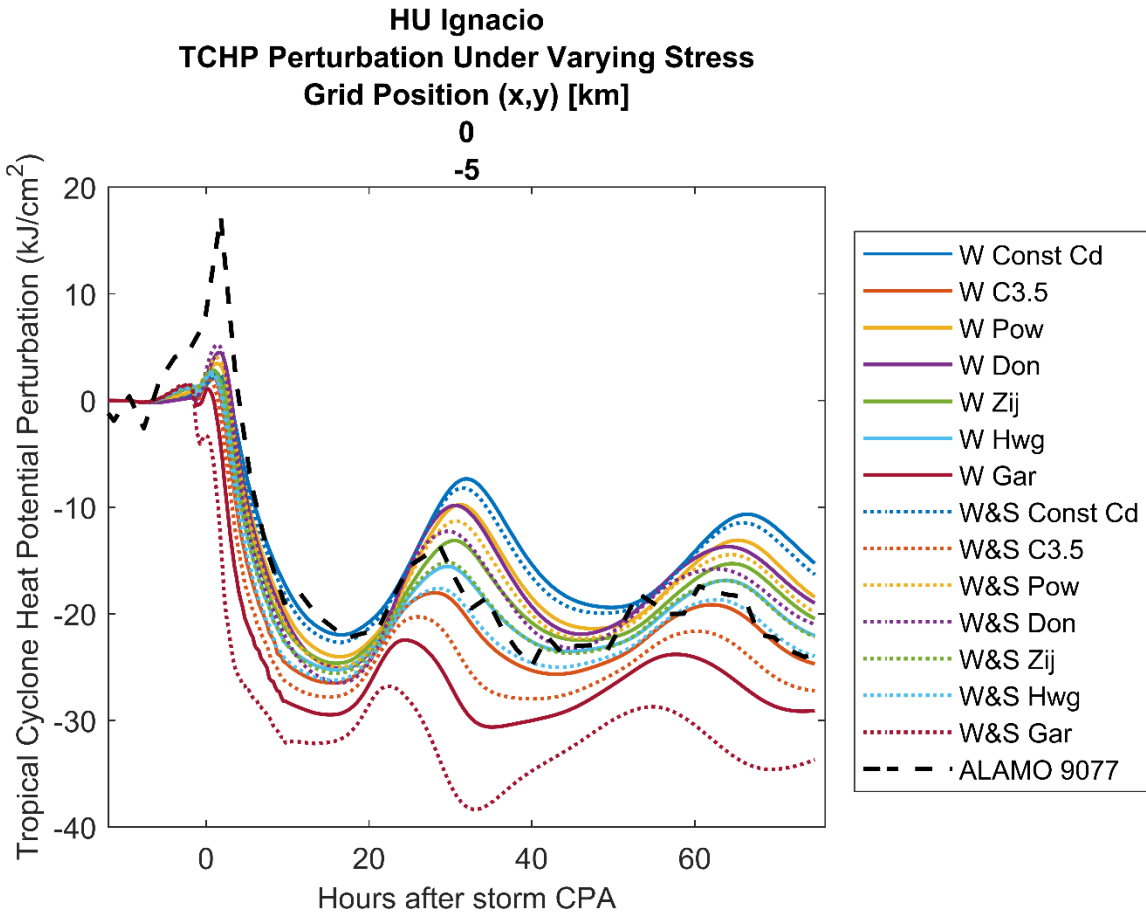
Figure 4-9: TCHP perturbation under varying stress, during the passage of HU Ignacio, as measured by ALAMO 9077 and initialized 12 hours prior to its CPA with the storm. Solid and dotted lines represent modeled output with τ_w and $\tau_{w\&s}$ forcing respectively, under a variable C_D. The black dashed line represents measured data.

Subsequently, continuing to use HU Ignacio as the example, a similar analysis was conducted for TCHP perturbation, using Figure 4-9. At least partially as a result of the magnitude of the depth of the 26°C isotherm perturbation not having been achieved by any of the modeled forcing types, the measured TCHP perturbation was much greater. In addition, with the perturbation being positive, it was considered as having a positive DWI. With said, however, none of the

modeled output registered a positive DWI. The same process was conducted with nearly identical results using the ROHC perturbation, where only five modeled outputs and the measured results were considered as having a positive DWI.
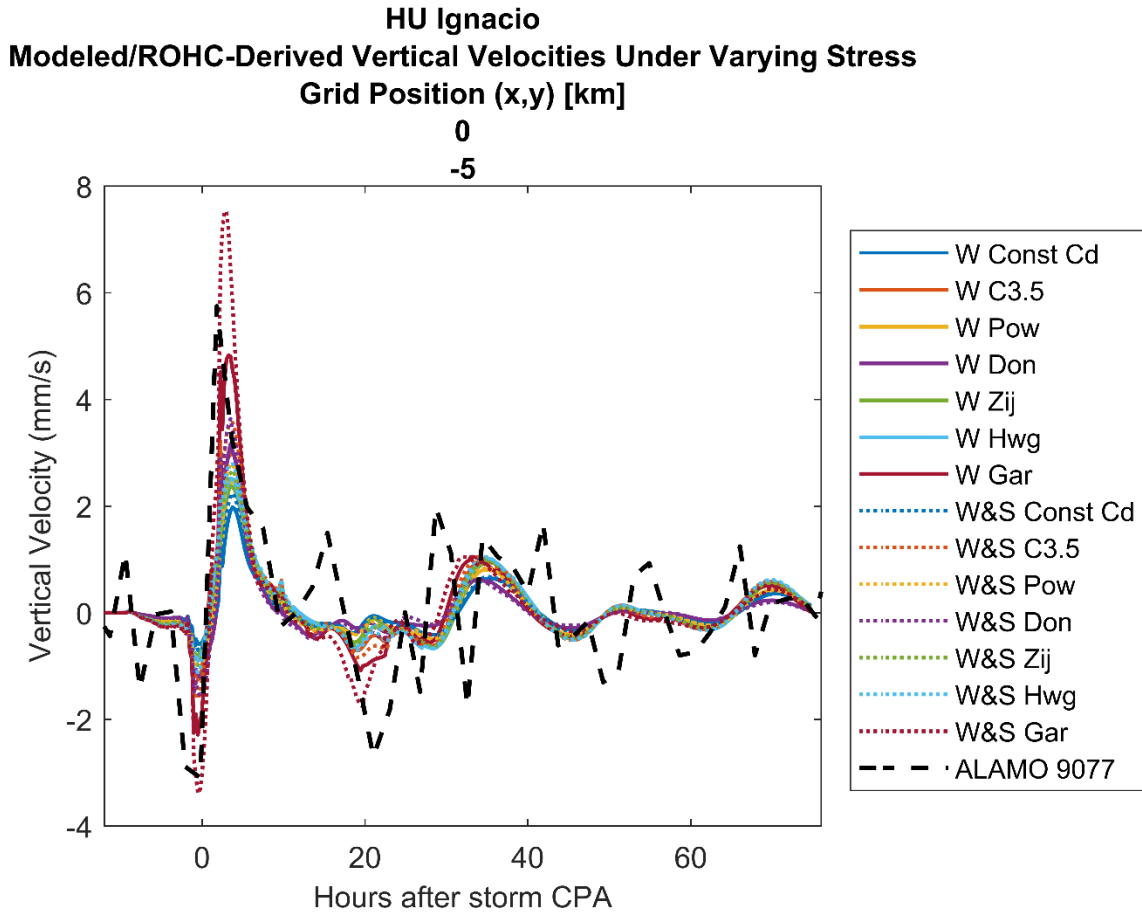
Figure 4-10: Modeled and ROHC-derived vertical velocity under varying stress, during the passage of HU Ignacio, as measured by ALAMO 9077 and initialized 12 hours prior to its CPA with the storm. Solid and dotted lines represent model output, w_{PWP}, with τ_w and $\tau_{w\&s}$ forcing respectively, under a variable C_D. The black dashed line represents w_{ROHC}, derived from measured data.

With mixed results to that point, the most telling metric remained—vertical velocity. If downwelling is present prior to CPA, the vertical velocity must be negative; in this study, however, it must have a strength at least ¼ of the well-known, traditionally primary, strong upwelling associated with TC passage [14], allowing it achieve a positive DWI. The plot of w_{PWP} and w_{ROHC} during the passage of HU Ignacio is illustrated in Figure 4-10, where there is a clear, pre-CPA, negative vertical velocity in both the modeled output and measured data, followed by the expected upwelling. In this case, the pre- and post-CPA extrema of w_{ROHC}

measured -3.1 and 5.7 mm/s respectively, leading to a 54.4% comparison and positive DWI. Furthermore, when including the w_{PWP} metrics as well, the vertical velocities in total resulted in a 80.0% positive DWI test.
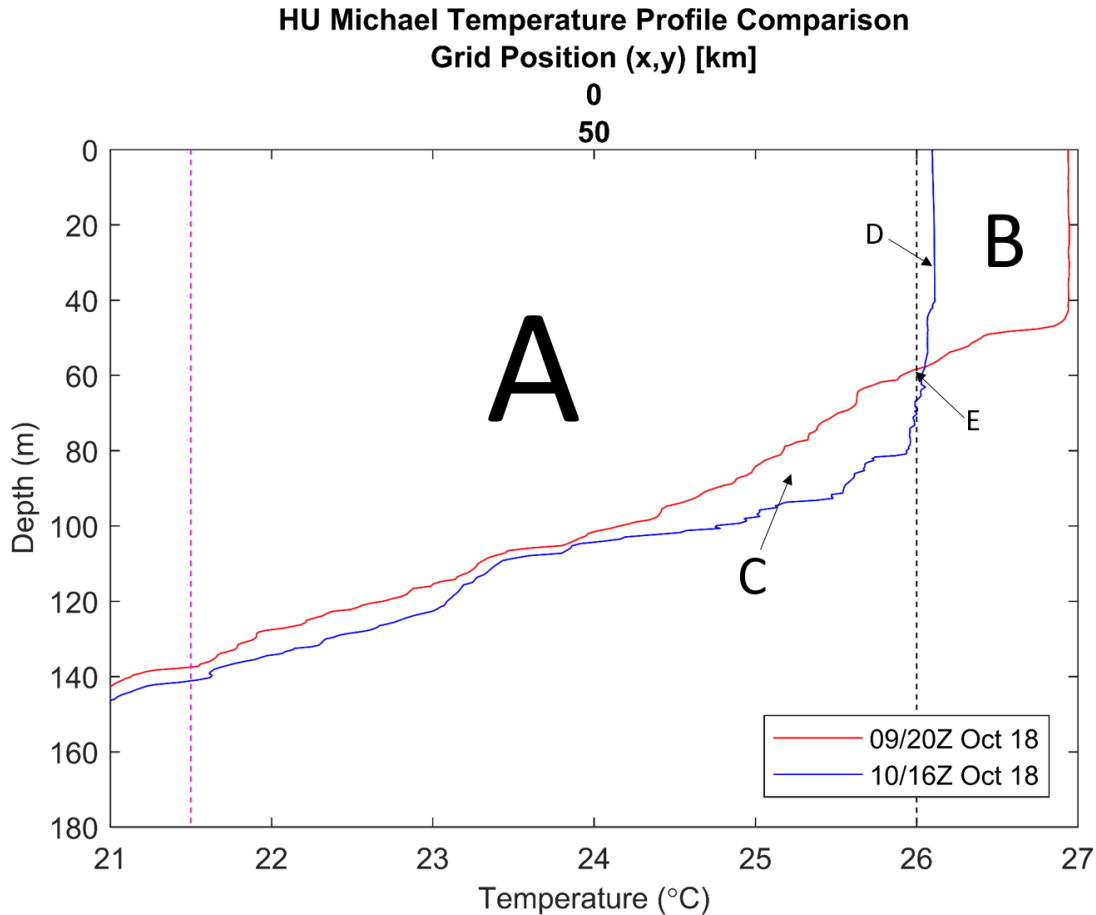
Figure 4-11: HU Michael temperature profile comparison of two measures, one before (09/20Z Oct 18 (red)) and after (10/16Z Oct 18 (blue)) CPA with Navy glider 288. The dashed vertical lines mark 26°C for TCHP (black) and 21.5°C for ROHC (magenta) for visual analysis. The different letters identify bounded areas, where $A \gg B > C \gg D \gg E$ and $\Delta TCHP = E - B$ and $\Delta ROHC = (C + E) - B$. Area B is larger, but of similar order as area C, resulting in the magnitude of $\Delta TCHP \gg \Delta ROHC$.

Overall, two of the four variables resoundingly indicated pre-CPA downwelling during the interaction of HU Ignacio and ALAMO 9077, but only cumulated 55% positive DWI tests. With that said, this same process was then continued at every location and storm herein, as summarized in Table 4.4. These analyses indicated the presence of downwelling unequivocally based on tests with the depth of the 26°C isotherm perturbation and vertical velocities, mixed, trendless results with ROHC perturbation, and overwhelmingly no downwelling based on TCHP

Summary of Downwelling Analysis						
		Modeled output & Measured Data Meeting Downwelling Index per Storm				
Storm	*Float / Glider*	*Depth of 26°C Isotherm Pert*	*TCHP Pert*	*ROHC Pert*	*Vertical Velocity*	*Average + DWI per storm (no TCHP)*
Ignacio	9077	93.3%	6.7%	40%	80.0%	*71.1%*
Irma	9129	100%	86.7%	86.7%	100%	*95.6%*
	9134	80.0%	0.0%	20.0%	100%	*66.7%*
Florence	9136	100%	0.0%	20.0%	100%	*73.3%*
	9141	100%	0.0%	100%	100%	*100%*
Michael	NG 288	100%	0.0%	40.0%	100%	*77.8%*
Average + DWI per variable		*94.4%*	*~~15.6%~~*	*51.1%*	*96.7%*	***80.7%***

Table 4.4: Summary of downwelling analysis where the percentage of the primary variables represent the number of positive DWI outcomes compared to the modeled output and measured data (15 comparisons at each point). The italicized percentages represent the average number of positive DWI tests per variable (bottom row), storm and measurement platform (rightmost column—neglecting TCHP) and overall percentage (bottom right—neglecting TCHP).

perturbation results. In fact, with such low DWI test results (15.6%, with four of the storms indicating 0.0% positive outcomes), further analysis was required to discern a potential cause and assess the utility of TCHP perturbation.

To begin, it was prudent to consider the primary difference between TCHP and ROHC perturbations, where the latter feeds w_{ROHC}, due to the great differences in the DWI test results. As described in 4.2, they are computed using the exact same method, but contain distinct reference temperatures—26 and 21.5°C respectively, where such implications can be illustrated through an example in Figure 4-11, using pre- and post-CPA temperature profiles from HU Michael. When comparing the two profiles, that before CPA had a much warmer, but shallower mixed layer and steep thermocline indicative of a notional tropical contour, which substantially cooled, deepened and contained a more gradual upper thermocline after storm passage due to intense mixing and cool entrainment. Using these observations, a comparison of the magnitudes of ΔTCHP and ΔROHC helped to codify the DWI test discrepancies. Due to the cutoff at 26°C, |ΔTCHP| was much larger than |ΔROHC| as only a sliver of the increased mixed layer depth and none of the weakly sloping upper thermocline (a combination of areas 'C' and 'E' in Figure (4-11)) were captured by the former measure. As a result, these regions of relatively warm water, as compared to their initial measures at a given depth, were not quantified in TCHP

computations leading to |ΔTCHP| being 2.65x greater than |ΔROHC| on average. With such a large measure in |ΔTCHP|, regardless of a slight increase due to downwelling ahead the storm passage, the post-CPA perturbation will always be orders of magnitude larger, ultimately consistently resulting in a negative DWI test. Rather than adjusting the DWI for TCHP perturbation alone, it is believed this variable does not provide insight towards vertical motion, which is still captured via the ROHC perturbation. As a result, with this parameter neglected, 80.7% of modeled output and measured data resulted in positive DWI tests, strongly pointing to the presence of downwelling ahead of CPA in each storm and at all measurement locations.

4.3.2   Oceanic Response Trends, Plausible Drag Coefficients, and Effect of Sea Spray

In order to assess which drag coefficients were reasonable, the effect of sea spray and eventually which forcing was most accurate, an evaluation of oceanic response trends to TC passage was sensible. The following paragraphs will continue the use HU Ignacio's interaction with ALAMO 9077 as the case study, but subsequently expound upon all storms to provide study-wide trends, comparing modeled output, with variable forcing, to measured data.

4.3.2.1 Oceanic Response Trends in the Depth of the 26°C Isotherm

Beginning with the perturbation of the depth of the 26°C isotherm, as illustrated in Figure 4-8, and working in chronological order, the first set observations involves its marked depression, commencing prior to and maximizing near CPA. This interval, which will now be referred to as the downwelling region, boasted a 40 m perturbation as measured by ALAMO 9077, which was at least twice deep as 92.8% of modeled output. While none of the variable forcing matched the measured data in this region, key trends emerged as first, the depth of the maximum depression was proportional to the strength of forcing. As illustrated by the combination of Figures 2-1 and 3-1, the strongest stress forcing was achieved by grouping sea spray with the drag coefficients of Garratt, C3.5, and Donelan. In the downwelling region of HU Ignacio, the maximum depressions, in descending order, were realized by $\tau_{w\&s\_Gar}$, τ_{w_Gar}, $\tau_{w\&s\_C3.5}$, $\tau_{w\_C3.5}$, $\tau_{w\&s\_Don}$. In fact, $\tau_{w\&s\_Gar}$ was far and away the closest model output to, but still approximately 10 m shy of, the measured data. In addition, for every C_D, the maximum depression was larger with $\tau_{w\&s}$

versus τ_w. Overall, the highest valued C_D coupled with spray stress led to deepest perturbation of the depth of the 26°C isotherm.

Following CPA, positive wind stress curl leads to the traditional oceanic response of strong inertial pumping or upwelling, typically with the greatest magnitude throughout the storm passage, which significantly cools the mixed layer due to the entrainment of thermocline water [39]. In this example with HU Ignacio, it what will now be referred to as the upwelling region, both modeled output and measured data indicated this cooling through a maximum shallowing in perturbation of the depth of the 26°C isotherm about 15 hours after CPA. In this case, the amplitude of the measured data was actually less than that from the downwelling region, which was unexpected, especially given traditional theories [14] and the previously undiscovered downwelling response. Furthermore, the modeled output universally exceeded the shallowing of the measured data in this region, with again the strongest forcing exhibiting the greatest values.

Following the initial upwelling, despite a storm's eye having transited nominally between 75-150 km from the CPA location, the presence of inertial currents (rather than directly-forced surface currents) continues to drive vertical mixing for several days [39], as discussed in Section 4.1.2.1. As such, this internal wave signature can be replicated by assessing the post-initial upwelling, specifically looking for alternating, decaying depression and shallowing of the perturbation depth of the 26°C isotherm, with an appropriate inertial period, as a function of latitude. Each of the aforementioned features were found in the upper oceanic response to HU Ignacio, with very good agreement in terms of magnitude and frequency, where the inertial period of the modeled output, measured data and theoretical computation $\left(T_i = \frac{2\pi}{f}\right)$ matched at approximately 38 hours. Overall, PWP output closely matched the measured data for HU Ignacio, especially in this internal wave region, for the perturbation depth of the 26°C isotherm.

While in HU Ignacio the various forcing parameters were unable to meet the magnitude of these connected responses, that was not the case in the other storms. In those HUs, measured data often fell between the strongest and weakest forcing; however, it was made clear that Garratt's C_{DN} parameterization was too strong, sometimes resulting in an upwelling response beyond that of the surface. In HU Florence, for example, as illustrated in Figure 4-12, $\tau_{w\&s\_Gar}$ and τ_{w_Gar} indicated a loosely similar vertical oscillation shape as measured by ALAMO 9144, but the scales of the shallowing perturbation amplitude were more than 5 orders of magnitude

too large. Furthermore, with an initialized depth of the 26°C isotherm of 52 m, under Garratt's forcing, the modeled shallowing perturbation attempted to extend well beyond 50 m, ultimately through the surface of the water, which is the explanation for the visible "cap" in its upwelling region. Following the upwelling response, the storms' well- known internal waves at an inertial frequency were generally well modeled, with some discrepancies in amplitude across the storms.

   In total, the perturbation depth of the 26°C isotherm was aptly modeled and replicated the measured results. Additionally, stronger forcing led to larger extrema and while Garratt's C_{DN} parameterization may be too large, at least visually, there were no clear indications of the most accurate forcing parameterization.

HU Florence
Depth of 26°C Isotherm Perturbation Under Varying Stress
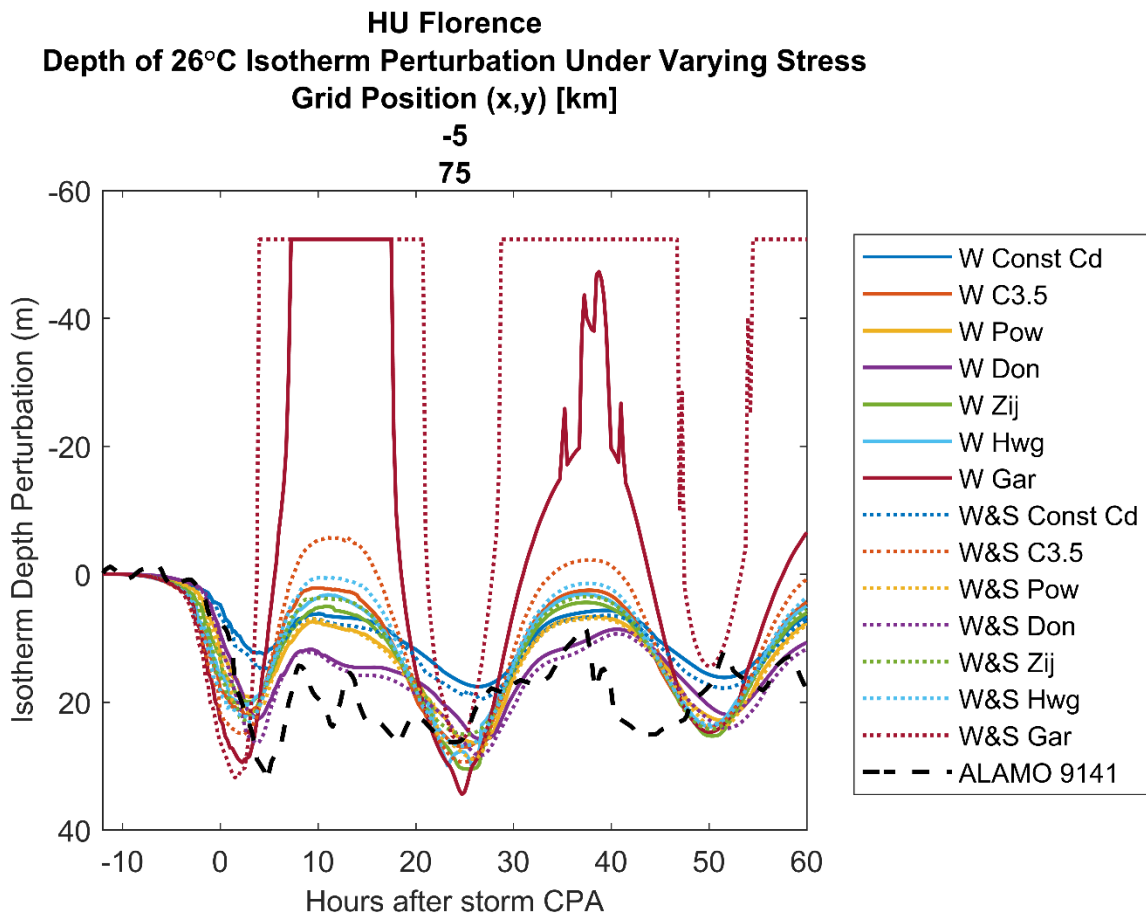
Figure 4-12: Depth of 26°C isotherm perturbation under varying stress, during the passage of HU Florence, as measured by ALAMO 9141, and initialized 12 hours prior to its CPA with the storm. Positive perturbation values reflect a depression in the original measured/modeled depth of the 26°C isotherm. Solid and dotted lines represent modeled output with τ_w and $\tau_{w\&s}$ forcing respectively, under a variable C_D. The black dashed line represents measured data.

4.3.2.2 Oceanic Response Trends in TCHP

In the downwelling region, due to the horizontal advection of warmer water to the column and depression of the 26°C isotherm, the TCHP perturbation is expected to increase as there is more energy per unit area available to promote storm formulation and sustainment. While it is not a precise, one-to-one relationship, the depth of the 26°C isotherm is generally proportional to TCHP, as discussed in Section 4.2.2. With that said, due to the extreme depression of the former in HU Ignacio, the resulting measured increase in the TCHP perturbation was much larger than any of the modeled outputs, as displayed in Figure 4-9. For the measured data, this maximum occurred just after CPA and exactly aligned with that of the perturbation of the 26°C isotherm; however, the modeled output did not react in such a uniform way. First, the largest TCHP perturbation was not exhibited by strongest forcing, rather $\tau_{w\&s\_Don}$, τ_{w_Don}, $\tau_{w\&s\_Pow}$, τ_{w_Pow} and $\tau_{w\&s\_Zij}$, in descending order. In fact, the strongest forcing only demonstrated a small increase and then rapidly decreased near CPA. Second, the addition of spray to the wind stress did not have a consistent response as compared to the wind only forcing. For example, while $\tau_{w\&s\_Gar}$ had the smallest increase in TCHP, it was $\tau_{w\&s\_Don}$ contained the largest, leaving τ_{w_Don} and τ_{w_Gar} in the middle.

Due primarily to the significant mixing and entrainment of cold thermocline waters, the upper portion of the water column significantly cools in the upwelling region. As a result, the TCHP perturbation is expected to significantly decrease to its minimum near the height of the upwelling. In HU Ignacio, order seemed to be restored in this region as there was good agreement in the timing and amplitude of the TCHP minimum, which aligned with the maximum shallowing in the perturbation depth of the 26°C isotherm. In addition, in every forcing parameterization, wind stress with sea spray led to a greater decrease in TCHP than wind only, which was also expected. With that being said, however, nearly all of the modeled output overestimated this depression in TCHP, with the strongest forcing missing by over $10 \frac{kJ}{cm^2}$.

In the ocean's internal wave response region, the oscillating vertical motion causes the 26°C isotherm to be displaced up and down at an inertial period. Unlike its perturbation where it may return or even surpass its original depth, the TCHP perturbation will not even approach its initial values due to the substantial cooling of the mixed layer. As such, its profile is expected to oscillate on a near-inertial period, but with a relatively small, decaying amplitude, remaining

79

negative throughout the interval applicable to this study. In HU Ignacio, these expectations were met and while the general shapes and frequencies aligned, the amplitude of the measured data fell in the middle of the modeled output. Additionally, while no one forcing parameterization was better than the rest, Garratt's C_{DN} led to consistent extremely low TCHP perturbation values as compared to the measured data. In total, the modeled output effectively matched the shape and frequency of the measured response throughout the entire interval, but the strongest forcing was inaccurate during downwelling and $\tau_{w\&s\_Gar}$ and τ_{w_Gar} remained extreme in the subsequent regions.

When expanding to all of the storms and locations, with the exception of the downwelling region, the remainder of these same findings remained trends throughout the dataset. As evidenced in HU Irma's interaction with ALAMO 9129, as illustrated in Figure 4-5, the strongest forcing not only generated the greatest TCHP perturbations (which had been expected, yet was absent in HU Ignacio), but it was τ_{w_Gar} that appeared to have most effectively modeled the downwelling region. Overall, again the modeled output replicated the measured data, with no one forcing parameterization having distinguished itself as the most precise and questions remaining on the validity of Garratt's legacy drag coefficient, which may be better in the downwelling region where surface stress is at a maximum.

4.3.2.3 Oceanic Response Trends in Vertical Velocities

Traditionally, the expected upper oceanic response from a passing storm contains a series of alternating extrema of positive and negative vertical velocity, unequivocally beginning with the former—intense upwelling at CPA [14]. In Section 4.3.1, however, the presence of downwelling as the initial vertical response was established for each storm in this study, ultimately modifying the expected result to begin with a negative vertical velocity. In HU Ignacio, just prior to CPA, there was a marked spike in negative vertical velocity, indicative of the anticipated downwelling in this region, as pictured in Figure 4-10. This signature was also found in all of the modeled output, with the strongest forcing exhibiting the greatest magnitude vertical velocities, led by $\tau_{w\&s\_Gar}$ and τ_{w_Gar}. As with the perturbation of the depth of the 26°C isotherm, the $\tau_{w\&s\_Gar}$ and τ_{w_Gar} provided the results closest to the magnitude of the measured data in this region. In addition and as before, wind stress with sea spray universally increased the magnitude of the downwelling velocity.

In the upwelling region, the measured data and modeled output were in excellent agreement in terms of shape, order of magnitude and timing as the maximum vertical velocity occurred approximately four hours after CPA—some 11 hours before the maximum shallowing and minimum of the respective perturbations of the depth of the 26°C isotherm and TCHP. Remaining consist, the strongest forcing and addition of sea spray generated the greatest vertical velocities, which was also the largest response throughout the measurement interval.

While there was good agreement in both the downwelling and upwelling regions, this was only partially true within the internal wave response. In general, the measured data and modeled output all demonstrated alternating positive and negative vertical velocities with similar magnitudes on average, but unlike the previous variables, with a period much shorter than inertial. Naturally, the measured data has more of a "spiked" look through the oscillations of vertical velocity, but the modeled output seems to replicate several high frequency cycles. Furthermore, the disparity in modeled output collapsed in this interval, with each forcing parameter resulting in essentially the same vertical velocity profile over time. For this storm as a whole, the modeled output replicated the two predominant downwelling and upwelling features, indicated sub-inertial oscillations in the internal wave response and confirmed stronger forcing and the addition of sea spray increased the magnitude of the vertical velocities.

Branching out to all of the storms and positions, in every case, an initially downward and then upward vertical velocity near CPA was indicated, with some more marked than others. With that said, each of the storms and positions resulted in an 100% positive value of DWI for vertical velocity, as listed in Table 4.4. Also near CPA, in both the downwelling and upwelling regions, at least 50% of the measures of $\tau_{w\&s\_Gar}$ and τ_{w_Gar} resulted in vertical velocity magnitudes much greater than that of the float/glider data. For example, in the interaction between HU Irma and ALAMO 9129, as shown in Figure 4-13, $\tau_{w\&s\_Gar}$ and τ_{w_Gar} led to a maximum downwelling velocity 50-200% larger than measured respectively, with $\tau_{w\&s\_Gar}$ also being 50% greater in the upwelling region. Other than these two forcing parameterizations, none of the others distinguished themselves as more accurate than the next in any region, especially in the internal wave interval where the modeled output was in good agreement. With that said, as documented in HU Ignacio, the presence of sub-inertial oscillations was also present in the other storms and positions. Using HU Irma and ALAMO 9129, in Figure 4-13 for a second time, there were multiple, short oscillation wavelengths in the modeled output and measured data between

8-17 hours after CPA. While these "short waves" do not explicitly align in terms of amplitude, frequency and/or wavelength, they were observed with similar orders of magnitude in many of the storms and positions. This finding, which may be significant, as in addition to the maximum in vertical velocity preceding the upwelling, was also absent in traditional upper oceanic response theories, would require further research beyond the scope of this study to better understand. As a whole, the modeled output generally replicated the measured data, especially in the downwelling and upwelling regions, where the stronger forcing and addition of sea spray led to greater magnitude vertical velocities, but $\tau_{w\&s\_Gar}$ and τ_{w_Gar} seemed too large in many cases.

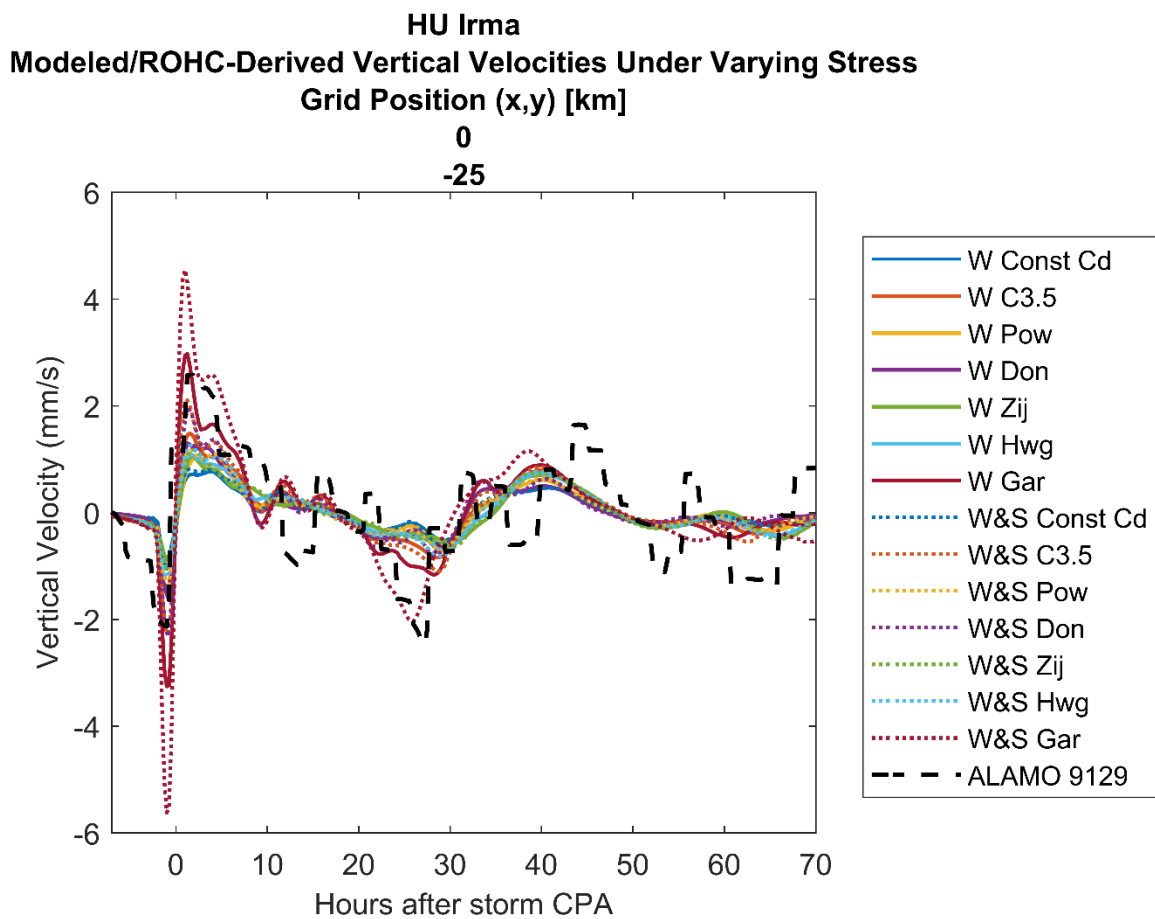Figure 4-13: Modeled and ROHC-derived vertical velocity under varying stress, during the passage of HU Irma, as measured by ALAMO 9129 and initialized nine hours prior to its CPA with the storm. Solid and dotted lines represent model output, w_{PWP}, with τ_w and $\tau_{w\&s}$ forcing respectively, under a variable C_D. The black dashed line represents w_{ROHC}, derived from measured data.

4.3.2.4 Oceanic Response Trend Synthesis and Way Forward

A few commonalities arose from this initial, primarily qualitatively graphical comparison of the modeled output and measured data across all storms and float/glider positions. First and overall, the modeled output from each of the three variables (with ROHC feeding vertical velocity) replicated the measured data, in most cases, in terms of shape, sign, order of magnitude, and frequency. There were no storms and positions where a great disparity was present between the modeled output and measured data and the main findings of sequential downwelling, upwelling and internal waves remained consistent throughout, albeit with varying magnitudes. Second, as expected, the magnitude of the modeled response was directly proportional to the strength of the forcing, with the lone exception of the TCHP perturbation in HU Ignacio. The aforementioned strength applies to both the drag coefficient as well as the addition of sea spray, which always led to a higher magnitude response than that of wind only stress. Third, despite the last trend, no one forcing parameterization appeared to be more accurate than the rest across all measurement comparisons. Furthermore, some were better in certain intervals of the storms' passages, including $\tau_{w\&s\_Gar}$ and τ_{w_Gar}, which sometimes replicated the measured data very well in the downwelling region, but was much too strong in the upwelling and internal wave regions. With that being said, while inquiries concerning the validity of Garratt's C_{DN} certainly remained, a largely quantitative analysis was required to formally address the issue of accuracy.

In terms of accuracy, several specific questions remained. First, whether there were any outliers within the drag coefficients, particularly aiming to address the prior discrepancies identified with Garratt's C_{DN}. Second, do any of the forcing parameterizations perform significantly different across the various time intervals with respect to storm passage? Third, was the addition of sea spray more or less accurate than wind only stress? Fourth, ultimately, which combination of drag coefficient and sea spray/wind only stress forcing was best? Finally, fifth, were there any trends relating the deltas between the modeled output and measured data to storm characteristics such as translation speed, maximum wind speed and/or measurement position?

In order to address these, the following procedure was applied. First, the difference between the modeled output and measured data was computed for each point of the latter, which required linear interpolation of the former to match indices. Next, the mean of the magnitude of these

differences was computed for each storm and measurement position and oceanic response variable (except ROHC directly). The original deltas were then normalized by the mean of their respective variable across all storms and positions, allowing for each variable to have equal weight. For example, a delta between the perturbation depth of the 26°C isotherm, TCHP perturbation and vertical velocity might have been 10 m, 15 $\frac{kJ}{cm^2}$ and 2 mm/s respectively, but after normalization by that storm and position's variable mean, the now unit-less quantities allowed for a fair comparison. This baseline set of data, which will be referred to as point by point (PbP) differences, was then applied in a variety of ways to answer the five questions above and will be described in the following sections.

4.3.2.5 Plausible Drag Coefficients

With the ultimate goal of determining the most accurate forcing parameterization, the first step was attempt to identify any outliers. In order to do so, the normalized mean PbP differences were cumulated and partitioned with respect to their forcing parameterization and variable, for each of the six storm/positions. Subsequently, these data were plotted along with their mean and one standard deviation, as illustrated in Figure 4-14, which includes the comparison for each of the three variables over the total measured time interval. The utility in these graphics was the ability to determine relative forcing accuracy, by identifying the following: the lowest (highest) cumulative normalized delta indicating the least (greatest) difference between the measured data, where values falling outside of one standard deviation were deemed to be statistically significant. From this analysis across the total measured time interval, two key findings were made. First, in each of Figures 4-14, none of the forcing parameterizations were more accurate than the others to a statistical significance, as not one of the 56 vertical bars was found below one standard deviation of the mean. While some were better for certain variables, summing across each in Figure 4-14d, the lowest cumulative normalized delta was found to be $\tau_{w\&s\_Pow}$. Second, there were only ten accumulations that landed above one standard deviation, but seven of those were either $\tau_{w\&s\_Gar}$ and τ_{w_Gar}. This confirms earlier observations in which the forcing parameterizations using Garratt's C_D were often too strong; however, since these seemed to perform well in the downwelling region in the qualitative analysis, it was prudent to further partition the time interval into subsections. Such a test would indicate if a certain

84
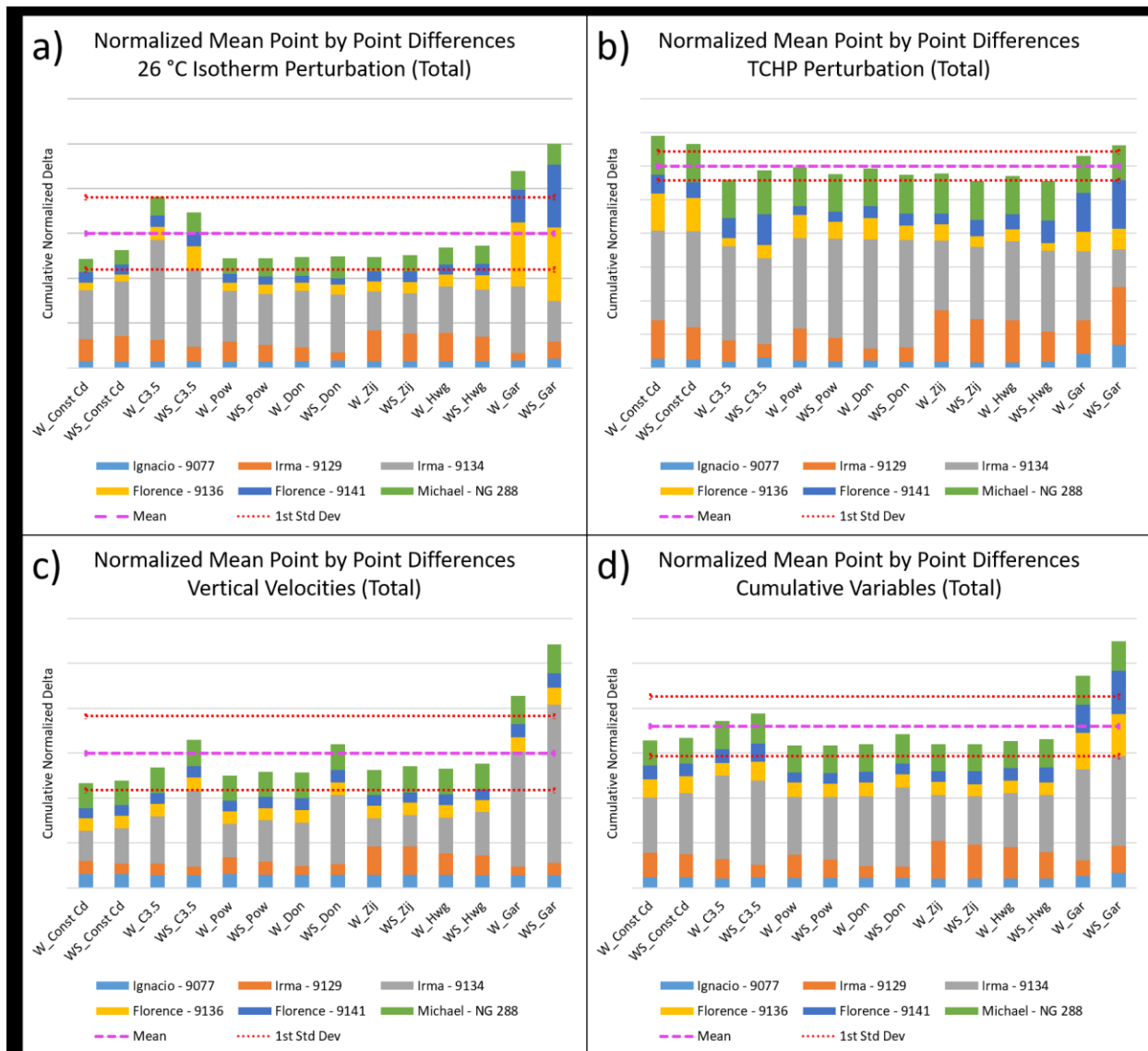
Figures 4-14a, 4-14b, 4-14c, 4-14d: a) Normalized mean PbP differences of the perturbation depth of the 26°C isotherm, over the total measured interval, for all storms and locations; b) TCHP perturbation (as in (a)); c) Vertical velocities (as in (a)); and d) Cumulative variables (as in (a)). The contribution from each storm/measurement device is identified with a solid color and the mean and first standard deviation of the data set are plotted in dashed magenta and red lines respectively.

parameterization performed better as a function of storm passage, specifically looking to address the downwelling and upwelling regions. As such, the downwelling region was defined in this test as the time of the first measurement through six hours post-CPA, aimed to obviously assess the downwelling, while an inertial period (IP), defined as the time of first measurement through the length of one IP (as computed for each storm), would capture both the downwelling and upwelling. Between these two subintervals, if any one forcing parameterization was better
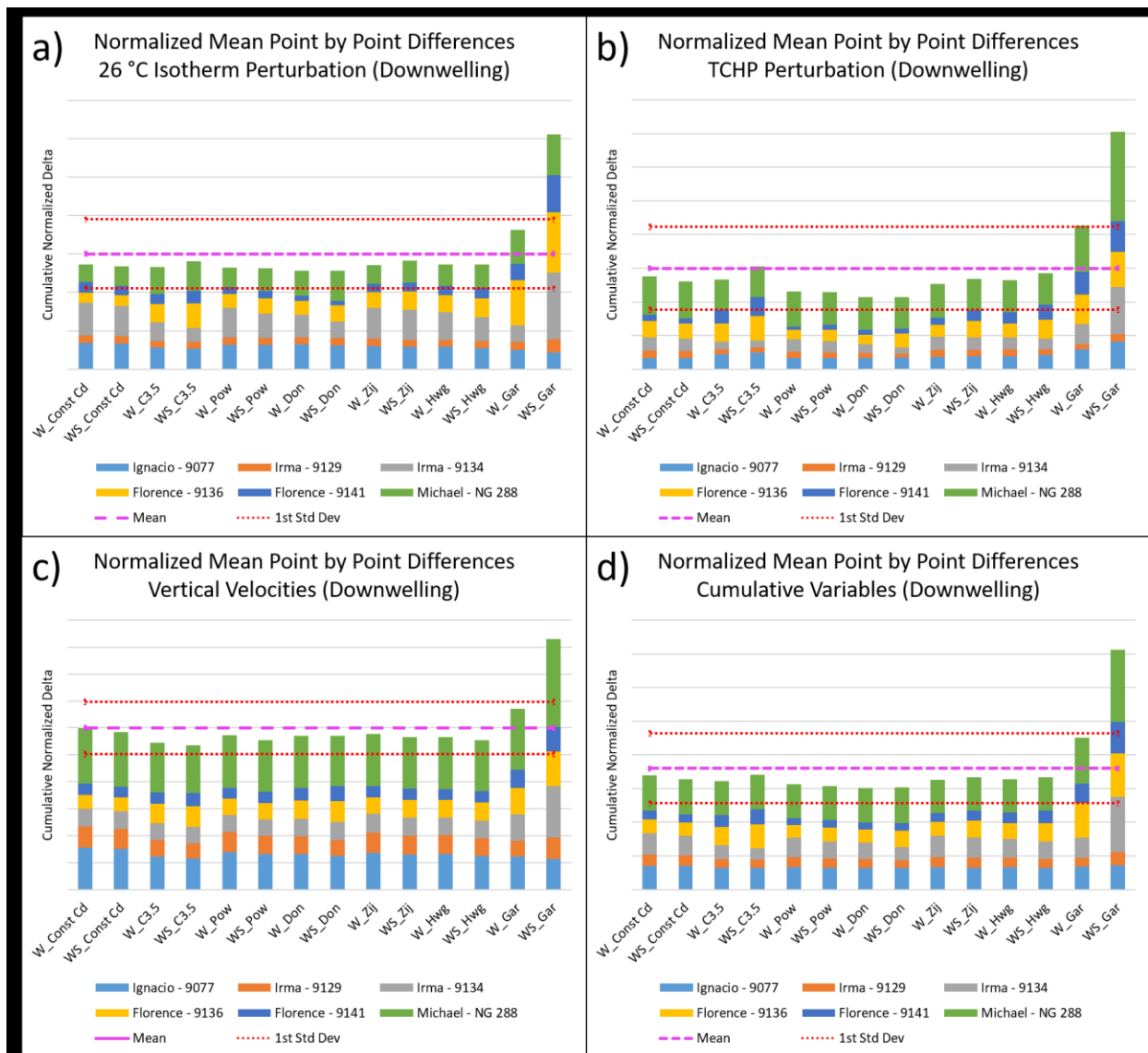
Figures 4-15a, 4-15b, 4-15c, 4-15d: a) Normalized mean PbP differences of the perturbation depth of the 26°C isotherm, over the downwelling region, for all storms and locations; b) TCHP perturbation (as in (a)); c) Vertical velocities (as in (a)); and d) Cumulative variables (as in (a)). The contribution from each storm/measurement device is identified with a solid color and the mean and first standard deviation of the data set are plotted in dashed magenta and red lines respectively.

during just the downwelling or under the greatest stress, but did not perform as well in a later region, they would be identified. The results for each variable and in cumulative form, which are displayed in Figures 4-15 and 4-16, indicated much of the same as the total interval in which there remained no statistically significant best forcing and this time $\tau_{w\&s\_Gar}$ and τ_{w_Gar} were responsible for all 12 instances where the cumulative normalized deltas exceeded one
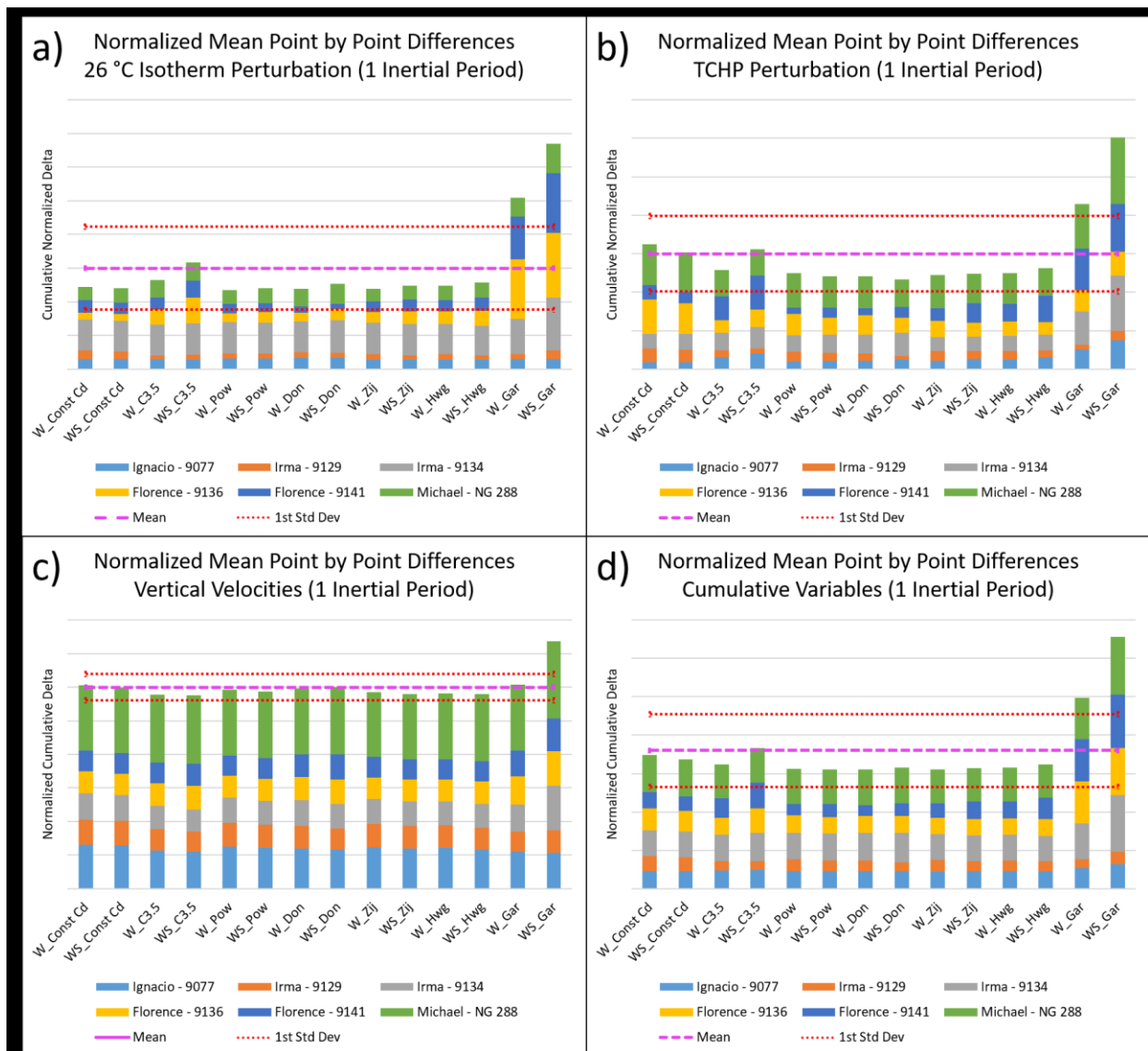
Figures 4-16a, 4-16b, 4-16c, 4-16d: a) Normalized mean PbP differences of the perturbation depth of the 26°C isotherm, over the first inertial period, for all storms and locations; b) TCHP perturbation (as in (a)); c) Vertical velocities (as in (a)); and d) Cumulative variables (as in (a)). The contribution from each storm/measurement device is identified with a solid color and the mean and first standard deviation of the data set are plotted in dashed magenta and red lines respectively.

standard deviation. In fact, during the three intervals of the downwelling region, IP and total, the forcing parameterizations using Garratt's C_D were 161.6%, 160.2% and 154.6% greater than their respective means. Furthermore, while early indications pointed to $\tau_{w\&s\_Gar}$ and τ_{w_Gar} being fairly accurate in the downwelling region, at least in some cases, this interval turned out to be their least precise. Consequently, it was determined the forcing parameterizations using Garratt's C_D were too strong and statistical outliers, which may have been skewing the data

enough to prevent a most accurate forcing from emerging. While the other six drag coefficients remained plausible, that of Garratt, along with legacy parameterizations in general, was deemed to be not realistic based on this study.

Figures 4-17a, 4-17b, 4-17c: a) Normalized mean PbP differences of the cumulative variables, excluding Garratt's C_D forcing parameterizations, over the downwelling period, for all storms and locations; b) Inertial period (as in (a)); and c) Total measured interval (as in (a)). The contribution from each storm/measurement device is identified with a solid color and the mean and first standard deviation of the data set are plotted in dashed magenta and red lines respectively.
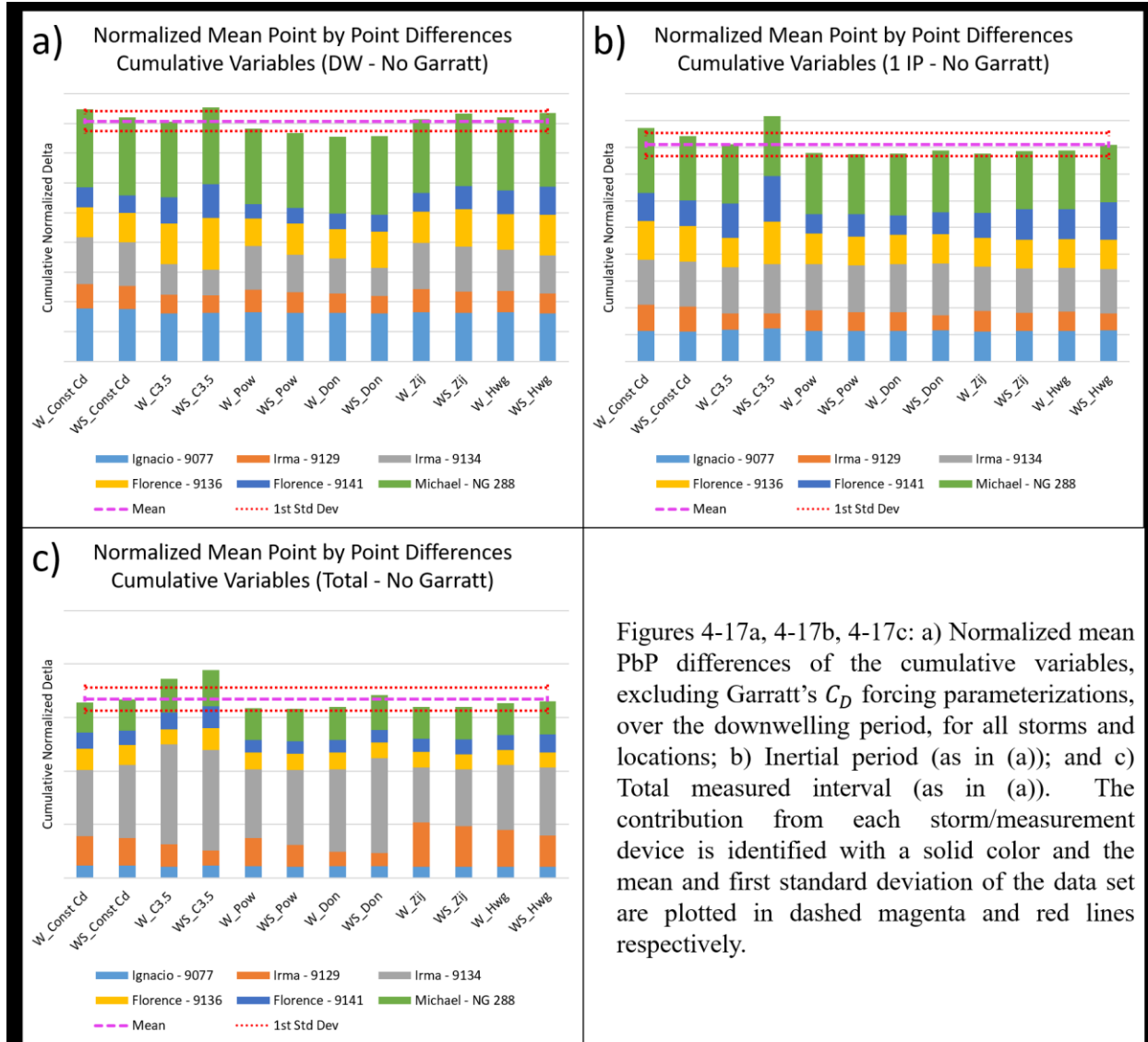
As a result, it was judicious to repeat this same analysis after the removal of the two aforementioned outliers, with the results of the cumulative variables displayed in Figure 4-17. A few key findings emerged from the second version of this test, including first, a noticeable collapse in the spread in the data. With the removal of the forcing parameterizations using Garratt's C_D, the mean standard deviation plummeted by 69.1%—a remarkable amount further cementing $\tau_{w\&s\_Gar}$ and τ_{w_Gar} as outliers. As a result, it no longer required a marked departure from the mean to indicate accuracy to a statistical significance, but was only achieved by

$\tau_{w\&s\_Pow}$, $\tau_{w\&s\_Don}$ and τ_{w_Don} in the downwelling interval. On the contrary, the strongest remaining forcing parameterization was C3.5, which proved to be statistically significantly inaccurate in 66.7% of metrics. Interestingly enough, while the forcing formulations using C3.5 and Donelan's C_D were at both ends of the accuracy spectrum, as illustrated in Figure 2-1 and mentioned in Section 2.2.6, these parameterizations are exactly equal for $U_{10} \geq 33$ m/s, which made their discrepancy surprising and demanded the cause be attributed to sub-storm force wind stress. Overall, for the most accurate forcing, by the slimmest of margins, $\tau_{w\&s\_Pow}$ was more precise than τ_{w_Pow} as they were 0.82% and 0.80% better than the next closest forcing parameterization, respectively, relative to the mean. With that said, however, as illustrated in Figure 4-17c, none of the forcing parameters were statistically significantly lower than the mean, throughout the total time interval.

4.3.2.6 Effect of Sea Spray

To assess the effect of sea spray, two separate analyses were conducted. First, an inquiry was completed to determine the relative importance of the inclusion of sea spray. Simply, initially apart from accuracy, the goal was to quantify just how much sea spray affected the three variables of the upper oceanic response during TC passage. To do so, the difference between the individual modeled output of the depth of the 26°C isotherm, TCHP and vertical velocity for $\tau_{w\&s}$ and τ_w was computed and averaged across all storms/locations. These values, which are listed in Table 4.5a, carried some weight on their own (as they did contain units, unlike the normalized mean PbP data), but to help determine their relative importance, each quantity was compared to the mean of their respective measured variable. These secondary results, which are recorded in Table 4.5b, confirm the expected finding where the stronger the forcing parameterization, the greater the difference that was made by sea spray. In addition, when splitting the means across all variables and forcing parameterizations between including and excluding those with Garratt's C_D, the overall mean difference generated by adding spray was 10.3% relative to measured quantities. This value is nearly exactly the same as a similar quantity postulated by Andreas [19], where he believed 10% of the total interfacial stress was attributable to sea spray, at wind speeds of 30 m/s. While these metrics certainly do not allow for an apples-to-apples comparison, it stands to reason the percentage of $\tau_{w\&s}$ attributable to τ_{sp} is at least proportional and likely of the same order as the relative mean difference for spray and no spray,

Summary of Mean Sea Spray vs. No Spray Delta for all Storms									
a)	Forcing: Wind & Spray – Wind Only							Means	
Variable	Const C_D	C3.5	Pow	Don	Zij	Hwg	Gar	All	No Garratt
Depth of 26°C Isotherm (m)	0.87	2.55	1.65	1.92	1.21	1.36	12.90	*3.21*	*1.59*
TCHP (kJ/cm^2)	1.10	4.07	2.24	4.43	2.27	2.70	7.56	*3.48*	*2.80*
Vertical Velocity (mm/s)	4.2e-5	3.4e-4	6.6e-5	2.6e-4	6.1e-5	7.5e-5	3.2e-4	*1.7e-4*	*1.4e-4*

Summary of Relative Mean Sea Spray vs. No Spray Delta for all Storms									
b)	Relative Forcing: Wind & Spray – Wind Only vs. Measured							Means	
Variable	Const C_D	C3.5	Pow	Don	Zij	Hwg	Gar	All	No Garratt
Depth of 26°C Isotherm	1.2%	3.6%	2.3%	2.7%	1.7%	1.9%	18.0%	*4.5%*	*2.2%*
TCHP	2.3%	8.5%	4.7%	9.3%	4.8%	5.7%	15.8%	*7.3%*	*5.9%*
Vertical Velocity	5.7%	46.6%	8.9%	35.2%	8.3%	10.1%	43.8%	*22.7%*	*19.1%*
Average	*3.1%*	*19.6%*	*5.3%*	*15.7%*	*4.9%*	*5.9%*	*25.9%*	**11.5%**	**9.1%**

Tables 4.5a, 4.5b: a) Summary of mean sea spray vs. no spray delta for all storms/locations as partitioned by upper oceanic response variable and forcing parameterization; b) same as in (a), but compares each value to the measured mean across all storms/locations. The italicized percentages represent the means for each variable and forcing parameterization, with the left column including all forcing parameterizations and the right excluding those with Garratt's C_D.

across the upper oceanic response variables. In this case, they are essentially equal, helping to confirm Andreas' assertion as well as validate the architecture and data analysis used within this study.

Next, a very similar analysis to that of the previous section was completed in order to compare the accuracy of stress with and without sea spray. After removing the forcing outliers, the sum of the normalized mean PbP differences across the withstanding model parameterizations was computed, but partitioned between stress with and without spray. These data, which are displayed in Figure 4-18, contained a standard deviation that was only 1.1% of
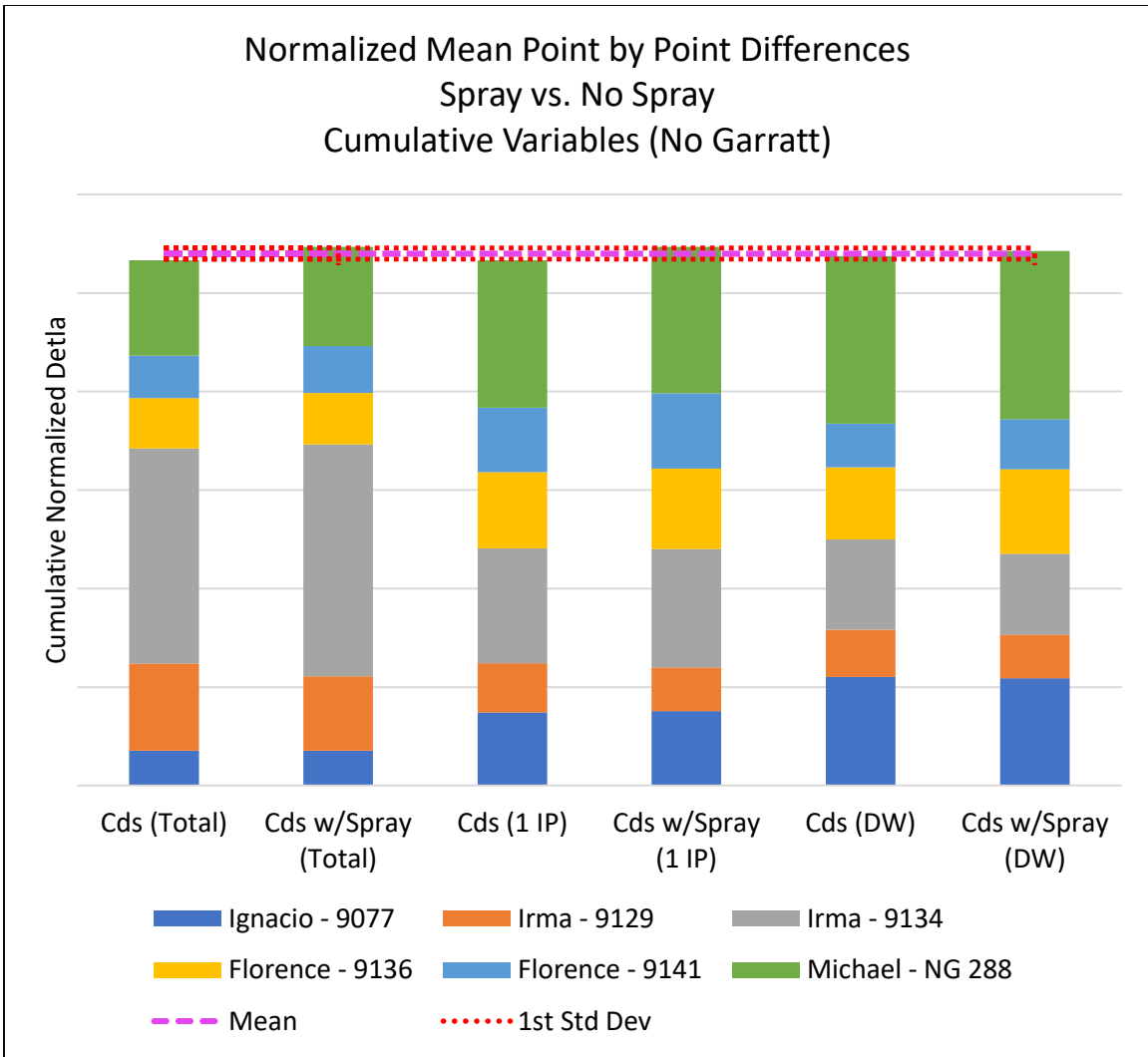
Figure 4-18: Normalized mean PbP differences of the cumulative variables, excluding forcing parameterizations using Garratt's C_D, over the total measured interval. The contribution from each storm/measurement device is identified with a solid color and the mean and first standard deviation of the data set are plotted in dashed magenta and red lines respectively.

the mean, making the statistical significance difficult to verify visually. With that said, in each interval, the cumulative variables were an average of 2.0% more accurate *without* sea spray, with the inertial period and total measured interval indicating such to a statistical significance. Overall, sea spray had about a 10% increase in the magnitude of the upper oceanic response variables during TC passage, but including such in models made their output less accurate.

4.3.3 Best Forcing

Several different tests over multiple variables, time intervals and storms/locations were conducted in order to attempt to determine the most accurate forcing (amongst other analyses). As a brief synopsis, when first considering the total time interval across each of the upper oceanic response variables, it was $\tau_{w\&s\_Pow}$ that was only slightly more accurate than several of the other parameterizations, but not to a statistical significance. The most substantial finding of this test actually went the opposite way as $\tau_{w\&s\_Gar}$ and τ_{w_Gar} appeared to be outliers, to a statistical significance, in seven out of their eight measures. Based on previously conducted qualitative tests, however, $\tau_{w\&s\_Gar}$ and τ_{w_Gar} performed well within the downwelling region, motivated by observations in HU Ignacio (Figures 4-8 and 4-10). As a result, the second test partitioned the data into subintervals that included the downwelling region and first IP, aiming to capture any forcing parameterizations that performed better as a function of storm passage. Not only did these results also fail to indicate a statistically significant most accurate forcing, but they also confirmed $\tau_{w\&s\_Gar}$ and τ_{w_Gar} as clear outliers, where 12 of their 16 metrics were greater than one standard deviation from the mean. In an effort to pare down the data, the same tests were then conducted after the removal of the forcing parameterizations using Garratt's C_D. This third test maintained the theme where although $\tau_{w\&s\_Pow}$ remained the most accurate forcing, the results were not to a statistical significance. Finally, the accuracy of stress including sea spray vs. wind only was completed, which to a statistical significance, indicated the addition of the former produced less accurate modeled output.

Based on these results, there are three clear conclusions including legacy drag coefficients are too strong under TC force winds, the addition of sea spray does not improve model accuracy and there is no singular best forcing parameterization of those selected for this study. With that said, these outcomes do help to further the motivation for a modern C_D parameterization that maximizes between storm and TC force winds and slightly decreases to an asymptote, as illustrated in Figure 2-1. In addition, while the explicit addition of sea spray to the interfacial stress (equation 3.3f) led to less accurate modeled output, the modern drag coefficient is predicated on that same spray dampening its value at high winds speeds. At such wind velocities, it is believed that wave crests are sheared off by this extreme forcing, which sends sea spray into the atmosphere. However, as detailed in Chapter 3, these droplets quickly accelerate

to near the wind speed and return to the ocean. While the momentum transfer of these droplets from the atmosphere to the ocean was presented previously, the secondary effect of the spray flattening the smaller waves upon reentry has not be introduced [19]. As such, while the wind alone limits wave heights by clipping the largest crests, the resulting spray then reduces the size of smaller waves. Taken together, under extreme wind forcing, wind and spray limit the wave field and as such, do the same to the drag coefficient. As a fourth conclusion from the aforementioned tests, while the methodology used to parameterize $\tau_{w\&s}$ triggered less accurate results, the effect of sea spray remains important in TC modeling through the drag coefficient as it is paramount that a C_D is selected incorporating such effects, through a decreasing or asymptotic relationship under extreme winds.

4.3.4   Trends in Storm Characteristics

Each of the aforementioned analyses involved solely comparing the accuracy of the modeled output to the measured data, but essentially taking the storms/locations to be equal. The following three graphical analyses will again consider the modeled vs. measured accuracy, but this time as a function of storm characteristics or position, including translation and maximum wind speed as well as track position. As a bit of a disclaimer, unfortunately, all of the subsequent outcomes only involved 4-6 storm metrics, resulting in a severely data limited set of tests. With that said, however, the some of the findings remain noteworthy and as such, are included.

   The first of these studies involved a comparison of the normalized mean PbP differences, cumulated over all variables, vs. the translation speeds of the four storms. As such, this relationship includes two sets of measures from HUs Irma and Florence, but from different positions, lending to a spread in the data at their respective translations speeds, as depicted by Figure 4-19. Consequently, the shapes of the trend lines, which were set based on determining the largest values of R^2 between exponential, linear, logarithmic, polynomial (order 2-3) and power fits, are very distinct across the individual forcing parameterizations. Despite the data bias, one trend that was illuminated by this analysis involved an increase in the difference between the modeled output and measured data as a function of translation speed. This phenomenon could be physically related to the wave age as faster moving storms have younger

waves with larger drag, thus enhancing the forcing on the ocean. While such an effect would be captured through measured data, wave age was not explicitly considered within the PWP model.

The second storm characteristic analysis was very similar to the previous, but rather than translation speed, the dependent variable was adjusted to each storm's maximum wind speed. While this investigation was certainly natural and practical, no consistent or physically-based trends were illuminated and as such, it will only be mentioned, but not further expounded.
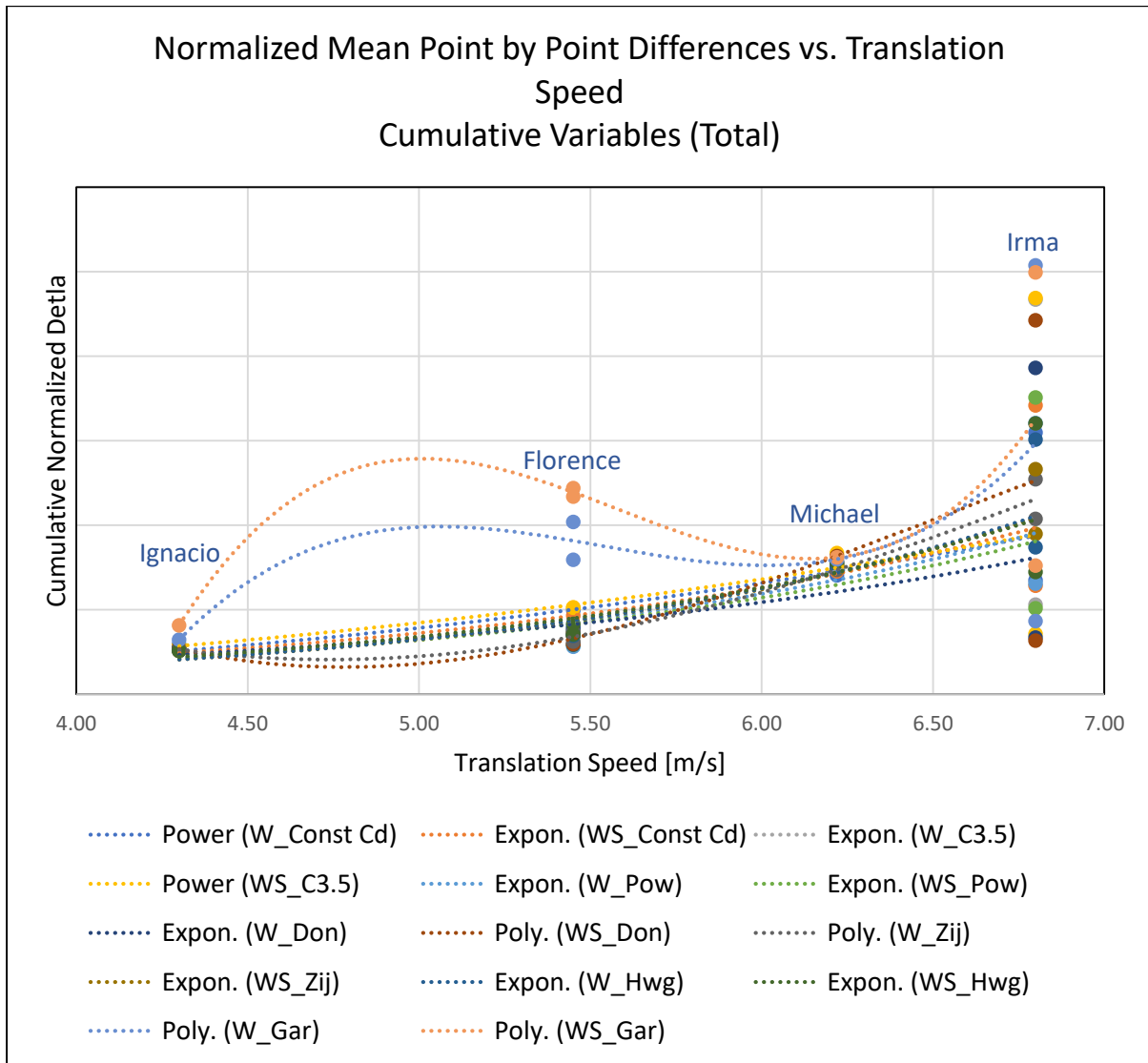

Figure 4-19: Normalized mean PbP differences of the cumulative variables, over all forcing parameterizations and the total measured interval, vs. storm translation speed. The individual trend lines were determined based on the largest value of R^2 between exponential, linear, logarithmic, polynomial (order 2-3) and power fits.

The final analysis involving the normalized mean PbP differences as well as storm characteristics was a comparison as a function of the relative distance from the track. Unlike the two previous inquiries, the distance from the storm's track was not uniform for HUs Irma and Florence as the dependent variable was predicated on the position of the individual floats/gliders. As a result, the "stacked" data bias was absent, which was conducive to more judicious outcomes. To approximate the relative distance from the track, the magnitudes of the measurement devices' model grid positions were computed. Next, the notional storm track was rotated to align with the y-axis, where storms left (right) of track were assigned a negative (positive) distance from the origin, the HUs' assumed center. Finally, with the distances left and right of track determined, the cumulated normalized mean PbP deltas for all variables and forcing parameterizations, partitioned by sub-interval, were plotted per storm, as illustrated in Figure 4-20. After repeating the trend line process from the first analysis, two key trends emerged. First and most notably, the greatest modeled to measured delta for the total interval and IP was found approximately 25-30 km right of track, which was to be expected based on the following factors. First, as demonstrated in Section 4.1.1.1, the storm's additive wind and translation speed as well as wind stress forcing and inertial current resonation on the right side of any NH storm, cause that side to have the greatest oceanic response. Second, in each of the four storms used herein, the radius of maximum winds was measured at 28 km. Taken together, the strongest forcing experienced in this study, across each HU, was approximately 28 km right of track. As a result, one might intuitively hypothesize the greatest deltas would be found under the strongest forcing through a contrapositive, when there is no forcing, as long as the initialization was effective, there should be only small differences between modeled output and measured data. Furthermore, as evidenced by the poor accuracy of forcing parameterizations using Garratt's C_D as well as that of C3.5, which is clearly displayed by Figure 4-17, generally the stronger the forcing, the less model precision against measurement. Consequently, at least in this study, it was expected that the largest deltas would fall at the location of the greatest forcing. Second, as related to the first observation, the delta between modeled output and measured data generally decreased when moving away (both to and from) the radius of maximum winds.

As mentioned above, the storm trend analyses were all data limited, however, each of their observations, whether random or statistically significant, were supported by physical phenomena. As such, these results separately and qualitatively helped to validate the precision

95
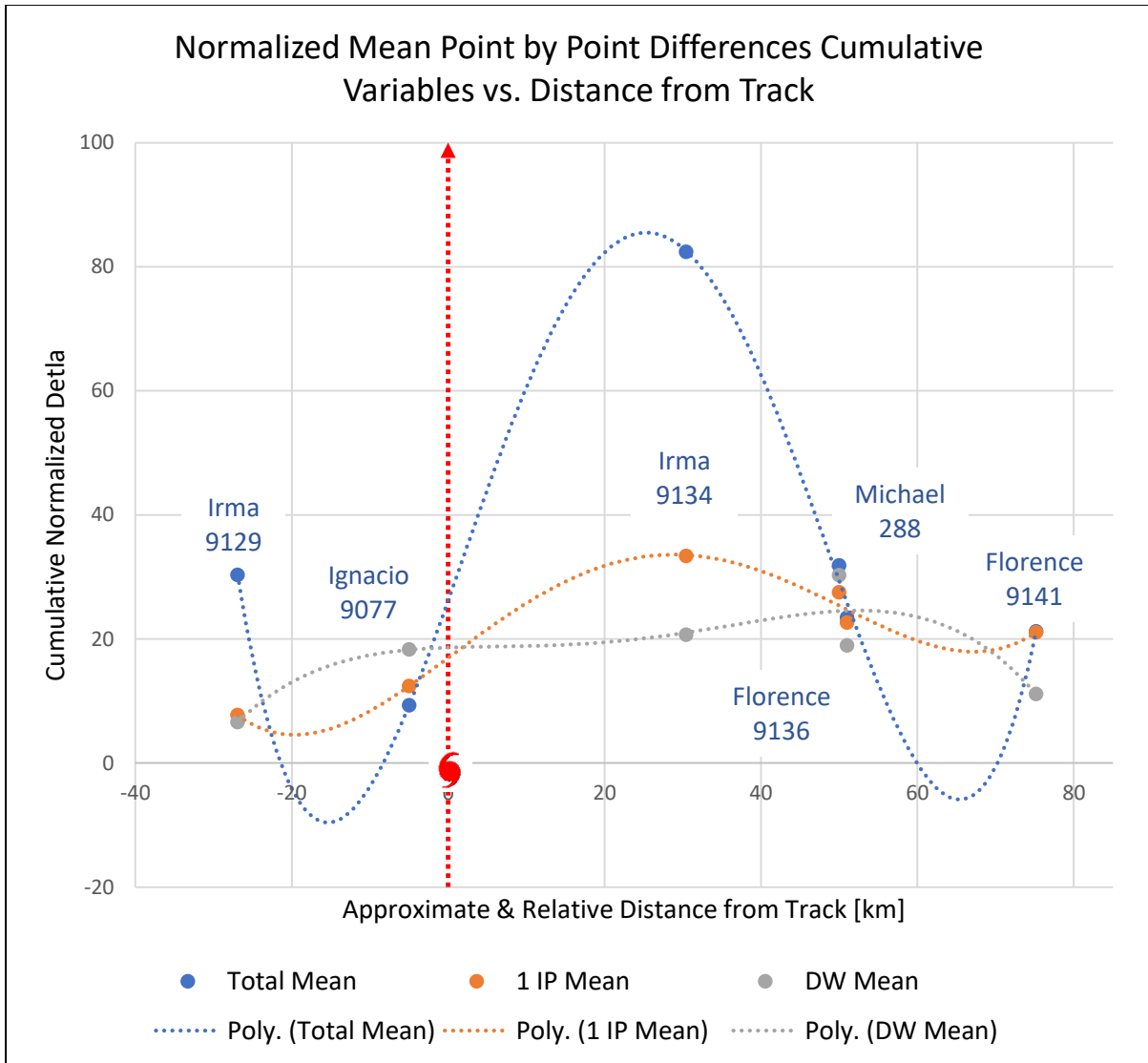
Figure 4-20: Normalized mean PbP differences of the cumulative variables, summed over all forcing parameterizations and partitioned by sub-interval, vs. the float/gliders' approximate and relative distance from the storm track. To standardize across all storms and facilitate visual trend analysis, each storm was rotated to translate along the y-axis, centered at the origin, with the approximate distance left and right of track computed based on the magnitude of the float/gliders' positions. The individual trend lines were determined based on the largest value of R^2 between exponential, linear, logarithmic, polynomial (order 2-3) and power fits.

of the previous PbP statistical analyses. In another way, if the results of these last two

investigations would not have been founded in physics, it would begin delegitimize the

previously presented statistical outcomes. While all of these trends would require further

research to statistically confirm, they are physically based and comforting to the overall analyses performed herein.

THIS PAGE INTENTIONALLY LEFT BLANK

Chapter 5

Downwelling and Drag Coefficients Revisited

5.1 Ekman Velocity

In Section 4.3.1, downwelling ahead of TC passage was demonstrated based upon a modeled and measured deepening of the 26°C isotherm, increase in TCHP and ultimately a negative vertical velocity. For completeness, it was also practical to use Ekman layer dynamics to separately model the upper oceanic response. This method did involve some of the same principles applied earlier, but was independent of TC intensity metrics and embedded PWP model design. Additionally, Ekman layer dynamics are a good, relatively simple way to qualitatively determine the sign of the vertical velocity as a function of stress. As such, this second investigation to verify the presence of downwelling was not only aimed to strengthen the argument, but also place a physical explanation to its origination outside of TC specific metrics.

In general, Ekman dynamics describe the oceanic (and atmospheric) layer in which large-scale flow, where the effects of rotation are significant, has a balance between the Coriolis force and friction and/or stress [49]. While such a region is not present in the majority of the ocean, it is important near the surface where stress from the atmosphere can impart small-scale turbulence, which diffuses throughout a layer ranging from tens to a few 100 m thick [49]. Despite great technological and geophysical fluid dynamic (GFD) research advancements, most turbulence remains parameterized to this day, which is required in the case of the wind stress imparted upon the ocean's surface. To begin deriving the Ekman layer, one must commence with the horizontal Navier-Stokes equation of motion, having made the hydrostatic and Boussinesq approximations (as before in Section 4.1.2.1 within the PWP model), as given by

$$\frac{Du}{dt} - fv = -\frac{1}{\rho_w}\frac{\partial p}{\partial x} + A\nabla^2 u \text{ and } \frac{Dv}{dt} + fu = -\frac{1}{\rho_w}\frac{\partial p}{\partial y} + A\nabla^2 v, \text{ (5.1a, 5.1b)}$$

where A is the viscosity constant. Next, to incorporate the stress forces through the frictional terms while keeping the units intact, the following parameterization is made, where

$$A\nabla^2 \boldsymbol{u} = \frac{1}{\rho_w}\nabla\boldsymbol{\tau}. \tag{5.1c}$$

In the upper ocean as well as generally in GFD, however, it is common to assume vertical derivatives are much larger than the horizontal, which leaves the following relationship when combining equations (5.1a), (5.1b) and (5.1c), as given by

$$\frac{Du}{dt} - fv = -\frac{1}{\rho_w}\frac{\partial p}{\partial x} + \frac{1}{\rho_w}\frac{\partial \tau^x}{\partial z} \text{ and } \frac{Dv}{dt} + fu = -\frac{1}{\rho_w}\frac{\partial p}{\partial y} + \frac{1}{\rho_w}\frac{\partial \tau^y}{\partial z}, \tag{5.1d, 5.1e}$$

where $\frac{\partial \tau^x}{\partial z}$ and $\frac{\partial \tau^y}{\partial z}$ are the vertical wind stress vectors [49]. Under the aforementioned condition where the Coriolis and stress forces balance, several terms vanish, leaving the following principle relationships for Ekman dynamics, as given by

$$-fv = \frac{1}{\rho_w}\frac{\partial \tau^x}{\partial z} \text{ and } fu = \frac{1}{\rho_w}\frac{\partial \tau^y}{\partial z}. \tag{5.1f, 5.1g}$$

At this stage, it is useful to compare this result to that of the scaling of equation (4.1c) for a TC, as described in Section 4.1.2.2. In each case, the remaining terms match, making the Ekman layer a good proxy for the upper oceanic response to TC passage, despite the incongruence in some of the physical processes at hand. Subsequently, after taking the derivatives with respect to x and y of equations (5.1g) and (5.1f) respectively, subtracting the result and applying continuity [50], the vertical velocity (w) then arrives via

$$\frac{1}{\rho_w}\frac{\partial}{\partial z}\left(\frac{\partial \tau^y}{\partial x} - \frac{\partial \tau^x}{\partial y}\right) + \frac{\beta}{\rho_w f}\frac{\partial \tau^x}{\partial z} = -f\frac{\partial w}{\partial z}, \tag{5.1h}$$

where β is the change in the Coriolis parameter with respect to latitude $\left(\frac{\partial f}{\partial y}\right)$. Afterward, the equation is integrated from the Ekman layer depth to the surface and scale analysis[10] allows the removal of the β term, which is at least an order of magnitude smaller than the others in a TC. The final result provides an equation for the vertical velocity at the Ekman layer depth, simply known as the Ekman velocity (w_E), as given by

---

[10] β can be further expressed as $\frac{\partial f}{\partial y} = 2\Omega\cos(\phi_o)/R$, where Ω is the rotation rate of the Earth $\left(\Omega \approx 7.29\text{x}10^{-5}\frac{rad}{s}\right)$, ϕ_o is the initial or median latitude and R is the radius of the Earth ($R \approx 6371\ km$). Furthermore, $f = 2\Omega\sin(\phi_o)$. These values are included to provide background for the following scale analysis comparing the left terms in equation (5.1h). After removing the like and equating the remaining terms, the following relationship arises within an TC: $L^{-1} \gg (R\tan(\phi_o))^{-1}$, thus $\frac{\beta}{\rho_w f}\frac{\partial \tau^x}{\partial z}$ is dropped.

$$\frac{1}{\rho_w f}\left(\frac{\partial \tau^y}{\partial x} - \frac{\partial \tau^x}{\partial y}\right) = w_E, \tag{5.1i}$$

where $\left(\frac{\partial \tau^y}{\partial x} - \frac{\partial \tau^x}{\partial y}\right)$ is the vertical curl of the wind stress. Using this result, both the explicit equation (5.1i) and the vertical curl of wind stress, the sign and magnitude of the vertical velocity could be modeled as well as qualitatively reasoned, as described below.

Beginning qualitatively, when taking the vertical curl of the wind stress vector (or any physical principle), the orientation of the wind stress can lead to vertical motion. From a Eulerian perspective, when the wind stress (curl) is cyclonic (positive) and anti-cyclonic (negative), the oceanic response is upwelling and downwelling, respectively. This simple concept can be applied to a passing TC by considering a notional vector wind field and assessing the orientation of the wind stress at various points, thus deducing the sign of the vertical velocity. In Figure 5-1 below, a Rankine vortex has been used to model a NH, category 5 HU, translating due west at 7 m/s, where the colored vectors indicate the magnitude and direction of the wind. By applying Eulerian principles, an assessment of the wind's orientation can be made working west to east, as if the storm had passed over a moored buoy with an anemometer. Ahead of the storm, at point one, there is a negative wind stress curl and anti-cyclonic flow due to weaker, northerly winds to the west and stronger, northerly winds to the east, thus leading to Ekman pumping or downwelling. Next at point two, after the passage of the radius of maximum winds, but before the eye, the traditional response of positive wind stress curl and cyclonic flow due to strong, northerly winds to the west and only light winds to the east in the eye, leads to Ekman suction or upwelling. The same response also occurs at the third point as after the passage of the eye, but before the rear radius of maximum winds, there is again cyclonic flow due to light winds to the west and strong southerly winds to the east, which leads to upwelling. Finally, at the fourth point, after the lion share of the storm has passed, there a second region of anti-cyclonic flow due to stronger, southerly winds to the west and weaker, southerly winds to the east, leading to downwelling. From this simple analysis, based on Ekman principles, the first upper oceanic response should have a negative Ekman velocity indicating downwelling ahead of upwelling.

Based on these ideas, it was then prudent to explicitly calculate and plot the Ekman velocity near the storms' CPAs, allowing for a comparison to the aforementioned qualitative theory as well as modeled and measured values. For the strongest assessment, HU Ignacio's interaction with ALAMO 9077 was selected because it was a near "direct-hit," thus the most similar to the
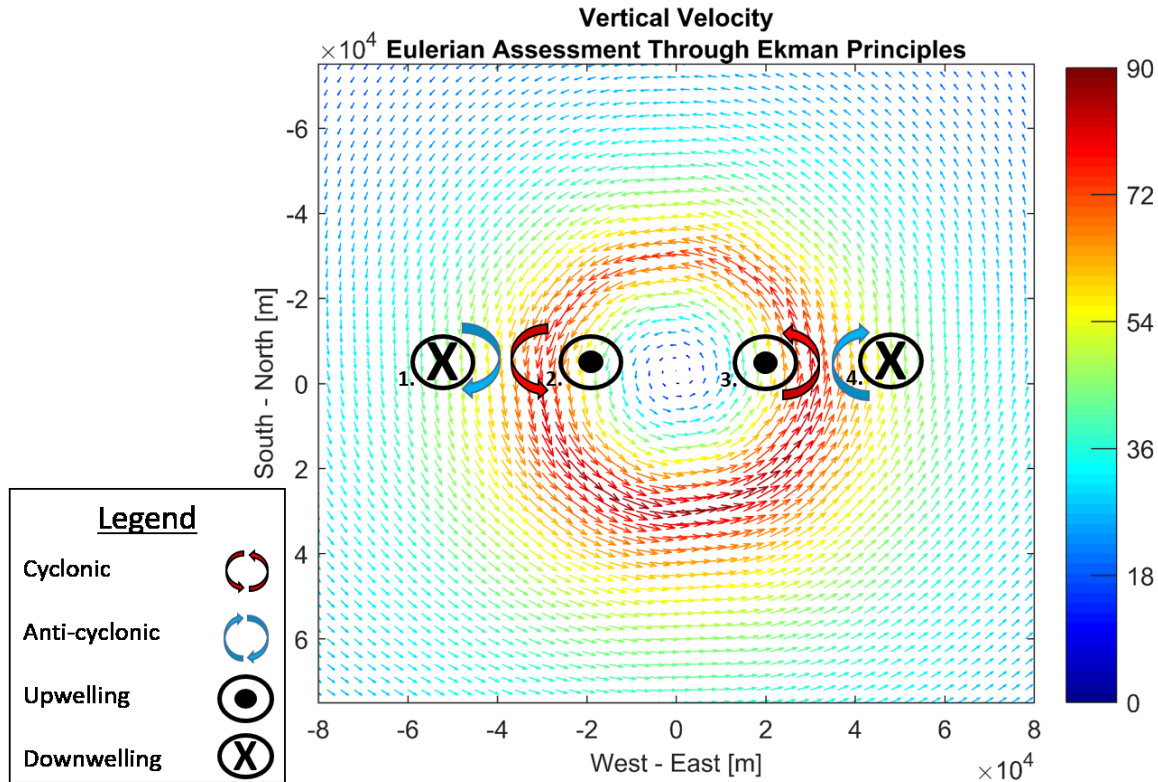
Figure 5-1: Eulerian assessment of vertical velocity through Ekman principles where each of the four locations illustrates the wind stress orientation and the sign of the Ekman velocity, with positive and negative w_E corresponding to upwelling and downwelling respectively. The background wind stress models a category 5 HU, translating at 7 m/s from east to west, with a Rankine vortex, where the color and size of the arrow indicate the wind's magnitude and direction at each grid point.

theoretical example of the storm's center passing right over the four points. As a result, Figure 5-2 illustrates the mean of the modeled Ekman velocities across each forcing parameterization as well as the ROHC-derived vertical velocity via float measurements. Beginning with the modeled Ekman velocities, the presented theoretical pattern is matched with downwelling, two maxima of upwelling, followed by downwelling after the storm's passage. The ROHC-derived, measured vertical velocity does not have the same magnitude as the Ekman velocity, but does show an initial downwelling, subsequent and significant upwelling, and then a slow recovery into the next downwelling cycle. Despite the magnitude and shape discrepancies, the measured vertical velocity response is supported by Ekman dynamics as the sign and relative amplitude of w_{ROHC} and w_E do match through the passage of the TC. This result continues to advance the argument of upper oceanic downwelling ahead of storm CPA using fundamental physical reasoning nearly independent from TC dynamics and intensity indices.
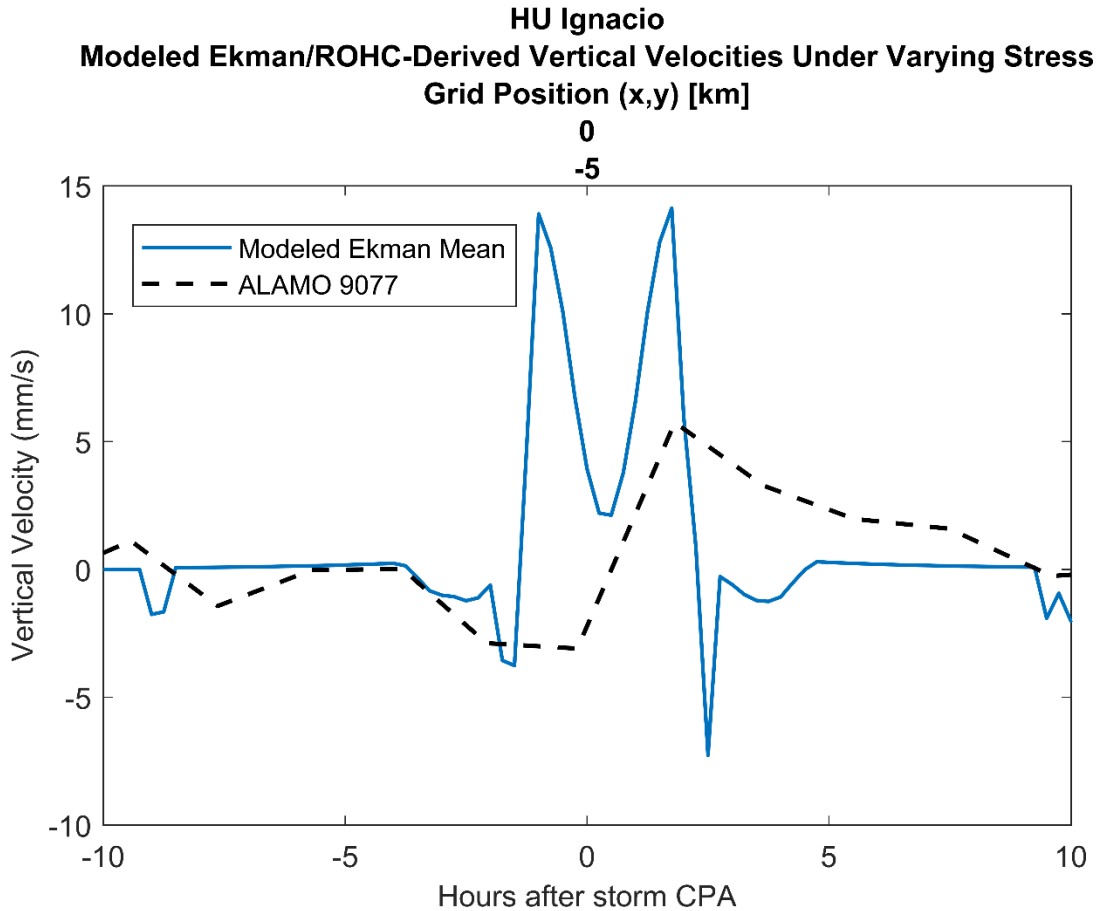
Figure 5-2: Modeled Ekman and ROHC-derived vertical velocity under varying stress, during the passage of HU Ignacio, as measured by ALAMO 9077 and initialized 12 hours prior to its CPA with the storm. The solid line represents the modeled $\overline{w_E}$ across all 14 forcing parameterizations while the black dashed line represents w_{ROHC}, derived from measured data.

5.2   Comparison with Other Studies' Results

While there have been many studies involving the upper oceanic response to a specific TC passage as well as attempts to best characterize the drag coefficient under extreme wind forcing, two studies in particular stood out as in terms of their alignment to the work herein. First, Jaimes and Shay [51] investigated the upper oceanic response to HUs Katrina and Rita passing over eddies and currents in the Gulf of Mexico, where they discovered downwelling in certain instances. Second, Zedler et al. [52] considered how different drag coefficients affected the SST and near-surface currents during the passage of HU Frances, where they found a marked difference using a constant C_D. Each of these has obvious connections to the motivation,

methodology and/or outcomes of this study and will be compared appropriately in the following sections.

5.2.1 Downwelling – Jaimes and Shay (2009)

In an effort to study the feedback between the Loop Current (LC) and warm and cold core eddies (WCEs and CCEs) during the passage of HUs Katrina and Rita, Jaimes and Shay [51] developed a multi-layered data synthesis to characterize the ocean's mixed layer, including its vertical velocity. Their overall dataset included airborne ocean measurements using AXBTs, current profilers and conductivity-temperature-depth (CTD) devices, moored CTDs and current profilers, and wind fields using the NOAA/Hurricane Research Division "H*Wind" product, which resolves a 10-m field based on a plethora of measured data sources [51]. In order to convert the winds into a surface stress, they applied equation (1) with the legacy C_{D_LP}, but maximized its value at 2.6 x 10^{-3} [51], slightly above the asymptote applied in C3.5 and by Donelan. Finally, they supplemented their primarily in-situ measurements with those from satellites via sea surface height anomaly (SHA), which through Ekman principles, illuminates the presence of WCEs and CCEs through positive and negative anomalies respectively. With all of these data in place, they correlated the storms' intensities and underlying oceanic mixed layer responses. Finally, as a bit of comparison case study, elements of HU Rita's passage will be detailed below.

On September 22, 2005, HU Rita transited over branches of the warm LC, where it reached its peak category five intensity, before weakening after passing over a CCE and an area of high wind shear and eventually making landfall over southern Louisiana two days later [51]. In addition to their series of ocean temperature and horizontal current observations, Jaimes and Shay [51] also aimed to parameterize the vertical velocity response as the storm interacted with geostrophic eddies. While the specific derivation is beyond the scope of this study (as it will not be explicitly used), their final formulation for the vertical velocity resulted in
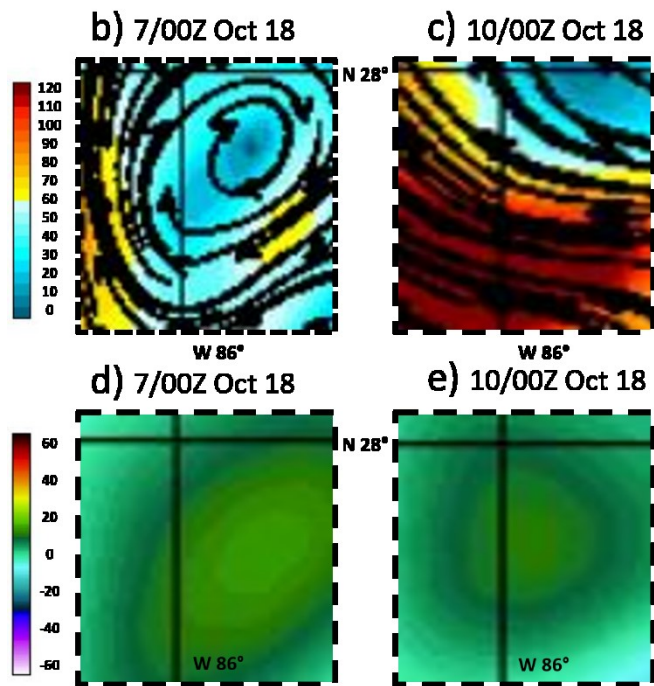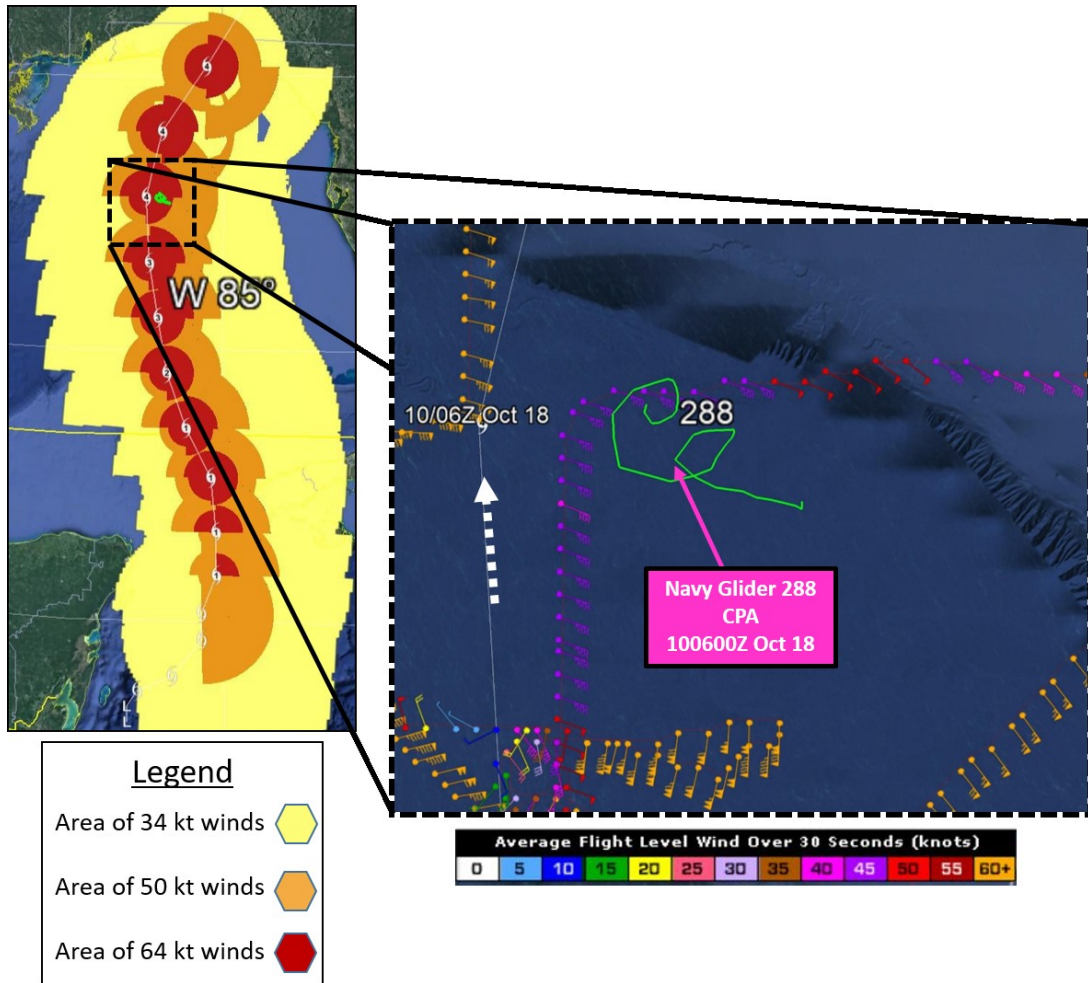
$$w_{JS} = \frac{1}{\rho_w f^2}\left(\frac{\partial \tau^y}{\partial x} - \frac{\partial \tau^x}{\partial y}\right) \cdot \nabla \zeta_g, \qquad (5.2a)$$

where ζ_g is the vertical component of the geostrophic relative vorticity [51]. This relationship, the majority of which contains Ekman principles via equation (5.1i), boils down to this physical,

qualitative result: there will be upwelling (downwelling) when the sign of the vertical curl of wind stress matches (opposes) that of an eddy's geostrophic relative vorticity. For example, when HU Rita passed directly over a WCE, where the signs of the vertical wind stress curl and geostrophic relative vorticity were positive and negative respectively, leading to downwelling ahead of the storm. This was observed on multiple occasions, including when it passed the bulge of the LC [51], which on a mesoscale, has an anti-cyclonic current pattern at its northern tip.

These results are profound in the context of this study as they also contradict traditional upper oceanic response theories regarding vertical velocity, while providing a physical explanation for downwelling that extends the previous reasoning using Ekman principles alone. In this study, however, downwelling was observed ahead of every storm's passage, which could be also be explained by the same theory, but in more general way where the flow orientation of pre-existing mixed layer currents opposes that of the wind stress. Nonetheless, the findings of Jaimes and Shay [51] are the only other published study (known by the author) to also claim the presence of downwelling as a possible and physically-reasonable response to TC passage, further cementing the validity of the results herein.

With that being said, it seemed prudent to conduct one final case study herein to corroborate their presented theories. Unfortunately, however, their quantitative inquiry into the vertical velocity was predicated on the presence of background eddies, generating the necessary geostrophic relative vorticity, which is not something that the current version of the PWP model is able to resolve (due to the initially homogeneous ocean). With that being said, a qualitative, visual analysis of HU Michael, which also passed over smaller eddies in the Gulf of Mexico as a category four storm, was completed using HYCOM near-surface current and SHA output [43] as well as flight-level winds measured by NOAA reconnaissance aircraft [12], as presented in Figure 5-3. In order to determine the "background" eddy field, Figures 5-3b and 5-3d display the near surface currents and corresponding SHA approximately three days prior to storm passage. The culmination of those two modeled outputs in the presence of a WCE, as evidenced by the anti-cyclonic flow and accompanying positive and concentric SHA. As the storm approaches, wind stress forcing dominates the near surface ocean currents, essentially removing the presence of the WCE in Figure 5-3c; however, a weaker, yet still existing WCE is evident in the SHA, as illustrated in Figure 5-3e. With the presence of a WCE established in the vicinity of Navy glider 288, near the time of the CPA with HU Michael, an evaluation of the wind stress curl and

Legend

Area of 34 kt winds

Area of 50 kt winds

Area of 64 kt winds

b) 7/00Z Oct 18

c) 10/00Z Oct 18

d) 7/00Z Oct 18

e) 10/00Z Oct 18

Figures 5-3a, 5-3b, 5-3c, 5-3d, 5-3e: a) Interaction between HU Michael and Navy glider 288 [11]. The left image displays the majority of the storm's track with the modeled area of over water wind speeds in 34, 50 and 64+ knot thresholds. The right image zooms in on this interaction and labels the time and position of the CPA between the storm and glider as well as plots 30 second average flight level wind vectors as measured by NOAA reconnaissance aircraft [12]; b, c) HYCOM model of near surface currents [cm/s] valid 76 and 6 hours before storm CPA, respectively [43]; and d, e) HYCOM model of SHA [cm] valid 76 and 6 hours before storm CPA, respectively [43]. The region outlined in b-e) is the same as that of the right graphic in a).

geostrophic relative vorticity can be completed akin to Jaimes and Shay [51]. While the aforementioned theory of WCEs and TCs would point to a negative vertical velocity from equation (5.2a), measured cyclonic wind vectors ahead of storm CPA (Figure 5-3a) coupled with underlying anti-cyclonic current motion, visually confirm this result. Furthermore, as previously presented in Figure 4-7, HU Michael caused a (ROHC-derived) measured downwelling velocity over 5 mm/s, which approaches that estimated by Jaimes and Shay [51] during HU Rita's interaction with a WCE.

   In the only apples-to-apples comparison possible (based on geographic location, storm strength and track and available data), the physical basis presented for downwelling ahead of HU Rita was virtually replicated in HU Michael. This small case study coupled with the presented downwelling analysis now carries much more strength with an extended physical, TC intensity index independent basis to help supplement this weighty finding.

5.2.2   Drag Coefficients – Zedler et al. (2009)

In much the same way as the last section presented the results of very similar study to that herein for vertical velocity, the following will do the same with respect to the drag coefficient at high wind speeds. In order to determine the most accurate C_D parameterization under such forcing, Zedler et al. compared model simulations to upper oceanic measurements, with the primary difference between each run being its drag coefficient [52]. In particular, she and her coauthors aimed to simulate the passage of HU Frances over a series of drifters outfitted with thermistors and profiling floats, deployed via WC-130J aircraft, as part of the Coupled Boundary Layers/Air-Sea Transfer (CBLAST) campaign [52]. These devices had variable CPAs between 0-200 km from the storm's track, but all on the right side [52]. For comparison, Zedler et al. [52] utilized the MIT Ocean General Circulation Model (OGCM), which contained mostly an analogous set-up and series of assumptions as the PWP model, but alternatively did apply the first order closure K-Profile Parametrization (KPP) for shear instability induced vertical mixing. Additionally, rather than building the storm as a function of its key parameters and assuming a Rankine vortex-like structure, as described in Section 4.1.2.3, they utilized the NOAA H*Wind product to simulate HU Frances' wind stress field [52]. With the model in place, they ran each simulation using four different drag coefficients including that of Donelan, Powell, constant (1.2 x 10^{-3},

which is 0.1 x 10^{-3} smaller than $C_{D\_Const\ C_D}$ used herein) and another as developed during the CBLAST experiment [52]. In the end, for both mixed layer temperature and 15 m horizontal currents, the most accurate forcing as compared to measured data was that of the constant drag coefficient, with Donelan performing the worst [52]. As a result, Zedler et al. [52] concluded that the drag coefficient likely asymptotes or even decreases under extreme wind speed and with Donelan's C_D as the strongest, yet least precise, their investigation clearly established none of the legacy parameterizations, including Large and Pond [37] (as they referenced) or Garratt [21] or Wu [20] as used herein, were accurate in such forcing.

The similarities between this study and the work of Zedler et al. [52] are uncanny (especially given the fact that the author did not become aware of their publication until well after the conclusion of data analysis). In fact, both overarching conclusions with respect to the drag coefficient were the same—a linearly increasing C_D is invalid under TC forcing. With that said however, while they found the constant C_D to be the most accurate, it was that of Powell (with spray, then wind only) and actually Donelan (wind only) that were the most precise parameterizations herein, although not to statistical significance. Furthermore, in this study, $C_{D\_Const\ C_D}$ did not outperform that of Donelan overall or in most cases. On a separate front, Zedler et al. [52] concluded that a decreasing C_D may be most representative of the ocean surface under extreme wind forcing. However, this was simply based on the weakest of their applied drag coefficients performing the best rather than via testing a C_D that actually decreased with U_{10}, such as $C_{D\_Zij\_bounded}$ and C_{D_Hwg} used herein. Due to the differences between each studies' results, it is hard to say how they would have performed if applied to the MIT/OGCM and HU Frances, but herein, the drag coefficients of Zijlema (with spray and wind only) and Hwang (wind only) did outperform $C_{D\_Const\ C_D}$. Overall, despite the detailed differences, the main findings were in agreement and together help to bolster the strength of each result through the consistency in outcomes using like methodology.

5.3   Final Claim and why Downwelling Matters?

Based on the culmination of the downwelling analysis of DWI using TC intensity indices, PWP modeled vertical velocities and Ekman dynamics and a qualitative case study involving HU Michael akin to that by Jaimes and Shay [51], downwelling was consistently modeled and

measured ahead of all storms and locations. As physically reasoned via Ekman dynamics and furthered when considering the orientations of the vertical wind stress curl as compared to that of the upper oceanic currents/eddies' geostrophic relative vorticity, downwelling should be present (with varying magnitudes) ahead of every storm. With that said, why does it matter?

First, with downwelling ahead of storm passage, there is a depression in the depth of the 26°C isotherm and notionally a proportional pre-storm increase in TCHP, both of which are positive indices for storm intensification. As such, it is completely conceivable that the downwelling, especially when enhanced through the anti-correlation of the vertical wind stress curl and upper oceanic currents/eddies' geostrophic relative vorticity, increases the strength of the storm. There obviously can be holes poked through such an argument as there are many unknowns, but further research involving case studies and/or high time and spatial resolution, coupled atmosphere-ocean models would be needed to explore this in detail. As it stands, the theory that pre-CPA downwelling at least slightly enhancing TC intensity is at least arguable from an index standpoint, aligning with larger-scale ideas of several other publications [4], [6], [7].

Second, there could be implications with respect to storm surge. As a bit of background, storm surge is an abnormal rise in water due to extreme meteorological conditions, which exceeds that of the astronomical tide [53]. In general, storm surge is affected by the following series of characteristics including: atmospheric pressure—lower pressure leads to a higher water level; maximum wind speed—stronger winds lead to more significant storm surge; translation speed—for an open coastline (as is the case for most TC landfalls), faster moving storms generate a higher water level; storm radius—due the duration and sheer area of strong winds, a higher volume of water can be forced ashore; angle of approach—a storm moving perpendicular to the coast will produce a more significant surge than one moving at a shallower angle; width and bottom gradient of the continental shelf and slope—the wider and more shallow the shelf/slope, the greater the storm surge [53]; and several others. Historically, however, the first two, which combine to as the storm's strength, have been taken to be the indices most commonly applied to storm surge and emergency planning via the Saffir-Simpson scale [54]. Unfortunately, a simple case study comparing HUs Camille and Katrina, which made landfall in the same region as category five and three storms respectively, illustrates this devastating misconception [54]. As one of the strongest storms to ever make landfall in the U.S., HU Camille only directly lead to the deaths of about 250 people [55]; however, 36 years later, HU

Katrina claimed over 1800 lives as a much weaker, but larger storm [18]. Based on this example, it is clear that storm surge forecasting remains a challenge even in modern times, akin to that of TC intensity prediction, and the ramifications of each are on the order of billions of dollars and thousands of lives.

Diving into storm surge dynamics from a more physical oceanographic perspective, there are two phenomena and stages specifically leading to the water advancing towards the coast. First, when the storm is approaching the coast at a perpendicular angle, the leading edge of winds will blow parallel to the coast, which due to the surface stress, generates a coastal current with building, young wind waves [56]. While these waves would not initially be oriented towards the beach, as the storm makes landfall, the wind direction (on the right-side of a NH TC) will shift and the current will directly approach the coast. Prior making landfall, as a result of the coastally-parallel winds, Ekman transport forces water towards the coast throughout the column [56]. Second, even when the storm's eye has moved inland and the wind direction allows for any remain Ekman transport to be seaward, older, swell waves will persist and continue drive near-surface water ashore. Through these processes, the surface causing coastal flows can only be balanced via bottom stress (in a steady state) [56], which is why more gently sloped shelves are conducive to a greater surge—less friction [53]. In reality, however, storm surge is a transient problem [56] and synoptic scale motion governs the duration of the event, to first order, as a steady state is rarely reached.

Within the aforementioned oceanic explanation of storm surge, the TC's vertical motion was never mentioned or considered. Based on traditional theories, that should not be surprising as the predominant and initial vertical velocity response of the ocean is upwelling [14], which through Ekman processes, is accompanied by a depression in the SSA. Contrarily, in a downwelling regime, like is well-known in a WCE for example, the anti-cyclonic horizontal currents lead to inward Ekman transport and a rise in the SSA. The same would be expected in the case of downwelling ahead of a TC, which would only worsen a storm surge. To help quantify this, a well-defined WCE can routinely boast a SSA of tens of cm [43], which could absolutely be the difference between the maintenance or breach of a water levee. From a different and more qualitative perspective, if there is persistent downwelling ahead of a passing storm, as it approaches the coast, the shallowing depths limit its ability to move vertically. As a result, in order to maintain continuity, the water must "go somewhere," which would be to

diverge horizontally, with a large portion being forced towards the shore. From either angle, this simple argument leads to the presence of downwelling as a potentially significant variable in storm surge enhancement. As such, while more research is obviously needed to specifically parameterize and test this assertion, there may be yet another important characteristic of TCs to consider in storm surge modeling and ultimately recommending appropriate safety responses to the general public.

THIS PAGE INTENTIONALLY LEFT BLANK

Chapter 6

Conclusion

6.1   Research Summary

Several infamous storms and recent studies together have indicated TC intensity forecasting has only been advancing slowly [2], but when incorporating greater dimensions and volumes of oceanic temperature measures, the results have been promising [4], [5], [6], [7], [8], [9]. One way of safely and efficiently measuring upper ocean temperature profiles during the passage of such storms is via ALAMO floats deployed from USAF reconnaissance flights. In a stroke of good fortune, ALAMO 9077, which was alluded by its intended storm (HU Guillermo), meandered due north for nearly a month before being intercepted by HU Ignacio [11], [12]. The resulting temperature measurements from this virtual "direct hit" motivated this entire study—a marked upper oceanic isotherm depression ahead of the storm's CPA with the float. This apparent downwelling was initially puzzling due to traditional theories regarding the upper oceanic response to TC passage, which universally described the initial vertical motion as that of upwelling as a result of positive wind stress curl [14]. To determine what might cause and accurately model such a response, other traditional ideas with respect to wind stress were challenged. First, while many legacy drag coefficients linearly increase with wind speed, several modern formulations maximize upon reaching storm force winds, where their end behavior then consists of an asymptotic and/or decreasing dependence on U_{10} [18]. Many of the modern ideas were buoyed based on a hypothesis in which the development of sea foam and spray covering the surface might significantly alter air-sea momentum exchange at wind speeds greater than 40 m/s [24], thus saturating or even diminishing the drag coefficient. Second, most models utilize a bulk surface flux parameterization of turbulent exchanges across the air-sea interface, thus smaller scaler phenomenon like sea spray and its associated stress are either omitted or crudely formulated [15]. In the absence of the enthalpy and momentum fluxes generated by sea spray, however, model simulations indicated TCs would be unable to reach the extreme, yet oft

113

measured, devastating strengths of category five storms [33]. In addition, the latter flux has the potential to transfer a significant amount of momentum, from the extreme winds of the atmosphere to the slower moving ocean, upon the drops' reentry. As a result, explicitly adding a parameterization of this flux to the traditional interfacial, wind only stress [33] may elicit the measured downwelling response and more accuracy overall. Taken together, the drag coefficient and sea spray could potentially have a major effect on how the upper ocean responds to extreme stress forcing, such as via a passing TC. In total, this study aimed to replicate the measured downwelling by ALAMO 9077 below HU Ignacio, but also in three other storms (HUs Irma, Florence, and Michael) using measurements by other floats and a Navy glider, through comparing these measured data to PWP modeled output of a combination of forcing parameterizations encompassing legacy and modern drag coefficients, with and without sea spray stress. Additionally, irrespective of the downwelling results, an attempt was made to discern the effect of modifying the stress forcing through the drag coefficient and sea spray, ultimately aiming to illuminate general upper oceanic response trends and accuracy statistics throughout the passage of each storm.

A total of 56 model runs were completed through the PWP model, a half order closure scheme that formulates turbulent vertical mixing via the bulk method, using 14 forcing parameterizations across the aforementioned four storms. Using this output along with measured data, four variables were plotted in a time series as a function of each HU's passage, including the depth of the 26°C isotherm, TCHP, ROHC and vertical velocity, with the first two serving as TC intensity indices. Next, both qualitative and quantitative comparisons of the modeled output and measured data were completed, beginning with the DWI test to evaluate the presence of downwelling. Overall, 80.7% of tested variables (after removing TCHP due to its limitations as a vertical velocity index) across all six storms/locations qualitatively exhibited the presence of downwelling ahead of the traditional post-CPA upwelling. The subsequent comparison involved visually identifying trends across these four variables as a function of time after storm CPA, where four overarching themes were illuminated including each measured variable being generally well-modeled and replicated; the magnitude of the modeled response was directly proportional to the strength of the forcing (i.e. legacy drag coefficients with sea spray stress induced the greatest variable response); no one forcing parameterization was clearly more accurate than any other; and finally, however, Garratt's legacy C_D was often, yet not universally

in time, much too strong relative to measurements. Based on the last two developments, a quantitative, statistical analysis testing for accuracy was prudent, which involved cumulative normalized measured vs. modeled PbP deltas across the total measured duration as well as partitioned into subintervals, aiming to identify any forcing parameterizations better characterizing the forced and/or relaxation stages of TC passage [39]. This series of analyses indicated the following key findings where both forcing parameterizations involving Garratt's C_D were statistically significantly proven to be outliers in every time interval; the formulations utilizing Powell's C_D were the most accurate, but not to a statistical significance; sea spray stress increased the magnitude of each variable an average of 10.3%, matching a similar published hypothesis [19], but was statistically significantly less accurate compared to wind only stress metrics; and modeled vs. measured deltas increased as a function of translation speed, possibly due to wave age, and were maximized at the location of peak forcing. Lastly, while the final two interpretations were made based upon limited data, their physical foundation strengthens all of the previously presented statistical analyses.

Stepping back to synthesize in the context of the original motivation, the downwelling measured by ALAMO 9077 beneath HU Ignacio was model-replicated, both in that HU and each of the others. This downwelling can be physically explained via Ekman principles of alternating signs of the wind stress curl as a function of the CPA with the radius of max winds (e.g. negative ahead, positive inside and negative behind). With that said, when coupling this with the sign of the geostrophic relative vorticity found in upper oceanic currents and eddies, when these do not match, downwelling can also be induced [51], as shown in HU Michael's interaction with a WCE. Next, legacy drag coefficients that monotonically increase with wind speed are outliers herein and do not seem physically possible, as argued by many publications over the past 16 years, including at least one using an extremely similar methodology [52]. With that said, however, the specific end behavior of C_D under TC force winds remains unclear from this and many of those same studies [18], [52]. Additionally, while explicitly adding sea spray to the interfacial stress does not improve model accuracy, its effect cannot be neglected, rather must be expertly considered upon selecting a drag coefficient when applying the usual bulk parameterization. This may seem counter-intuitive, but under extreme wind forcing, winds clip the largest wave crests, expelling spray droplets that reduce the amplitude of smaller waves upon reentry. Taken together, wind and spray limit the wave field and as such, do the same to the drag

coefficient, ultimately demanding that its parameterization incorporate sea spray theory and/or at least have a decreasing or asymptotic end behavior of $C_D(U_{10})$.

6.2   Recommendations for Future Research

Initially, the primary aim of this study was to determine if the apparent downwelling as measured by ALAMO 9077 below HU Ignacio was really possible; could it be replicated by an ocean model? After its successful replication, more storms and measurements were considered, to then deduce possible commonalities during all TC passages. Again after replication, the study continued to grow to determining the accuracy of many forcing parameterizations, taking a deep dive into legacy and modern drag coefficients and the effect of sea spray stress. Subsequently, there were a few more layers of analysis conducted, but this study really confirmed a few fundamental ideas including the first upper oceanic response to a passing TC is pre-CPA downwelling, legacy drag coefficients are outliers and should not be used in TC modeling and sea spray theory is important to the C_D selection for proper bulk parameterization. At the risk of repetition, the above results have largely established the groundwork for many potential, detailed investigations where proving each of those arguments is no longer paramount. The following paragraphs will provide a few of the many associated ideas requiring research.

First, since downwelling depresses the depth of the 26°C isotherm and increases TCHP, two indices pointing to storm intensification, applying a coupled atmosphere-ocean model to assess this connection could be fruitful. In doing so, the ability to assess the effect of downwelling-induced intensification against other factors above and below the water such as wind shear, relative humidity, upper level convergence/divergence, land friction, eddies, currents, etc., could illuminate or eliminate its criticality in TC intensity modeling.

Second, a similar study to the methodology applied herein could be conducted after a storm has interacted with a significant current or eddy. In this study, however, by incorporating a background current/eddy field vs. a homogeneous ocean, an analysis of the resulting vertical motion could quantitatively codify the presented physical reasoning for downwelling involving geostrophic relative vorticity.

Third, as presented in Section 4.3.2.3, there were measured and modeled high frequency, sub-inertial oscillations in the vertical velocity time series that are seemingly unaccounted for with

respect to traditional oceanic response theories to TC passage. Developing a device or method to measure and categorize these in a single storm could help to advance principles within the relaxation stage.

Fourth, based on limited data, this study concluded there may be a correlation between two TC development/intensification indices as a function of storm translation speed and location of maximum wind forcing. If these trends could be confirmed within a larger-scale study, they could be helpful in understanding and interpreting TC intensity model output.

Fifth, throughout this entire study, the great isotherm depression measured by ALAMO 9077 was replicated in terms of shape, timing and frequency, but never in magnitude. Even the strongest forcing parameterization applied herein, Garratt's C_D with spray stress, which is now known to be an over-estimating outlier, was 10 m short of the 40 m perturbation in the depth of the 26°C isotherm, near CPA with HU Ignacio. If the strongest drag coefficient with the added spray stress couldn't get there, what could it be? Unfortunately, the question remains, but it could be found by attempting to correlate internal ocean tides with the initial downwelling and upwelling associated with strong TCs. If it is assumed the most accurate forcing parameterization herein is ground truth, such a study could consider whether or not it would be feasible for an internal tide, which are prominent along the Hawaiian Ridge and much of the Pacific Ocean [57], to add another 20 m to the initial perturbation. If so and if downwelling is correlated to TC intensification or the following topic, the implications of internal tides could be paramount.

For the sixth and final potential research application, the "so what" is presented—why does downwelling really matter? If it is assumed the impact to TC intensification would be relatively small, which is likely, then the implications of downwelling potentially enhancing storm surge is why it matters. Theoretically, downwelling would be accompanied with a positive SHA and qualitatively, if the water wants to move down, but is suddenly limited by depth, it must be forced horizontally; from either perspective, its stands to reason that there could be a strong connection between TC downwelling and storm surge enhancement. With that said, case studies and high resolution ocean and surge models could prove or dispel this idea, ultimately potentially having obvious applications in storm surge forecasting and emergency management.

6.3   Future Applications

As alluded to above, this study aimed to tackle one very specific question and while it respectfully expounded from there, its direct future applications are not robust, but simple. First, the ocean responds by downwelling ahead of TCs, which can be physically reasoned with Ekman dynamics (and extensions). Second, when conducting TC research, refrain from using any drag coefficient that is linearly dependent with wind speed; however, there is almost no wrong answer as long as its limit in high winds does not greatly exceed 2.5 x 10^{-3}. Third, sea spray is very important to understanding what happens to the ocean's surface under TC forcing, but bulk parameterizations are sufficient as a long as the drag coefficient does consider it in its development. Naturally, the second and third findings are interconnected and fundamental to quantitatively and physically characterizing the sea surface in extreme winds. As a final comment, while adjusting the C_D will absolutely change the total stress and oceanic response, to a first order, choosing any of the modern drag coefficients presented herein, another with a similar shape or even constant, will likely be sufficient.

Bibliography

1. Emanuel, K., 2005: Increasing destructiveness of tropical cyclones over the past 30 years. *Nature*, **436**, 686–688, doi:10.1038/nature03906.

2. DeMaria, M., Sampson, C. R., Knaff, J. A., and Musgrave, K. D., 2014: Is tropical cyclone intensity guidance improving? *Bull. Amer. Meteor. Soc.*, **95(3)**, 387-398, https://doi.org/10.1175/BAMS-D-12-00240.1.

3. Tropical Atlantic – Model archive for major Hurricane Katrina (12L) – 2005. Hollis Innovation, accessed 14 May 2019, http://tropicalatlantic.com/models/models.cgi?basin=al&year=2005&storm=12&display=archive.

4. Sanabia, E., Barrett, B. S., Black, P. G., Chen, S., and Cummings, J. A., 2013: Real-time upper-ocean temperature observations from aircraft during operational hurricane reconnaissance missions: AXBT demonstration project year one results. *Wea. Forecasting,* **28**, 1404-1422, https://doi.org/10.1175/WAF-D-12-00107.1.

5. Jayne, S. R. and Bogue, N. M., 2017: Air-deployable profiling floats. Oceanography, **30(2)**, 29-31.

6. Leipper, D. F. and Volgenau, D., 1972: Hurricane heat potential of the Gulf of Mexico. *J. Phys. Oceanogr.*, **2**, 218-224, https://doi.org/10.1175/1520-0485(1972)002<0218:HHPOTG>2.0.CO;2.

7. Price, J., 2009: Metrics of hurricane-ocean interaction: vertically-integrated or vertically-averaged ocean temperature. *Ocean Sci.*, **5**, 351-368, https://doi.org/10.5194/os-5-351-2009.

8. Ito, K., Kuroda, T., and Saito, K., 2015: Forecasting a large number of tropical cyclone intensities around Japan using a high-resolution atmosphere–ocean coupled model. *Wea. Forecasting,* **30**, 793-808, https://journals.ametsoc.org/doi/pdf/10.1175/WAF-D-14-00034.1.

9. Mogensen, K. S., Magnusson, L., and Bidlot, J. R., 2017: Tropical cyclone sensitivity to ocean coupling in the ECMWF coupled model. *J. Geophys. Res.: Oceans*, **10**, 4392-4412, https://doi.org/10.1002/2017JC012753.

10. Gallaudet, T., 2016: U.S. Navy ocean gliders: unmanned underwater vehicles that are improving our understand of the world's oceans. Accessed 3 March 2019, https://navylive.dodlive.mil/2016/12/19/u-s-navy-ocean-gliders-unmanned-underwater-vehicles-that-are-improving-our-understanding-of-the-worlds-oceans/.

11. WHOI ALAMO/ALTO float summary. Woods Hole Oceanographic Institution, accessed 23 April 2019, http://argo.whoi.edu/alamo/.

12. Tropical Atlantic – Tropical cyclone model and best track archive. Hollis Innovation, accessed 23 April 2019, http://tropicalatlantic.com/models/models.cgi?archive=1.

13. Air launched autonomous micro observer (ALAMO). Woods Hole Oceanographic Institution, accessed 24 April 2019, https://alamo.whoi.edu/.

14. Geisler, J. E., 1970: Linear theory of the response of a two layer ocean to a moving hurricane. *Geophys. Astrophys. Fluid Dyn.*, **1**, 249-272, https://doi.org/10.1080/03091927009365774.

15. Andreas, E. L., 2011: Fallacies of the enthalpy transfer coefficient over the ocean in high winds. *J. Atmos. Sci.*, **68**, 1435-1445, https://doi.org/10.1175/2011JAS3714.1.

16. Chen, S., Price, J. F., Zhao, W., Donelan, M. A., and Walsh, E. J., 2007: The CBLAST-Hurricane program and the next-generation fully coupled atmosphere-wave-ocean models for hurricane research and prediction. *Bull. Am. Meteorol. Soc.*, **88(3)**, 311-318, https://journals.ametsoc.org/doi/pdf/10.1175/BAMS-88-3-311.

17. Emanuel, K., 1995: Sensitivity of tropical cyclones to surface exchange coefficients and a revised steady-sate model incorporating eye dynamics. *J. Atmos. Sci.*, **52**, 3969-3976, https://journals.ametsoc.org/doi/abs/10.1175/1520-0469(1995)052%3C3969:SOTCTS%3E2.0.CO;2.

18. Bryant, K. M. and Akbar, M., 2016: An exploration of wind stress calculation techniques in hurricane storm surge modeling. *J. Mar. Sci.*, **4**, 1-26, https://doi.org/10.3390/jmse4030058.

19. Andreas, E. L., 2004: Spray stress revisited. *J. Phys. Oceanogr.*, **34**, 1429-1440, https://doi.org/10.1175/1520-0485(2004)034<1429:SSR>2.0.CO;2.

20. Wu, J., 1982: Wind-Stress coefficients over sea surface from breeze to hurricane. *J. Geophys. Res.*, **12**, 9704-9706, https://doi.org/10.1029/JC087iC12p09704.

21. Garratt, R., 1977: Review of drag coefficients over oceans and continents. *Mon. Weather Rev.*, **105**, 915-929, https://doi.org/10.1175/1520-0493(1977)105<0915:RODCOO> 2.0.CO;2.

22. Price, J. F., 1981: Upper ocean response to a hurricane. *J. Phys. Oceanography*, **11**, 153-175, https://doi.org/10.1175/1520-0485(1981)011<0153:UORTAH>2.0.CO;2.

23. Charnock, H., 1955: Wind stress on a water surface. *Q. J. R. Meteorol. Soc.*, **81**, 639-640, https://doi.org/10.1002/qj.49708135027.

24. Powell, M. A., Vickery, P. J., Reinhold, T. A., 2003: Reduced drag coefficient for high wind speeds in tropical cyclones. *Nature*, **422**, 279-283, https://www.nature.com/articles/nature01481.

25. Donelan, M. A., Haus, B. K., Reul, N, Plant, W. J., Stiassnie, M., Graber, H. C., Brown, O. B., and Saltzman, E. S., 2004: On the limiting aerodynamic roughness of the ocean in very strong winds. *Geophys. Res. Lett.*, **31**, 1-5, https://doi.org/10.1029/2004GL019460.

26. Zijlema, M., Van Vledder, G. P., and Holthuijsen, L. H., 2012: Botto Friction and Wind Drag for Wave Models. *Coastal Engineering*, **65**, https://doi.org/10.1016/j.coastaleng.2012.03.002.

27. Hwang, P. A., 2018: High-wind drag coefficient and whitecap coverage derived from microwave radiometer observations in tropical cyclones. *J. Phys. Oceanogr.*, **48**, 2221-2232, https://doi.org/10.1175/JPO-D-18-0107.1.

28. Edson, J. B. and Coauthors, 2013: On the exchange of momentum over the open ocean. *J. Phys. Oceanogr.*, **43**, 1589-1610, https://doi.org/10.1175/JPO-D-12-0173.1.

29. Callaghan, A., de Leeum, G., Cohen, L., and O'Dowd, C. D., 2008: Relationship of oceanic whitecap coverage to wind speed and wind history. *Geophys. Res. Lett.*, **35**, 1-5, https://doi.org/10.1029/2008GL036165.

30. Gall, J. S., Frank, W. M., and Kwon, Y., 2008: Effects of sea spray on tropical cyclones simulated under idealized conditions. *Mon. Weather Rev.*, **136**, https://doi.org/10.1175/2007MWR2183.1.

31. Andreas, E. L., 1992: Sea spray and the turbulent air-sea heat fluxes. *J. Geophys. Res.*, **97**, https://doi.org/10.1029/92JC00876.

32. Andreas, E. L., 1998: A new sea spray generation function for wind speeds up to 32 m s^-1. *J. Phys. Oceanogr.*, **28**, 2175-2184, https://doi.org/10.1175/1520-0485(1998)028 <2175:ANSSGF>2.0.CO;2.

33. Andreas, E. L. and Emanuel, K. A., 2001: Effects of Sea Spray on Tropical Cyclone Intensity. *J. Atmos. Sci.*, **58**, 3741-3751, https://doi.org/10.1175/1520-0469(2001) 058<3741:EOSSOT>2.0.CO;2.

34. Wu, J., Murray, J., and Lai, R. J., 1984: Production and distributions of sea spray. *J. Geophys. Res.*, **89**, 8163-8169, https://doi.org/10.1029/JC089iC05p08163.

35. Monahan, E. C., Spiel, D. E., and Davidson, K. L., 1986, *A Model of Marine Aerosol Generation via Whitecaps and Wave Disruption*, D. Reidel Publishing Company, 294 pp.

36. Smith, M. H., Park, P. M., and Consterdine, I. E., 1993: Marine aerosol concentrations and estimated fluxes over the sea. *Q. J. R. Meteorol. Soc.*, **119**, 808-824, https://doi.org/10.1002/qj.49711951211.

37. Large, W. G. and Pond, S., 1981: Open ocean momentum flux measurements in moderate to strong winds. *J. Phys. Oceanogr.*, **11**, 324-336, https://doi.org/10.1175/1520-0485(1981)011<0324:OOMFMI>2.0.CO;2.

38. Argo – How Argo floats work. Accessed 10 June 2019, http://www.argo.ucsd.edu/How_Argo_floats.html.

39. Price, J. F., Sanford, T. B., and G. Z. Forristall, 1994: Forced stage response to a moving hurricane. *J. Phys. Oceanogr.*, **24**, 233-260, https://doi.org/10.1175/1520-0485(1994)024<0233:FSRTAM>2.0.CO;2.

40. Ireton, G., Jarrett, M., and Vincent, N., 2016: Office of the Federal Coordinator for Meteorological Services and Supporting Research. Accessed 4 March 2019, https://www.ofcm.gov/groups/COPC/meetings/2016-01/02-NAVO%20Overview%20Brief%20to%20COPC%203-4%20May%2016%20v2.pdf.

41. Tropical Atlantic – Wind speed diagram for National Hurricane Center models for Hurricane Michael – 2018. Hollis Innovation, accessed 13 June 2019, http://tropicalatlantic.com/models/models.cgi?basin=al&year=2018&storm=14&display=wind_diagram&run=2018100812.

42. Price, J. F., Weller, R. A., and Pinkel, R., 1986: Diurnal cycling: Observations and models of the upper ocean response to diurnal heating, cooling, and wind mixing. *J. Geophys. Res.,* **7**, 8411-8427, https://doi.org/10.1029/JC091iC07p08411

43. Naval Research Laboratory – Real-time 1/12° global HYCOM+CICE nowcast/forecast system. Accessed 16 June 2019, https://www7320.nrlssc.navy.mil/GLBhycomcice1-12/.

44. Kundu, P. K. and Cohen, I. M., 2008, *Fluid Mechanics*, Elsevier Incorporated, 872 pp.

45. Dima, I. and Desflots, M., 2010: Wind profiles in parametric hurricane models. *Air Currents*, **7**, 1-6.

46. Courant, R., Friedrichs, K., and Lewy, H., 1928: On the partial difference equations of mathematical physics. *Mathematische Annalen*, **100**, 32-74.

47. Fofonoff, N. P and Millard Jr., R. C., 1983: Algorithms for computation of fundamental properties of seawater. *Unesco Technical Papers in Marine Science*, **53**, 26, http://hdl.handle.net/11329/109.

48. Harwood, P. and Scarrott, R., 2013, Product data handbook: Tropical cyclone heat potential (TCHP) Data. Issue No. 2, 21 pp, http://www.storm-surge.info/sites/storm-surge.info/files/eSurge_D180J_HB_HP1_TCHPDataHandbook_2.0.pdf.

49. Vallis, G. K., 2017: *Atmospheric and Oceanic Fluid Dynamics: Fundamentals and Large-Scale Circulation*, Cambridge University Press, 946 pp.

50. Monger, B. and Pershing, A., 2005: Cornell University Department of Earth & Atmospheric Sciences – EAS 494 – Physical Oceanography. Accessed 8 July 2019, http://www.geo.cornell.edu/ocean/p_ocean/.

51. Jaimes, B. and Shay, L., 2009: Mixed layer cooling in mesoscale oceanic eddies during Hurricanes Katrina and Rita. *Mon. Weather Rev.*, **137**, 4188-4207, https://doi.org/10.1175/2009MWR2849.1.

52. Zedler, S. E., Niiler, P. P., Stammer, D., Terrill, E., and Morzel, J., 2009: Ocean's response to Hurricane Frances and its implications for drag coefficient parameterization at high wind speeds. *J. Geophys. Res.*, **114**, 1-19, https://doi.org/10.1029/2008JC005205.

53. National Hurricane Center – Storm Surge Unit, Introduction to Storm Surge. Accessed 12 July 2019, https://www.nhc.noaa.gov/surge/surge_intro.pdf.

54. Irish, J., Resio, D., and Ratcliff, J., 2008: The influence of storm size on hurricane surge. *J. Phys. Oceanogr.*, **38**, 2003-2013, https://doi.org/10.1175/2008JPO3727.1.

55. NOAA – National Hurricane Center and Central Pacific Hurricane Center, Hurricanes in History. U.S. Dept of Commerce - NOAA, accessed 13 July 2019, https://www.nhc.noaa.gov/outreach/history/#camille.

56. Gill, A. E., 1982: *Atmospheric Ocean Dynamics*, Academic Press, 662 pp.

57. Niwa, Y. and Hibiya, T., 2001: Numerical study of the spatial distribution of the M2 internal tide in the Pacific Ocean. *J. Geophys. Res.,* **106**, 22441-22449, https://doi.org/10.1029/2000JC000770.